Title
An atomistic understanding of exciton-phonon coupling and nonradiative processes in semiconductor nanocrystals

Author
Jasrasaria, Dipti

Publication Date
2022

Peer reviewed|Thesis/dissertation

An atomistic understanding of exciton-phonon coupling and nonradiative processes in semiconductor nanocrystals

by

Dipti Jasrasaria

A dissertation submitted in partial satisfaction of the

requirements for the degree of

Doctor of Philosophy

in

Chemistry

in the

Graduate Division

of the

University of California, Berkeley

Committee in charge:

Professor Eran Rabani, Chair
Professor David Limmer
Professor Jeffrey Neaton

Summer 2022

An atomistic understanding of exciton-phonon coupling and nonradiative processes in semiconductor nanocrystals

Abstract

An atomistic understanding of exciton-phonon coupling and nonradiative processes in semiconductor nanocrystals

by

Dipti Jasrasaria

Doctor of Philosophy in Chemistry

University of California, Berkeley

Professor Eran Rabani, Chair

Semiconductor nanocrsytals (NCs) have been of much interest over the past several decades due to their highly tunable optoelectronic properties, which make them promising materials for applications ranging from solar energy conversion to quantum information. These optoelectronic properties depend significantly on electron-hole and exciton-phonon interactions, which are enhanced in NCs due to quantum confinement. A fundamental understanding of these interactions as well as processes, such as exciton decay and dephasing, is key to developing rational design principles for NCs with decreased thermal losses and increased quantum yields. Yet the description of excited carriers in NCs remains a great challenge for modern computational science. In this dissertation, we address this gap by developing a unified, atomistic model to accurately describe excitonic properties and dynamics in experimentally relevant NC systems with thousands of atoms and tens of thousands of electrons.

We develop an approach for calculating exciton-phonon couplings (EXPCs) and validate them by computing the reorganization energy, which is a measure of EXPC and is relevant for optical Stokes shifts, charge transfer processes, and NC-based device efficiencies. This microscopic theory allows us to delineate the dependence of the reorganization energy on NC size and structure as well as on phonon frequency and localization, resolving questions regarding the role of quantum confinement on EXPC. Additionally, we use this EXPC framework to perform quantum dynamics simulations of hot exciton cooling to address the longstanding controversy of the phonon bottleneck, which hypothesized slow nonradiative relaxation of hot carriers to the band edge in confined semiconductor nanostructures. Contrary to the phonon bottleneck but in agreement with recent experimental measurements, we find that cooling in CdSe NCs occurs in tens of femtoseconds. We show that this ultrafast timescale is governed by both electron-hole correlations and efficient multiphonon emission processes. Finally, we employ these tools in collaboration with experimentalists to understand lattice heating and polaron formation, photoluminescence, and charge trapping and

transfer in various NC systems. The atomistic theories and calculations presented in this dissertation bridge our understanding of molecular and bulk systems to provide fundamental insight into exciton-phonon interactions and nonradiative processes at the nanoscale.

To my mom and dad,

for teaching us to dream.

"For myself, I like a universe that includes much that is unknown and,
at the same time, much that is knowable.
A universe in which everything is known would be static and dull,
as boring as the heaven of some weak-minded theologians.
A universe that is unknowable is no fit place for a thinking being.
The ideal universe for us is one very much like the universe we inhabit.
And I would guess that this is not really much of a coincidence."

– Carl Sagan, *Can We Know the Universe?: Reflections on a Grain of Salt*

Contents

Acknowledgments

The past five years have been some of the most challenging yet joyful years of my life, and they wouldn't have been possible (or nearly as fun) without the love, support, and encouragement of a number of people.

First and foremost, I would like to thank my advisor, Eran Rabani. Thank you for your continuous commitment and patience, deep technical insight and intuition, fun scientific tidbits, and willingness to treat us as colleagues, not students. I have learned more physical chemistry and grown more as a scientist than I knew was possible. Through your example, I have also learned how to ask physically relevant and interesting questions, tell a scientific story, and foster an environment in which everyone feels valued. I am deeply grateful to have worked together these past five years, and I look forward to continued friendship and scientific conversations in the years to come.

The Rabani group has been the most collaborative, generous, and thoughtful set of colleagues to learn from and laugh with. Thank you to Lyran Kidon, my first mentor in the group, for your never-ending knowledge about open quantum systems as well as for your patience and faith in me as I learned how to be a grad student. Thank you to John Philbin for always being willing to answer my questions about nanocrystals or pseudopotentials, for discussing new ideas or debriefing research talks, and for being a great friend and scientific role model. Thank you to Tyler Takeshita and Amikam Levy for your deep technical knowledge and calming sense of perspective. Thank you, especially, to Paul Wrona for answering my random math questions, for morning catch-ups and lunch at noon, and for instilling laughter and silliness into every work day. I cannot imagine having gone through grad school without you. Thank you to Daniel Weinberg, Tommy Lin, Bokang Hou, Lior Verbitsky, and Kaiyue Peng for letting me play a part in your journeys as scientists. I have learned so much through our work together and am continually inspired by your energy; I know you have bright futures ahead of you. Thank you to Leslie Diettrick for keeping the heat running (quite literally) and for always being an energetic presence. I am also glad for the other members of the Rabani group that I've gotten to interact with over the years: Leopoldo Mejia, Wenjie Dou, Ming Chen, Nathan Ng, Alex Lee, Joseph Kelly, Michael Lostica, Srinath Ranya, Weifeng Hu, and Stephen Gee.

Outside of the Rabani group, the Pitzer Center has provided a vibrant environment to grow as a graduate student. Thank you to David Limmer for many valuable discussions that have helped shape my research and perspectives about teaching and academia. Thank you, also, to Martin Head-Gordon and Jeff Neaton for helpful conversations and comments through my qualifying exams and thesis writing. Thank you to Avishek Das, Elliot Rossomme, Julia Rogers, Layne Frechette, Aditya Singh, Trevor GrandPre, Katie Klymko, Norm Tubman, Rachel Clune, Tarini Hardikar, Orion Cohen, and Addison Schile for scientific discussions and friendly lunches.

Additionally, I am grateful to have collaborated with a number of talented scientists to learn about a diverse set of projects and experimental techniques: Chang Yan, Paul Alivisatos, Burak Guzelturk, Ben Cotts, Aaron Lindenberg, Jen Dionne, Michael Enright,

Ralph Nuzzo, Hannah Weaver, Naomi Ginsberg, Cora Went, Joeson Wong, Harry Atwater, Patrick Brosseau, Pat Kambhampati, Jaco Geuchies, Arjan Houtepen, and Uri Banin. To Chang, Ben, and Burak, especially, thank you for your patience in those early collaborations as I learned how to communicate effectively with experimentalists and how to think about physically relevant problems related to nanocrystals.

I would also like to thank the U.S. Department of Energy Computational Science Graduate Fellowship under Grant No. DE-SC0019323 for four years of generous support and community. The fellowship also gave me the opportunity to work at Lawrence Livermore National Laboratory, where I was lucky to learn about superconducting qubits from Vince Lordi and Yaniv Rosen.

Thank you to an incredible string of teachers, mentors, and advisors: Leah Marsh and David Baumritter, my high school chemistry teachers; Logan McCarty and Adam Cohen, who introduced me to the magic of quantum mechanics in PS10; Noam Prywes and Jack Szostak, who taught me the excitement of working toward answering the big, unanswered questions, like the origins of life; and Ed Pyzer-Knapp, Steven Lopez, Alan Aspuru-Guzik, Kirk Jordan, Sam Niblett, and David Wales, who exposed me to the power and diversity of computational and theoretical chemistry research. I am grateful for your early words of encouragement and opportunities, which are what brought me to grad school in the first place, and for your continued friendship.

Aside from research, I feel immensely fortunate to have found a wonderful community in Berkeley. To my cohort, Avishek Das, Elliot Rossomme, Sophia Steffens, Isabel Bogacz, Jenna Tan, Kaydren Orcutt, Valerie McGraw, Paul Wrona, Collin Steen, Eric Arsenault, and Harry Bergman, thank you for being the best parts of grad school and for making the worst parts more bearable. To Sam Gebb and the residents of 2510 and 1019, thank you for always making the East Bay home. To Jesus Moran, from picking me up from SFO when I moved to Berkeley to celebrating with me at graduation, thank you for being my biggest cheerleader and my most reliable grounding presence over the past five years. I am so grateful for all of you.

And finally, I would like to thank my family, Ma, Daddy, Rashmi Didi, Jyoti Didi, Sam, and Anshul. Words cannot express the depth of gratitude I feel for your unwavering love, care, and support. Thank you for being continuous sources of comfort, inspiration, and laughter. Thank you for always believing in me through the times of self-doubt and for always celebrating with me through the times of joy. I love you all so much.

Chapter 1

Introduction

Colloidal semiconductor nanocrystals (NCs) offer an idealized test bed to explore the behavior of excitons and multiexcitons from the discrete, molecular limit to the continuous, bulk limit [1–7]. At low excitation energies, NCs have discrete spectra, which resemble those of atoms and molecules, due to quantum confinement effects while at higher excitation energies their spectra converge to the bulk continuum limit due to increasingly large densities of states. Understanding the interplay of degeneracy, size, shape, and material composition on NC electronic structure has been the subject of numerous studies over the past several decades [2, 8–15].

From a theoretical perspective, the description of excitons and multiexcitons in semiconductor NCs poses several challenges. Because NCs contain several hundreds to thousands of atoms and valence electrons, quantum chemistry techniques that were developed to study the excited states of molecules are far too computationally expensive to be applicable to NCs. Thus, early work focused on the development of continuum approaches starting from the bulk limit, within a family of effective mass models, to describe the quantum confinement of excitons and dielectric screening [8, 16]. The most popular single band approximation provides a *qualitative* description of the optical properties of NCs, but it does not account for the non-parabolic effects and valence band degeneracies that are important in NCs. A more *quantitative* description based on the multi-band effective mass model revealed rich behavior and provided accurate predictions of the exciton fine structure and band edge exciton splittings as well as their dependence on the size, shape, and crystal structure of the NC [12, 17–19]. In addition, the inclusion of many-body exchange interactions of electrons and holes resulted in optically forbidden dark excitons and explained the non-monotonic temperature dependence of the radiative lifetime in NCs [20–23].

Despite the significant progress made with effective mass models, the lack of an underlying atomistic description has limited the application of these models primarily to the description of optical properties, which are less sensitive to the atomistic detail of the NC, particularly in the strong confinement limit ($R < a_{\mathrm{B}}$, where R is the NC radius and a_{B} is the bulk exciton Bohr radius). To account for inhomogeneities in the NC structure, semiempirical pseudopotential models, which became popular in the 1970s and 1980s to describe the

electronic and optical properties of bulk semiconductors and surfaces [24], were employed and further developed to study excitons in a variety of semiconductor NCs [10, 25–27], demonstrating remarkable success in postdicting and predicting the exciton fine structure [22, 28] as well as the roles of defects [29, 30], stress, and strain on the electronic structure [31, 32].

In recent years, growing interest in the dynamics of excitons inspired by novel experimental observations [33–49] has shifted the focus for theory to address issues related to the transients of these nonequilibrium species [50]. Understanding the radiative and nonradiative decay channels depicted in Fig. 1.1 as well as the dephasing and energy transfer mechanisms of confined excitons, which are dictated by exciton-phonon and exciton-exciton interactions, is key to the rational design of NC-based technologies with reduced thermal losses and increased quantum yields. Three central decay channels are the main focus this dissertation: hot exciton cooling, biexciton Auger recombination, and carrier trapping.

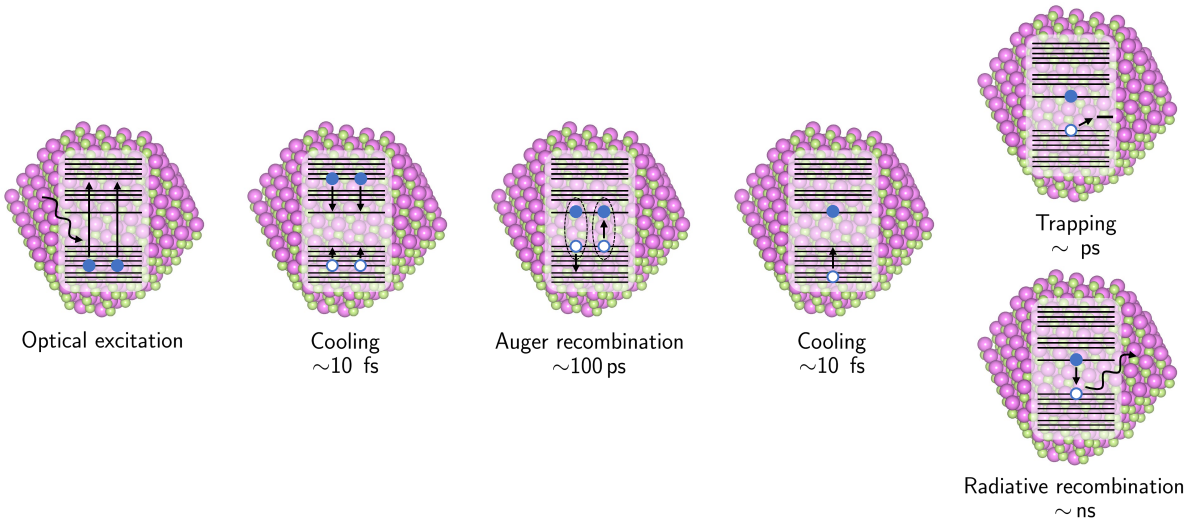

Figure 1.1: Photoexcitation of a NC can create multiple electron-hole pairs, which quickly relax to the band edge in a process called cooling. From the band edge, the multi-excitonic state can undergo Auger recombination, which nonradiatively annihilates one exciton and forms a hot electron-hole pair. The hot carriers then cool back to the band edge, from which they can radiatively recombine. Trapping of carriers to localized states can also occur.

The first decay channel is the nonradiative relaxation of hot excitons, or cooling, illustrated in Fig. 1.1. The study of this process is motivated by conflicting results for the relaxation times of hot excitons to the band edge in confined structures relative to those of hot excitons in bulk [33, 35, 51–58]. Due to the discrete nature of the excitonic levels in confined NCs, exciton cooling *via* phonon emission, especially near the band edge, has been thought to require multi-phonon processes and would, therefore, be inefficient, a phe-

nomenon known as the phonon bottleneck [59]. One mechanism for breaking the phonon bottleneck that allows for fast cooling is the Auger process [60]. In many NCs, holes relax rapidly to the band edge *via* phonon emission because valence band degeneracies and a larger hole effective mass lead to a higher density of hole states with smaller energy spacings that are on the order of the phonon frequencies. An electron, then, can relax to the band edge by nonradiatively transferring its energy to a hole *via* an Auger-like process, and the re-excited hole can quickly relax back to the valence band edge. The Auger-assisted cooling mechanism [61] has been supported by experimental observations [56, 57, 62–64] but has not been confirmed or validated by atomistic calculations [65], mainly because of the significant computational challenges of describing excitons and their coupling to phonons in systems containing thousands of atoms and valence electrons.

The second decay channel involves the nonradiative decay of multiexcitonic states [34, 66]. At high photo-carrier densities, which are typical of most optoelectronic devices, all semiconductor materials suffer from enhanced exciton-exciton annihilation that occurs primarily *via* Auger recombination (AR) processes, shown in Fig. 1.1, in which one exciton recombines by transferring its energy to another exciton [60]. This nonradiative process leads to heating of the NC lattice as well as reduced photoluminescence quantum yields (PLQYs) and decreased maximum device efficiencies. Thus, understanding the timescales and properties of multiexcitonic states and their decay channels is central to improving and further developing many light-induced NC applications.

The third decay channel pertains to the trapping of carriers to localized states, usually those associated with structural defects or dangling bonds due to unpassivated atoms at the NC surface. For most families of semiconductors, dangling bonds from non-metal atoms result in hole traps slightly above the valence band maximum, but metal dangling bonds do not result in electron traps due to the relatively lighter effective mass of the electron [29, 30, 67]. Hole trapping occurs on picosecond timescales and can have significant effects on exciton properties and dynamics. Core/shell heterostructure NCs have been shown to protect band edge carriers from surface states and has even led to the development of near-unity PLQY CdSe/CdS NCs [68]. However, trap states still pose a problem in NCs of other materials [69] or under high energy or high fluence excitation conditions [70]. Thus, understanding the electronic structure of these trap states, both through theoretical and experimental investigation, is crucial.

In this dissertation, we present our work to develop a unified model that address all three of these decay channels. In Ch. 2, we summarize the atomistic approach we have adopted to calculate quasiparticle excitations and neutral excitations in semiconductor NCs. First principles approaches, such as time-dependent density functional theory (DFT) [71–73] or many-body perturbation approximations [74], are limited to describing excitons in relatively small clusters, typically those with fewer than 100 atoms, due to their steep computational scaling [75, 76]. To make meaningful contact with experimental results on NCs that contain thousands of atoms and tens of thousands of electrons, we rely on the semiempirical pseudopotential model [10, 26, 27, 77] to describe quasiparticle excitations. We use a converged real-space grid method to represent the single-particle states combined with the filter diag-

onalization method [78, 79] to compute the single-particle states near the band edge and at higher excitation energies. We then use a subset of converged quasiparticle eigenstates to solve the Bethe-Salpeter equation [80] within the static screening approximation to account for electron-hole correlations in neutral optical excitations [81]. Ch. 2.1 also provides validation of the approach for the quasiparticle and optical gaps and the exciton binding energies for II-VI and III-V semiconductor NCs in both the strongly ($R < a_{\mathrm{B}}$) and weakly ($R > a_{\mathrm{B}}$) confined regimes.

In Ch. 2.3, we also develop and assess the accuracy of our approach for determining the exciton-phonon couplings (EXPCs) in semiconductors NCs, and we analyze the contributions of acoustic, optical, and surface modes to the overall magnitude of the EXPCs [82]. We compare predictions for the reorganization energies (*i.e.*, polaron shifts) computed from the EXPCs to experimentally measured Stokes shifts and demonstrate that *acoustic* modes that are delocalized across the NC contribute more significantly than optical modes to the reorganization energy in all NC systems and sizes. Excitons in smaller NCs are more strongly coupled to modes localized near the surface of the NC, while excitons in larger NCs are more strongly coupled to modes in the interior of the NC.

The assessment of the EXPC is essential for addressing the dynamics and mechanism for hot exciton cooling, which is the topic of Ch. 3. In this chapter, we present our framework for computing phonon-mediated exciton transition rates within Fermi's golden rule. We demonstrate that CdSe and CdSe/CdS core/shell NCs have a relatively high density of excitonic states, so that relaxation to the band edge involves a cascade of phonon-mediated exciton transitions. Still, some energy spacings in the excitonic spectrum, especially near the band edge in smaller systems, are larger than the phonon frequencies. Thus, we move to a polaronic picture to describe excitonic transitions that occur *via* the absorption or emission of multiple phonons [83, 84]. Our simulations show that efficient multiphonon processes enable ultrafast exciton cooling that occurs within tens of femtoseconds, circumventing the phonon bottleneck. Our simulations are in line with recent, two-dimensional spectroscopic measurements [85] and provide mechanistic insight regarding the role of EXPC and phonon frequencies on the cooling process.

Finally, we use the approaches developed in Ch. 2 to corroborate experimental measurements that further investigate the properties and dynamics of excitons and nonradiative processes in NC systems. In Ch. 4, we use molecular dynamics simulations and kinetic modeling to support electron diffraction measurements aimed at understanding how optical excitation of near-unity PLQY core/shell NCs leads to heading and disorder of the NC lattice [70]. We find that near-band edge excitation leads to long-lived NC heating due to sequential AR and exciton cooling events, whereas high-energy excitation leads to localized lattice distortions at the NC surface due to hole trapping. In Ch. 5, we use electronic structure calculations to investigate near-infrared emitting InAs/InP core/shell NCs [69]. Because these NCs are in the strong confinement regime, excitons readily delocalize out of the InAs core, facilitating charge trapping and quenching luminescence. This insight led to the design of synthetic protocols that yielded NCs with PLQYs that are among those highest reported for near-infrared emitting NCs. In Ch. 6, we calculate intraband photoinduced absorption

(PA) signals of band edge electrons, band edge holes, and surface-trapped holes, confirming spectroscopic assignments that are frequently used to monitor the populations and dynamics of electrons and holes in NCs [30]. These PA signals are used to investigate the competition between AR, hole trapping, and hole transfer in NCs, which we further understand using kinetic modeling and calculations of AR rates [86]. We find that, in some cases, hole trapping can improve hole transfer quantum yields by preventing the annihilation of holes *via* AR.

Chapter 2

The exciton-phonon Hamiltonian

The standard model Hamiltonian that describes a manifold of excitonic states and phonons that are coupled to first order in the atomic displacements is given by [82, 87, 88]:

$$H = \sum_n E_n \left|\psi_n\right\rangle \left\langle\psi_n\right| + \sum_\alpha \hbar\omega_\alpha b_\alpha^\dagger b_\alpha + \sum_{\alpha nm} V_{n,m}^\alpha \left|\psi_n\right\rangle \left\langle\psi_m\right| q_\alpha \,, \tag{2.1}$$

where $|\psi_n\rangle$ describes exciton n with energy E_n, and $b_\alpha^\dagger$ and b_α are the Boson creation and annihilation operators, respectively, of phonon mode α with frequency ω_α and displacement $q_\alpha = \sqrt{\frac{\hbar}{2\omega_\alpha}}\left(b_\alpha^\dagger + b_\alpha\right)$. Describing the nonequilibrium dynamics of excitons requires knowledge of the excitonic transition energies, E_n, and states $|\psi_n\rangle$, the phonon modes and their corresponding frequencies, ω_α, and the exciton-phonon couplings, $V_{n,m}^\alpha$. Sec. 2.1 describes the atomistic pseudopotential model used to compute excitonic states, and Secs. 2.2 and 2.3 provide the details for obtaining the phonon modes and the exciton-phonon couplings, respectively. The content of this chapter is adopted with permission from Jasrasaria, D.; Weinberg, D.; Philbin, J. P.; Rabani, E. Simulations of nonradiative processes in semiconductor nanocrystals. *J. Chem. Phys.* **2022**, *157*, 020901 and Jasrasaria, D.; Rabani, E. Interplay of surface and interior modes in exciton-phonon coupling at the nanoscale. *Nano Lett.* **2021**, *21*, 8741.

2.1 Manifold of excitonic states

The diversity of dynamic processes in semiconductor nanocrystals (NCs) requires a comprehensive model that captures a wide spectrum of physics. The finite size of NCs modifies the electronic structure relative to the bulk material—the continuous conduction and valence bands of the bulk are split into discrete states for finite crystals. This quantum confinement of carriers gives rise to NCs' hallmark size-dependent optical properties. To properly describe these optical properties, a model must go beyond the ground electronic state and describe the excited electronic states, as well. While these excited states are generally well understood in bulk semiconductors, quantum confinement complicates our understanding by

significantly enhancing the electron-hole interactions in nanoscale systems [77]. The small size of NCs compared to the exciton Bohr radius forces the electron and hole closer to each other than they would be in bulk, increasing the strength of their Coulomb interactions. Additionally, dielectric screening is reduced at the nanoscale as quantum confinement widens the band gap and increases the energy required to polarize the medium. This effect leads to a size-dependent reduction in screening, further contributing to size-dependent modifications of excited states in NCs. These enhanced interactions must be properly considered in order to describe the correlations between electrons and holes and achieve agreement with experimental measurements.

Experimentally relevant NCs are highly crystalline, and, in the interior of the structure, they closely resemble the corresponding bulk materials. The atomic configuration aligns closely with the bulk crystalline lattice across the majority of unit cells, suggesting that a description based on bulk bands would be a valid starting point. However, NCs possess additional features that distinguish them from bulk. The NC surface truncates the lattice symmetry, which gives rise to quantum confinement. Core-shell structures also form a nanoscale heterojunction that can introduce significant amounts of strain into the crystal structure [89, 90]. Both these internal interfaces and surfaces cause deformations from crystallinity on the scale of individual atoms, so accurate modeling of NCs must include this atomistic detail. For example, localized trap states at surfaces or interfaces due to atomic defects are ubiquitous in experimental studies of NCs, where they are observed to rapidly quench photoluminescence and result in significantly lower quantum yields [70, 91]. An atomistic description of the NC structure allows for the introduction of site-specific defects or alloying to understand their roles in trap formation and to determine the dynamics of trapping in NC systems [30, 69]. In addition to the static deformation of the crystal lattice, the effects of lattice fluctuations (*i.e.*, phonons) play a key role in the physics of NCs and must be properly incorporated [82]. Finally, in order to make meaningful contact with experimental measurements on NCs that contain thousands of atoms and tens of thousands of electrons, computational evaluation of the model must scale moderately with system size in comparison to first principles approaches. Because NC systems have important size dependent properties, such as optical gaps [92], radiative lifetimes, and Auger recombination (AR) lifetimes [93], and the scaling of these properties with system size is often an important question, the ability to access experimentally relevant sizes with volumes ranging across multiple orders of magnitude is crucial.

These considerations have informed our development of the semiempirical pseudopotential model as a sufficiently detailed description of NCs that can also tackle calculations of experimentally relevant systems. For example, a CdSe quantum dot only 4 nm in diameter has over 1000 atoms and 4000 valence electrons, so the conventional workhorses of quantum chemistry, such as density functional theory (DFT) and related methods for excited states, despite making significant progress [72, 73], are still far from being able to tackle this problem. On the other hand, continuum models based on the effective mass approximation have produced successful predictions for simple, linear spectroscopic observables [12] but are unable to capture many of the more complicated dynamic processes that determine

the timescales of processes, such as nonradiative exciton relaxation and AR. Furthermore, these continuum models are, by nature, blind to atomistic detail, such as defects, strain at heterostructure interfaces, and facet-dependent properties [94, 95].

Our approach is based on the semiempirical pseudopotential method [10, 27, 77], which was first developed to characterize the band structures of simple bulk materials [24] and was later extended to describe the role of surfaces [96] and confinement [10, 25]. The basic assumption made within this method is that the bulk band structure can be described by a simple, non-interacting model Hamiltonian:

$$\hat{h}_{\mathrm{qp}} = \hat{t} + \hat{v}(\boldsymbol{r}) = \hat{t} + \sum_{\mu} \hat{v}_{\mu}(\boldsymbol{r}) \,, \tag{2.2}$$

where $\hat{t}$ is the single-particle kinetic energy operator, and $\hat{v}(\boldsymbol{r})$ is the local (or non-local) pseudopotential, which is given by a sum over all atoms, μ, of a pseudopotential, $\hat{v}_{\mu}(\boldsymbol{r})$, centered at the location of each atom $\boldsymbol{R}_{\mu}$. The parameters used to describe the pseudopotential of each atom are obtained by fitting the reciprocal-space pseudopotentials to the bulk band structure obtained either from experimental measurements or high-accuracy electronic structure calculations, such as DFT+GW [24, 97]. Within the fitting procedure, we describe the real-space atomistic pseudopotential, $\hat{v}_{\mu}(\boldsymbol{r})$, by its reciprocal-space counterpart, $\hat{\tilde{v}}_{\mu}(\boldsymbol{q})$. The functional form of the local reciprocal-space pseudopotential used for the work presented throughout this dissertation is:

$$\hat{\tilde{v}}_{\mu}(\boldsymbol{q}) = a_0^{\mu} \left[1 + a_4^{\mu} \operatorname{Tr} \epsilon_{\mu} + a_5^{\mu} (\operatorname{Tr} \epsilon_{\mu})^3\right] \frac{q^2 - a_1^{\mu}}{a_2^{\mu} \exp(a_3^{\mu} q^2) - 1} \,, \tag{2.3}$$

where ϵ_{μ} is the local strain tensor around atom μ, the parameters $\{a_0^{\mu}, a_1^{\mu}, a_2^{\mu}, a_3^{\mu}\}$ are used to fit the band structure at the bulk equilibrium configuration, and a_4^{μ} is fit to match the absolute hydrostatic deformation potentials of the valence and conduction bands [98], which describe how those energies change with small, hydrostatic compression or expansion of the equilibrium structure. The trace of the local strain tensor at each atom is approximated by the ratio of the volume of the tetrahedron formed by the nearest neighbors in the deformed structure to that volume in the equilibrium bulk structure. The parameter a_5^{μ} has been added to correctly describe the optical gaps for core/shell NCs, in which the core experiences significant compression, about 6% compression in CdSe/CdS quantum dots, because of the presence of the shell [69, 99, 100]. Note that this formalism accounts for hydrostratic strain that occurs due to isotropic compression or expansion of a material, such as the core in spherical core/shell NCs. In anisotropic core/shell nanoplatelets, however, the core experiences biaxial strain [100], which may need to be incorporated into the model using additional terms.

The fitting of parameters $\{a_0, a_1, a_2, a_3\}$ proceeds by comparing the generated band structures to the expected band structures with special care taken to correctly capture the band gaps and effective masses. As shown in Fig. 2.1a, the model captures all band features and describes the band structure across the entire Brillouin zone. The real-space forms of

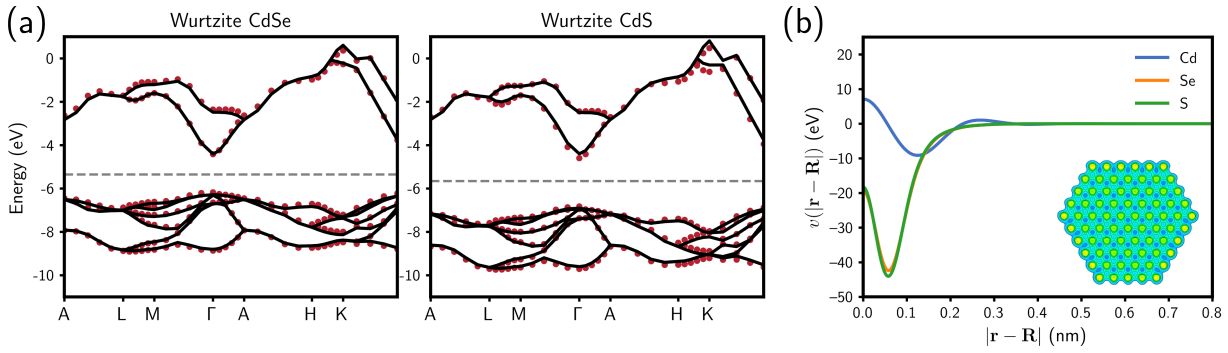

Figure 2.1: (a) The bulk band structures of wurtzite CdSe (left) and CdS (right) obtained from the pseudopotential Hamiltonian (red points) are compared to literature values [101] (black lines). The resulting band structures show excellent agreement across the entire Brilouin zone. (b) The corresponding real-space pseudopotentials for Cd, Se, and S. The inset illustrates a cross-section of the pseudoptential for a wurtzite 3.9 nm CdSe NC as constructed from these atom-centered functions.

the corresponding pseudopotentials are illustrated in Fig. 2.1b, where the psuedopotentials have been simultaneously fit to generate the correct band structures for both wurtzite and zincblende CdSe and CdS. The effects of strain are then incorporated through the a_4 parameter to fit the absolute deformation potentials of both the conduction band minimum and valence band maximum. This fitting procedure ensures that hydrostatic deformation of the crystal alters the energies of the electron and hole levels in the correct manner. Pseudopotential parameters for Cd, Se, S, In, As, and P that are used for electronic structure calculations in this work are collected in Table 2.1.

Table 2.1: Pseudopotential parameters for Cd, Se, S, In, As, and P. Cd, Se, and S parameters were fit to simultaneously reproduce wurtzite and zincblende CdSe and CdS bulk band structures and deformation potentials. In, As, and P parameters were fit to simultaneously reproduce zincblende InAs and InP bulk band structures. All parameters are given in atomic units.

	a_0	a_1	a_2	a_3	a_4	a_5
Cd	-31.4518	1.3890	-0.0502	1.6603	0.0586	0
Se	8.4921	4.3513	1.3600	0.3227	0.1746	-33
S	7.6697	4.5192	1.3456	0.3035	0.2087	0
In	49.6411	1.8874	3.5301	0.4235	0	0
As	25.7465	2.6905	1.5253	0.5721	0	0
P	28.8706	2.5839	1.5821	0.5622	0	0

Once the pseudopotentials have been fit to describe bulk systems (the fits are not unique and often other physical measures are used to choose the best set of parameters [26]), they are used to construct the NC Hamiltonian. The central assumption made here is that the pseudopotentials that describe single particle properties in the bulk are also adequate when applied to quantum confined nanostructures. While this may seem to be a large leap, the error introduced by this assumption is relatively small compared to the fundamental band gap [102]. A cross-section of the resulting pseudopotential for a wurtzite 3.9 nm CdSe NC is shown in the inset of Fig. 2.1b, illustrating both the near-periodic potential in the interior of the NC and the manner by which it is modified at the surface. The NC atomic configurations are obtained by first pruning a bulk structure such that all atoms are bonded to at least two other atoms. The atomic positions are then relaxed using molecular dynamics-based geometry optimization with previously-parameterized force fields [103, 104], which include two- and three-body terms to enforce tetrahedral bonding geometries and produce NC configurations that are relatively crystalline in agreement with experiment [105]. In the case of core/shell structures, the core is cut from bulk, and the shell material is grown on the surface using the lattice constant of the core material. The subsequent geometry optimization allows the shell to relax and results in compressive strain on the core to minimize the stress along the core/shell interface [99, 100].

The description of the surface of the NC presents a challenge, as simply terminating the NC will result in dangling bonds. These dangling bonds can give rise to localized electronic states within the band gap, which act as traps. For the II-VI and III-V families of semiconductors, we have found that dangling bonds from the non-metal atoms result in hole traps slightly above the valence band maximum, but metal dangling bonds do not result in electron traps due to the light electron effective mass relative to the hole effective mass [30, 69]. To passivate the surface of the NC, the outermost layer of atoms is replaced with passivation potentials that mimic the effect of organic ligands that terminate the surfaces of experimentally synthesized NCs, pushing the mid-gap states out of the band gap [10]. This procedure for building NC structures can be easily adapted to produce more complicated NCs, such as the core/shell NCs, nanorods, and nanoplatelets. Further modification, such as alloying, multi-layered NCs, dimer NC assemblies, and structural defects can also be modeled with atomistic detail.

While a NC of experimentally relevant size will have many single-particle states (see Fig. 2.2b), only a few highest-energy, occupied and lowest-energy, unoccupied states are relevant to describing the optical properties near the band edge. These single-particle states are obtained using the filter diagonalization method [78, 79], which provides a framework to extract all the eigensolutions within a specific energy window. This process can be done with nearly linear scaling with the system size due to the locality of the single-particle Hamiltonian, making feasible the calculation for NCs with volumes spanning several orders of magnitude. As the pseudopotentials are fit to reproduce quasiparticle band structures, the eigenstates of the pseudopotential Hamiltonian are assumed to describe the quasi-electron

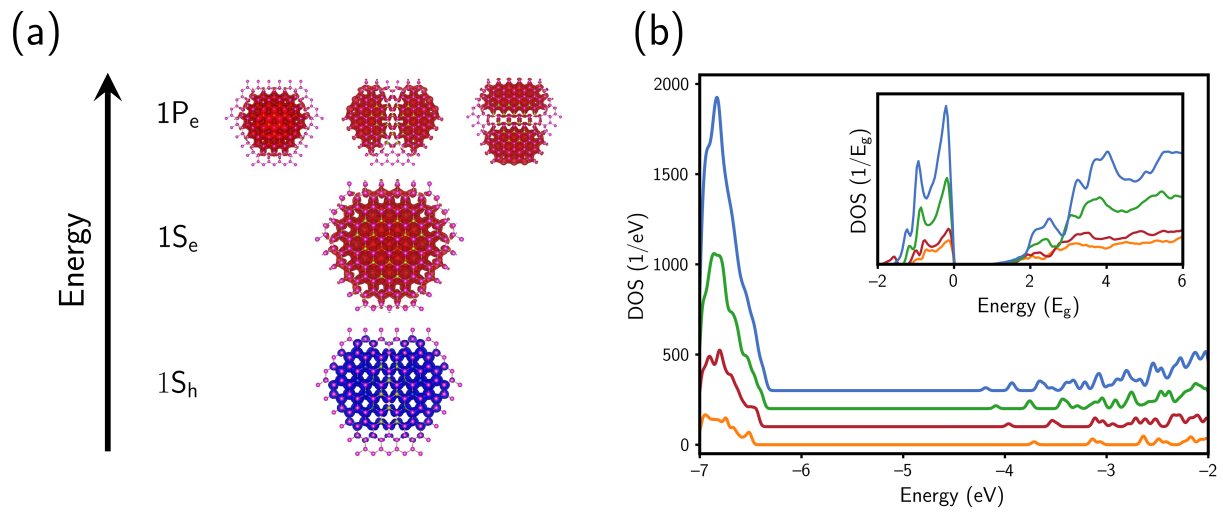

Figure 2.2: (a) Densities of the quasi-electron (red) and quasi-hole (blue) wavefunctions reveal that they are periodic across several unit cells in the interior of the NC. The electron states are labeled based on the symmetry of the envelope function in analogy to effective mass descriptions. (b) The densities of single-particle states (DOS) for wurtzite CdSe NCs of different sizes shows the effects of quantum confinement and the larger density of hole states in these II-VI systems. The inset illustrates the DOS across a larger energy range (that is scaled to the fundamental gap, E_g, of each NC), where the continuum of high energy states can be seen. The diameters of the NCs illustrated are 2.2 nm (orange), 3.0 nm (red), 3.9 nm (green), and 4.7 nm (blue).

and quasi-hole wave functions of the NC. Examples of the quasi-electron and quasi-hole densities are shown in Fig. 2.2a. We see that both the electron and hole states show Bloch-like oscillations, which are significantly more pronounced for the hole, and the electron states show a progression of envelope functions with s-type then p-type characteristics, in line with effective mass descriptions of NC electronic states [12, 106].

As previously stated, connection to experiments also requires an accurate description of the neutral excited states probed by optical spectroscopy. To account for electron-hole correlations, we use the single-particle eigenstates as the basis to solve the Bethe-Salpeter equation (BSE) [80] for the correlated excitonic states using the static screening approximation [113]. This approach explicitly includes electron-hole correlations, which allows for the accurate description of excitons across all confinement regimes using just one formalism, instead of relying on different approximations for different regimes. We take the excitonic states to be a linear combination of noninteracting, electron-hole pair states:

$$|\psi_n\rangle = \sum_{ai} c^n_{a,i} a^\dagger_a a_i |0\rangle \,, \tag{2.4}$$

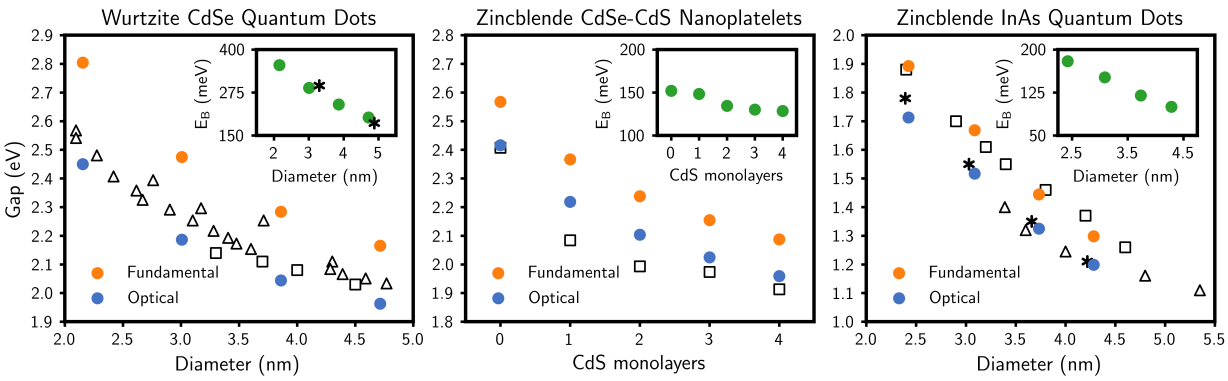

Figure 2.3: Gaps for wurtzite CdSe quantum dots of different sizes (left). The optical gaps computed by our semiempirical pseudopotential method agree with experimental measurements of the optical gap by Fan *et al.* [107] (black squares) and Yu *et al.* [108] (black triangles). The inset shows the exciton binding energy, E_{B}, computed by our method and compared to values computed by Franceschetti and Zunger [109] (black asterisks). Gaps for zincblende CdSe/CdS core/shell nanoplatelets with different thicknesses of CdS shell (middle). The optical gaps calculated by our method compare favorably with those measured experimentally by Hazarika *et al.* [100] (black squares). Gaps for zincblende InAs quantum dots of different sizes (right). The fundamental gaps calculated are in excellent agreement with those measured by Banin *et al.* [110] using scanning tunneling microscopy (black squares), and the optical gaps compare well with those measured by Guzelian *et al.* [111] (black triangles) and computed by Franceschetti and Zunger [112] (black asterisks).

where $a_a^\dagger$ and a_i are electron creation and annihilation operators in quasiparticle states a and i, respectively. The indexes $a, b, c, \ldots$ refer to quasi-electron (unoccupied) states while the indexes $i, j, k, \ldots$ refer to quasi-hole (occupied) states. The expansion coefficients $c_{a,i}$ are determined by solving the eigenvalue equation [80]

$$(E_n - \Delta\varepsilon_{ai}) c_{a,i}^n = \sum_{bj} \left(K_{ai;bj}^d + K_{ai;bj}^x \right) c_{b,j}^n \,, \tag{2.5}$$

which also determines the energy of exciton n, E_n, in terms of the direct and exchange parts of the electron-hole interaction kernel [80], $K_{ai;bj}^d$ and $K_{ai;bj}^x$, respectively, and the quasiparticle energy difference, $\Delta\varepsilon_{ai} = \varepsilon_a - \varepsilon_i$. The direct part of the kernel describes the main attractive interaction between quasi-electrons and quasi-holes while the exchange part controls details of the excitation spectrum, such as the singlet-triplet splittings. Importantly, the direct term is mediated by a screened Coulomb interaction [80], which we approximate using the static screening limit with a dielectric constant that is obtained directly from the quasiparticle Hamiltonian [77] and that depends on the size and shape of the NC. The binding energy of

excitonic state n, E_{B}^{n}, is calculated as

$$E_{\mathrm{B}}^{n} = \sum_{abij} \left(c_{a,i}^{n}\right)^{*} \left(K_{ai;bj}^{d} + K_{ai;bj}^{x}\right) c_{b,j}^{n} \,. \tag{2.6}$$

As this model was built on semiempirical foundations, it is necessary to validate the resulting calculations on well-known NC properties before using the model to explore more complex phenomena. Furthermore, the fitting was carried out on pure bulk materials, so it is important to assess the performance of the model on different NCs across a range of sizes and compositions. One of the most fundamental properties we need to capture is the optical gap. As shown in Fig. 2.3, we obtain results that compare favorably with experiments with respect to the magnitude of the gap and the scaling with NC size for several different NC compositions and geometries. We additionally validate properties, such as exciton binding energies [81, 114], exciton fine structure effects on polarized emission [114, 115], radiative and Auger recombination lifetimes [81, 93, 116], and optical signals of trapped carriers [30]. The strong agreement we obtain between theoretical predictions and experimental observations across a variety of system sizes, compositions, and dimensionalities demonstrates that our approach is suitable for understanding and rationalizing trends across a wide range of nanomaterial systems. Additionally, this model is extremely versatile and lends itself to new development and expansion.

2.2 Bath of phonons

Similar to the electronic degrees of freedom, which are quantized due to the finite size of the NC, lattice vibrations in NCs resemble phonons in bulk semiconductors, but they are finite in number and spatially confined to the NC. This confinement results in the quantization of the phonon frequencies and introduces additional complicating factors, such as the role of the NC surface [117, 118], that motivate the need for an atomistic description of phonon modes [105]. While DFT-based frozen phonon approaches have been used to compute phonon modes and frequencies [119–121], their computational expense restricts these methods to small NCs or to the computation of specific modes that are known *a priori* to be relevant for the properties or processes of interest. Therefore, we model phonons using classical, atomic force fields, which allows for the computation of all phonon modes and frequencies in NC systems of experimentally relevant sizes. The dynamical matrix, or mass-weighted Hessian, can be computed at the equilibrium configuration of a NC [122]:

$$D_{\mu k,\mu' k'} = \frac{1}{\sqrt{m_{\mu} m_{\mu'}}} \left(\frac{\partial^2 U(\boldsymbol{R})}{\partial u_{\mu k} \partial u_{\mu' k'}} \right)_{\boldsymbol{R}_0} , \tag{2.7}$$

where $U(\boldsymbol{R})$ is the potential energy given by the force field, $u_{\mu k} = R_{\mu k} - R_{0,\mu k}$ is the displacement of nucleus μ away from its equilibrium position in the $k \in \{x, y, z\}$ direction, and m_{μ} is the mass of nucleus μ. This $3N \times 3N$ dynamical matrix, where N is the number of

atoms in the NC, can be diagonalized to obtain the phonon mode frequencies and coordinates. Six of these modes have zero frequency, as they correspond to the three rotational and three translational degrees of freedom.

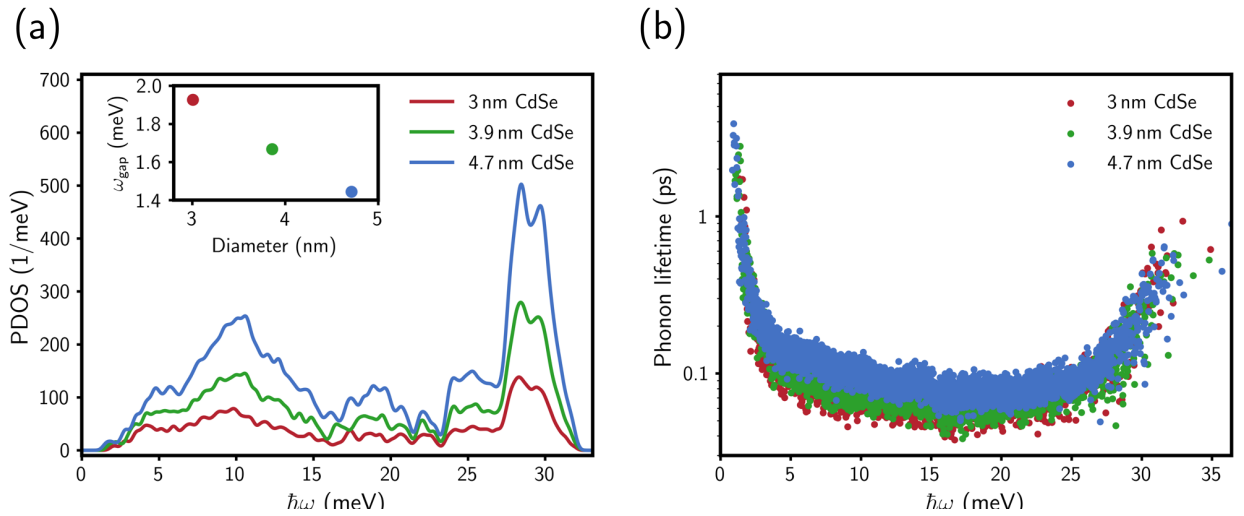

Figure 2.4: (a) The phonon densities of states (PDOS) calculated for wurtzite CdSe NCs of different sizes. The inset shows the phonon gap, ω_{gap}, which decreases with increasing NC size. (b) Phonon lifetimes calculated for wurtzite CdSe NCs. For all systems, almost all modes have sub-picosecond lifetimes, indicating significant phonon-phonon coupling.

The phonon densities of states (PDOS) for wurtzite CdSe NCs of different sizes computed using a previously-parameterized Stillinger-Weber interaction potential [103] are illustrated in Fig. 2.4a. Acoustic modes, which involve in-phase motion of atoms, have lower frequencies (1 THz $\sim$ 5 meV or lower in CdSe NCs) while optical modes, which are made up of out-of-phase movements of atoms, have higher frequencies (4 THz $\sim$ 16 meV or higher) [123]. Modes at intermediate frequencies are difficult to characterize due to the overlap of acoustic and optical branches in the bulk phonon dispersion relation as well as the confounding effects of phonon confinement. Phonon confinement also leads to a gap in the PDOS near zero-frequency since the longest-wavelength (*i.e.*, lowest-frequency) phonon mode in a NC is dictated by the NC size. As shown in the inset of Fig. 2.4a, the lowest-frequency phonon mode in the system is inversely proportional to the NC diameter, as observed by Raman spectroscopy measurements [124, 125].

The presence of a zero-frequency gap and the mixing of acoustic-optical modes in NCs has led to a hypothesized hot phonon bottleneck [126, 127], which has been observed in bulk semiconductors and perovskite systems [128–131]. In the hot phonon bottleneck, phonon thermalization is the rate-limiting step in processes, such as hot carrier relaxation. (Note that the "hot phonon bottleneck" is distinct from the "phonon bottleneck," which describes

slow carrier relaxation due to the mismatch between electronic gaps and phonon frequencies in NCs, that is discussed in Chs. 1 and 3.) The lack of low-frequency modes in NC systems may prevent the down-conversion of acoustic phonon modes and instead encourage efficient up-conversion to optical modes, leading to a hot phonon bottleneck [126, 127]. However, we have found that phonons have significant coupling with one another (*i.e.*, are anharmonic) and relax on picosecond timescales at room temperature [70]. We performed molecular dynamics simulations using a force field that consists of Lennard-Jones and Coulomb terms [132] to compute both phonon modes and phonon relaxation lifetimes of CdSe NCs, shown in Fig. 2.4b. Unlike the Stillinger-Weber potential, this force field includes long-range interactions that are necessary to accurately describe the splitting between acoustic and optical branches at the Brillouin zone edge in bulk polar semiconductors [133] and, thus, the phonon lifetimes. A detailed derivation of the phonon mode lifetimes is given in Sec. 2.2.1.

The lifetimes, which are dictated by the phonon-phonon interactions, are sub-picosecond for all modes except for the lowest-energy acoustic modes, for which the lifetimes reach $\sim$4 ps. Smaller NCs have shorter lifetimes because surface atoms, which are proportionally larger in number in smaller NCs, have increased anharmonic motion that leads to greater phonon-phonon coupling. For all NCs, at room temperature, the phonon dynamics for low-frequency modes are overdamped, so the relaxation timescales are less than the periods of the phonon modes, while the high-frequency modes are underdamped, so the phonons oscillate for multiple periods before decaying. These calculated results are in agreement with experimental observations [134–136]. We expect that phonon modes that are strongly out of equilibrium would relax even more quickly, indicating that a hot phonon bottleneck is unlikely in these systems.

2.2.1 Derivation of phonon lifetimes

First, consider a model system consisting of a tagged harmonic mode coupled to a bath of harmonic modes that are bilinearly coupled:

$$H = H_q + H_b + V \tag{2.8}$$

$$H_q = \frac{1}{2}\dot{q}^2 + \frac{1}{2}\omega^2 q^2 \tag{2.9}$$

$$H_b = \sum_\alpha \left(\frac{1}{2}\dot{x}_\alpha^2 + \frac{1}{2}\omega_\alpha^2 x_\alpha^2 \right) \tag{2.10}$$

$$V = -qF = -q\sum_\alpha g_\alpha x_\alpha \,. \tag{2.11}$$

Note that q and x_α refer to the mass-weighted coordinate of the harmonic modes.

By Fermi's golden rule, the quantum mechanical transition rate from state i to j of the tagged mode is given by

$$k_{i\to j} = \frac{1}{\hbar^2}\int_{-\infty}^{\infty} dt e^{i\omega_{ij}t}\langle V_{ij}(t)V_{ji}(0)\rangle_b \,, \tag{2.12}$$

where ω_{ij} is the energy difference between states i and j, V_{ij} is the i,j matrix element of the tagged mode-bath coupling, and $\langle \dots \rangle_b$ denotes a quantum mechanical average over bath coordinates. This can be written in the time-symmetrized form:

$$k_{i\to j} = \frac{2}{\hbar^2[1+\exp(-\beta\hbar\omega_{ij})]} \int_{-\infty}^{\infty} dt e^{i\omega_{ij}t} \left\langle \frac{1}{2}\{V_{ij}(t), V_{ji}(0)\} \right\rangle_b . \tag{2.13}$$

Because the solute is harmonic, only transitions between states $n \to n \pm 1$ are allowed, and $\langle n|q|n-1\rangle = \sqrt{\hbar n/2\omega}$. Accounting for these simplifications, the above rate becomes

$$k_{n\to n-1} = \frac{n}{\hbar\omega[1+\exp(-\beta\hbar\omega)]} \int_{-\infty}^{\infty} dt e^{i\omega t} \left\langle \frac{1}{2}\{F(t), F(0)\} \right\rangle_b \tag{2.14}$$

$$= \frac{2n}{\beta\hbar\omega[1+\exp(-\beta\hbar\omega)]} \tilde{\xi}'_{\rm qm}(\omega) , \tag{2.15}$$

where $\xi_{\rm qm}(t)$ is defined as

$$\xi_{\rm qm}(t) \equiv \left\langle \frac{\beta}{2}\{F(t), F(0)\} \right\rangle_b , \tag{2.16}$$

and its Laplace transform is given by

$$\tilde{\xi}_{\rm qm}(i\omega) = \int_0^{\infty} dt e^{-i\omega t} \xi_{\rm qm}(t) \equiv \tilde{\xi}'_{\rm qm}(\omega) - i\tilde{\xi}''_{\rm qm}(\omega) . \tag{2.17}$$

The transition rate diverges in the classical limit as the energy gap between states vanishes (*i.e.*, as $\beta\hbar\omega \to 0$). Thus, it instead makes sense to consider the T_1 relaxation time of the tagged mode by examining the rate of change of the tagged mode's average energy:

$$\frac{d\langle E(t)\rangle_b}{dt} = \sum_n E_n \dot{\rho}_{nn} . \tag{2.18}$$

Assuming that the bath relaxes much faster than the timescale of transitions between states of the tagged mode, the populations and coherences of the tagged mode are decoupled, and the rate of change becomes

$$\frac{d\langle E(t)\rangle_b}{dt} = -\hbar\omega \sum_n \rho_{nn}(t)[k_{n\to n-1} - k_{n\to n+1}] \tag{2.19}$$

$$= -\hbar\omega \sum_n \rho_{nn}(t)[k_{n\to n-1} - e^{-\beta\hbar\omega} k_{n+1\to n}] \tag{2.20}$$

$$= \frac{-2\hbar\omega}{\beta\hbar\omega[1+\exp(-\beta\hbar\omega)]} \tilde{\xi}'_{\rm qm}(\omega) \sum_n \rho_{nn}(t)[n - e^{-\beta\hbar\omega}(n+1)] \tag{2.21}$$

$$= \frac{2}{\beta\hbar\omega} \tanh\left(\frac{\beta\hbar\omega}{2}\right) \tilde{\xi}'_{\rm qm}(\omega) \sum_n \rho_{nn}(t) \left[\hbar\omega\left(n+\frac{1}{2}\right) - \frac{\hbar\omega}{2}\coth\left(\frac{\beta\hbar\omega}{2}\right)\right] . \tag{2.22}$$

Noting that $\sum_n \rho_{nn} = 1$ and that $(\hbar\omega/2)\coth(\beta\hbar\omega/2)$ is the thermal average energy, $\langle E\rangle_{\rm eq}$, we have

$$\frac{d\langle E(t)\rangle_b}{dt} = \frac{1}{T_1}[\langle E(t)\rangle_b - \langle E\rangle_{\rm eq}]\,, \tag{2.23}$$

where

$$T_1^{-1} \equiv \frac{2}{\beta\hbar\omega}\tanh\left(\frac{\beta\hbar\omega}{2}\right)\tilde{\xi}'_{\rm qm}(\omega)\,. \tag{2.24}$$

Because this model assumes a harmonic tagged mode, a harmonic bath, and bilinear coupling, $\tilde{\xi}'_{\rm qm}(\omega)$ can be related to its classical counterpart:

$$\tilde{\xi}'_{\rm qm}(\omega) = \frac{\beta\hbar\omega}{2}\coth\left(\frac{\beta\hbar\omega}{2}\right)\tilde{\xi}'_{\rm cl}(\omega)\,, \tag{2.25}$$

where $\xi_{\rm cl}(t)$ is the friction kernel of the generalized Langevin equation that describes the motion of the tagged mode:

$$\ddot{q} = -\omega^2 q(t) + R(t) - \int_0^t d\tau\xi_{\rm cl}(t-\tau)\dot{q}(\tau)\,. \tag{2.26}$$

For this model system, both $\xi_{\rm qm}$ and $\xi_{\rm cl}$ can be calculated analytically. Moving away from this model, $\xi_{\rm cl}$ can be computed for any arbitrary potential using the velocity autocorrelation function of the tagged mode. This can be seen by writing Eq. (2.26) in terms of the velocity, $\dot{q}(t)$, multiplying both sides by the initial velocity, $\dot{q}(0)$, and taking the average of both sides with respect to initial conditions:

$$\ddot{q} = -\omega^2 q(t) + R(t) - \int_0^t d\tau\xi_{\rm cl}(t-\tau)\dot{q}(\tau) \tag{2.27}$$

$$\frac{d}{dt}\langle\dot{q}(t)\dot{q}(0)\rangle = -\omega^2\langle q(t)\dot{q}(0)\rangle + \langle R(t)\dot{q}(0)\rangle - \int_0^t d\tau\langle\xi_{\rm cl}(t-\tau)\dot{q}(\tau)\dot{q}(0)\rangle \tag{2.28}$$

$$= -\omega^2\langle q(t)\dot{q}(0)\rangle - \int_0^t d\tau\xi_{\rm cl}(t-\tau)\langle\dot{q}(\tau)\dot{q}(0)\rangle \tag{2.29}$$

$$= -\omega^2\int_0^t d\tau\langle\dot{q}(\tau)\dot{q}(0)\rangle - \int_0^t d\tau\xi_{\rm cl}(t-\tau)\langle\dot{q}(\tau)\dot{q}(0)\rangle \tag{2.30}$$

$$= -\int_0^t d\tau[\omega^2 + \xi_{\rm cl}(t-\tau)]\langle\dot{q}(\tau)\dot{q}(0)\rangle\,, \tag{2.31}$$

$$\tag{2.32}$$

where we have made use of the facts that

$$\langle R(t)\dot{q}(0)\rangle = 0 \tag{2.33}$$

and

$$\int_0^t d\tau\langle\dot{q}(\tau)\dot{q}(0)\rangle = \langle q(t)\dot{q}(0)\rangle - \langle q(0)\dot{q}(0)\rangle = \langle q(t)\dot{q}(0)\rangle\,. \tag{2.34}$$

We will also make the following definitions:

$$C_v(t) \equiv \langle \dot{q}(t)\dot{q}(0)\rangle \tag{2.35}$$
$$\kappa(t) \equiv \omega^2 + \xi_{\mathrm{cl}}(t)\,, \tag{2.36}$$

so that

$$\dot{C}_v(t) = -\int_0^t d\tau \kappa(t-\tau) C_v(\tau)\,. \tag{2.37}$$

Taking the Laplace transform of both sides gives

$$\int_0^\infty dt e^{-i\omega t}\dot{C}_v(t) = -\int_0^\infty dt e^{-i\omega t}\int_0^t d\tau\kappa(t-\tau)C_v(\tau) \tag{2.38}$$
$$i\omega\int_0^\infty dt e^{-i\omega t}C_v(t) - C_v(0) = -\int_0^\infty dt\int_0^t d\tau\kappa(t-\tau)e^{-i\omega(t-\tau)}C_v(\tau)e^{-i\omega\tau} \tag{2.39}$$
$$i\omega\tilde{C}_v(\omega) - C_v(0) = -\tilde{\kappa}(\omega)\tilde{C}_v(\omega)\,, \tag{2.40}$$

where

$$\tilde{\kappa}(\omega) = -i\omega + \tilde{\xi}_{\mathrm{cl}}(\omega)\,. \tag{2.41}$$

Thus, we can solve for the real part of the Laplace transform of the classical friction kernel:

$$\tilde{\xi}'_{\mathrm{cl}}(\omega) = \mathrm{Re}\left[\frac{C_v(0) - i\omega\tilde{C}_v(\omega)}{\tilde{C}_v(\omega)} + i\omega\right]. \tag{2.42}$$

Equilibrium molecular dynamics (MD) simulations can be used to calculate the velocity autocorrelation function for a given phonon mode, and then Eq. (2.42) can be used to compute $\tilde{\xi}'_{\mathrm{cl}}(\omega)$ and the phonon lifetime. This MD-based approach for computing phonon lifetimes was verified for the simple model given by Eq. (2.8), which can be solved analytically.

2.3 Exciton-phonon coupling

Electronic degrees of freedom couple to phonons in semiconductors, resulting in a diverse set of processes that affect electronic properties and dynamics. These electron-phonon interactions in bulk semiconductors tend to be weaker than electron-vibrational interactions in molecular systems because the relatively large dielectric screening in bulk semiconductors leads to delocalized, Wannier-Mott excitons, which do not depend as sensitively on the nuclear configuration as do the localized, Frenkel excitons in molecular systems [2]. Additionally, phonons in bulk semiconductors are also delocalized over the material, unlike localized vibrations in molecules [137].

In bulk semiconductors, lower-frequency acoustic modes, which involve the in-phase movements of atoms, couple to electronic degrees of freedom *via* the deformation potential, which describes how strain and deformation of the crystal lattice change the energies

of the electronic bands [137]. In polar crystals, such as CdSe and other II-VI materials, the piezoelectric potential also couples electrons and acoustic phonons, although its effect is much weaker [137, 138]. Optical phonons are higher in frequency and consist of out-of-phase motions of atoms. They couple to the electronic degrees of freedom through the Fröhlich mechanism or the interaction between the dipole polarization field generated by optical phonons and the excitonic charge density [137].

While excitons and phonons are expected to interact *via* similar mechanisms in confined semiconductor NCs, the effects of confinement on the magnitude of exciton-phonon coupling (EXPC) are still poorly understood. Experimentally, dynamical effects as well as those of structural NC defects often confound measurements of the EXPC and have thus led to conflicting results. Some observations indicate stronger EXPC to acoustic modes [136, 139–141], and others show stronger EXPC to optical modes [142–146]. From a theoretical perspective [120, 121, 138, 147–154], progress has been limited due to the computational complexity associated with accurately describing excitons and phonons in NC systems of experimentally relevant sizes. These challenges have led to a set of outstanding questions regarding EXPC in semiconductor NCs: the relative coupling strengths of excitons to acoustic versus optical modes, the scaling of EXPC with system size, and the role of the NC surface in EXPC.

A detailed description of EXPC in NCs is essential for understanding the temperature dependence of excitonic properties [155] and phenomena, such as exciton dephasing (*i.e.*, homogeneous emission linewidths) [156, 157], phonon-mediated carrier relaxation [59, 65, 158], and charge transfer [159, 160].

Historically, theoretical studies of EXPC in NCs have described electronic states within parameterized models and/or have described phonons as vibrations of an elastically isotropic sphere [138, 142, 147–149, 151], leading to widely varying results, as the magnitude of EXPC is extremely sensitive to the descriptions of both excitons and phonons. Fully atomistic *ab initio* methods have been used for small NCs of ∼100 atoms or fewer, for which the electron-phonon coupling can be inferred from fluctuations of the adiabatic electronic states that are generated "on the fly" within DFT and time-dependent DFT frameworks [152, 161–163]. While these methods have been moderately effective in modeling electron-phonon coupling, they are often limited to small systems due to the computational expense of DFT, and they ignore excitonic effects. One recent study that did include these excitonic effects using *ab initio* methods was limited to clusters of tens of atoms [154].

Instead, as described in Secs. 2.1 and 2.2, we rely on the semiempirical pseudopotential model to describe excitonic states and atomic force fields to describe phonons [82]. Within this framework, the standard electron-nuclear matrix element to first order in the atomic displacements is given by [87]:

$$V_{n,m}^{\mu k} \equiv \left\langle \psi_n \middle| \left(\frac{\partial \hat{v}(\boldsymbol{r})}{\partial R_{\mu k}} \right)_{\boldsymbol{R}_0} \middle| \psi_m \right\rangle , \tag{2.43}$$

where $|\psi_n\rangle$ is the state of exciton n (cf., Eq. (2.4)), $\hat{v}(\boldsymbol{r}) = \sum_\mu \hat{v}_\mu(\boldsymbol{r})$ is the sum over atomic pseudopotentials given in Eq. (2.2), $R_{\mu k}$ is the position of atom μ in the $k \in \{x, y, z\}$

direction, and $\boldsymbol{R}_0$ is the equilibrium configuration of the NC. Using the static dielectric approximation for the excitonic wavefunction, we can reduce the calculation of these matrix elements to a simpler form given by [82]:

$$V_{n,m}^{\mu k} = \sum_{abi} c_{a,i}^{n} c_{b,i}^{m} v'_{ab,\mu}(R_{\mu k}) - \sum_{aij} c_{a,i}^{n} c_{a,j}^{m} v'_{ij,\mu}(R_{\mu k}) \,, \tag{2.44}$$

where

$$v'_{rs,\mu} = \int d\boldsymbol{r} \phi_r^*(\boldsymbol{r}) \frac{\partial \hat{v}(\boldsymbol{r})}{\partial R_{\mu k}} \phi_s(\boldsymbol{r}) \,. \tag{2.45}$$

Here, $c_{a,i}^{n}$ represent the Bethe-Salpeter coefficients introduced in Eq. (2.4), and $\phi_a(\boldsymbol{r})$ are the real-space quasiparticle wavefunctions. The first term in Eq. (2.44) represents the electron channel of EXPC, in which excitons comprised of different single-particle electron states are coupled. The second term describes the hole channel, in which excitons comprised of different single-particle hole states are coupled. These selection rules result from the fact that the EXPC is a matrix element of a one-body operator, $\partial \hat{v}/dR$.

The matrix elements given by Eq. (2.43) can be transformed to phonon mode coordinates using the eigenvectors of the dynamical matrix:

$$V_{n,m}^{\alpha} = \sum_{\mu k} \frac{1}{\sqrt{m_\mu}} e_{\alpha,\mu k}^{-1} V_{n,m}^{\mu k} \,, \tag{2.46}$$

where $e_{\alpha,\mu k}$ is the μk element of the α eigenvector of the dynamical matrix given in Eq. (2.7), and m_μ is the mass of atom μ. The diagonal matrix elements $V_{n,n}^{\alpha}$ describe the renormalization of the energy of exciton n through its interaction with phonon mode α, and the off-diagonal matrix elements $V_{n,m}^{\alpha}$ describe the interaction of excitons n and m through the absorption or emission of a phonon of mode α. A detailed derivation of the exciton-nuclear coupling matrix elements is given in Sec. 2.3.1.

One measure of the EXPC is the reorganization energy [17, 139], depicted schematically in Fig. 2.5a, which is the energy associated with rearrangement of the NC lattice after exciton formation and is relevant for optical Stokes shifts, charge transfer processes, and NC-based device efficiencies. In the harmonic approximation, the reorganization energy for excitonic state $|\psi_n\rangle$ is a sum of reorganization energies for each mode:

$$\lambda_n = \frac{1}{2} \sum_{\alpha} \left(\frac{1}{\omega_\alpha} V_{n,n}^{\alpha} \right)^2 . \tag{2.47}$$

To compare calculated values with those measured experimentally at room-temperature, we calculate a Boltzmann-weighted average over excitonic states, $\lambda = \frac{1}{Z} \sum_n e^{-\beta E_n} \lambda_n$, where $Z = \sum_n e^{-\beta E_n}$ is the partition function, $\beta = 1/k_B T$, and T is the temperature. All excitonic states included in the average at room temperature ($T = 298\,\mathrm{K}$) have contributions mainly from the LUMO and from several hole states near the HOMO, consistent with the heavier effective mass of the hole and the larger density of hole states.

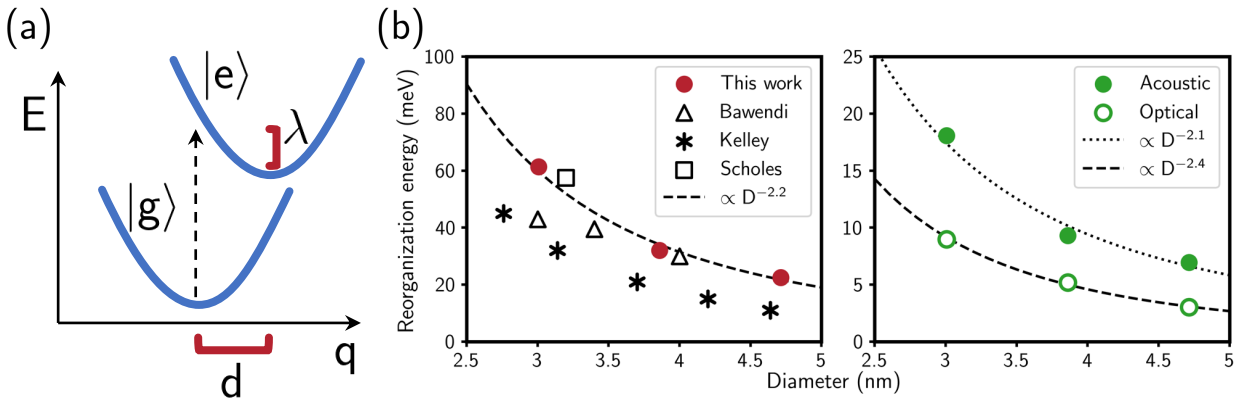

Figure 2.5: (a) The reorganization energy, λ, corresponds to the energy associated with the rearrangement of the lattice after a vertical excitation from the ground state, $|g\rangle$, to the excited state, $|e\rangle$. The minima of the ground and excited states are displaced by a distance, d, along the phonon mode coordinate, q. (b) Reorganization energies computed in this work for wurtzite CdSe NCs of various diameters in comparison to values from effective mass model-based calculations by Kelley [151] and from experimental measurements by Bawendi *et al.* [164] and Scholes *et al.* [139] (left). Acoustic modes contribute more significantly to the reorganization energy than do optical modes (right).

The reorganization energies for wurtzite CdSe cores with diameters of 3.0, 3.9, and 4.7 nm were calculated to be between 60 and 20 meV (Fig. 2.5b), which compare favorably with values obtained from a parametrized effective mass model [151] and from room-temperature absorption and photoluminescence measurements of the Stokes shift[139, 164], which is assumed to be equal to twice the reorganization energy. The reorganization energy decreases with increasing NC diameter D, with a scaling that roughly follows a power law: $\lambda \propto D^{-2.2}$. Excitons with smaller coherence areas are more sensitive to their local environment, explaining that EXPC is stronger in smaller NCs. Higher-energy excitonic states tend to be more delocalized and thus have smaller reorganization energies [136, 151].

To better understand the scaling of the reorganization energy with system size, we examine contributions to the total reorganization energy from acoustic modes (ω <4.1 meV, 1 THz) and optical modes (ω >16.5 meV, 4 THz), as shown in Fig. 2.5b, where the frequency cut-offs were determined from the CdSe bulk phonon dispersion relation [123]. Modes at intermediate frequencies ($1 < \omega < 4$ THz) are difficult to characterize due to overlap of the acoustic and optical branches in the bulk phonon dispersion relation and the confounding effects of phonon confinement [123]. For strongly confined NCs, like the ones studied here with $D < 5$ nm, we find that lower-frequency acoustic modes contribute more significantly to the reorganization energy than higher-frequency optical modes. Additionally, the reorganization energies of lower-frequency modes scale slightly less steeply with system size as

$\lambda_{\mathrm{ac}} \propto D^{-2.1}$ than those of optical modes, which scale as $\lambda_{\mathrm{op}} \propto D^{-2.4}$.

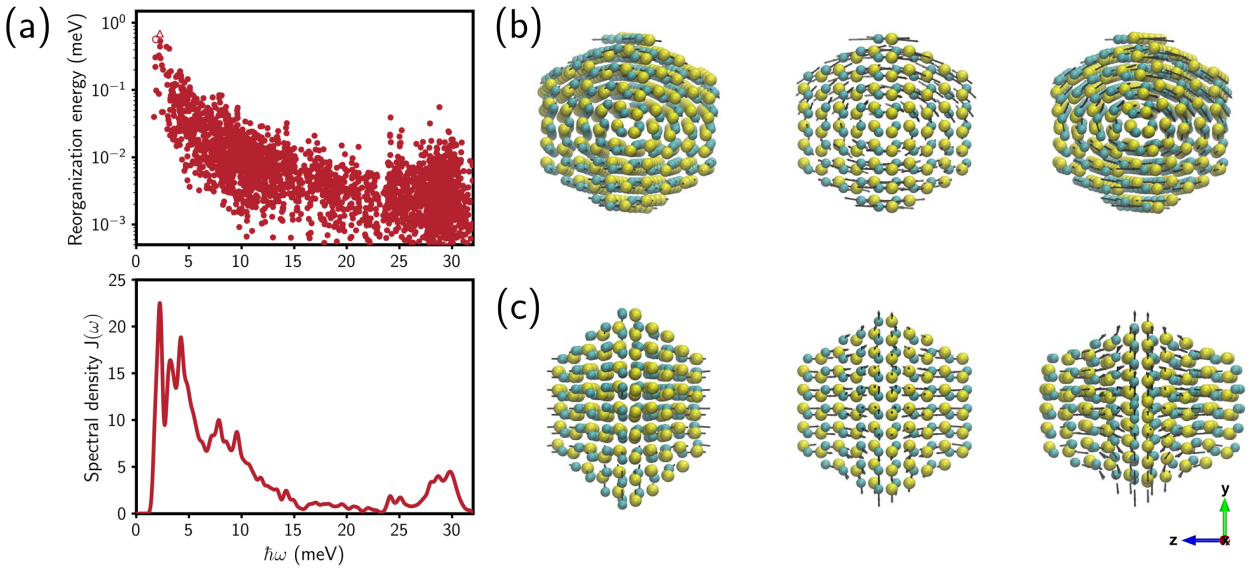

Figure 2.6: (a) Reorganization energies per mode (top) and spectral density (bottom) calculated for a 3.9 nm CdSe NC. The circle and triangle in the top panel correspond to the modes depicted in 2.6b,c, respectively. (b) Torsional mode with a frequency of 1.86 meV (0.45 THz) and reorganization energy of 0.69 meV. (c) Breathing mode with a frequency of 2.27 meV (0.55 THz) and reorganization energy of 0.57 meV.

To determine the contributions of specific modes, we analyzed the reorganization energy for each mode for a 3.9 nm CdSe NC, the results of which are plotted in Fig. 2.6a. Modes with frequencies lower than 6.2 meV (1.5 THz) contribute most significantly, and two modes in particular have large reorganization energies of 0.69 and 0.57 meV. These modes are depicted in Fig. 2.6b,c. They are the torsional and breathing (spheroidal) acoustic modes that are delocalized throughout the NC and involve collective motions of many atoms.

While these results indicate that lower-frequency acoustic modes are more strongly coupled to the exciton, the optical phonons may be important in dynamical processes despite their relatively weaker coupling. This significance may be due to a higher density of phonon states at those optical frequencies (Fig. 2.4), which are more relevant given the energy scales of typical excitonic transitions. This interplay can be further investigated through the weighted phonon density of states or spectral density,

$$J(\omega) = \sum_{\alpha} \lambda_{\alpha} \delta(\omega - \omega_{\alpha}) \,, \tag{2.48}$$

which is plotted in Fig. 2.6a for the same 3.9 nm CdSe NC. The Dirac delta functions in Eq. (2.48) were broadened as Gaussian functions with a standard deviation of 0.2 meV

(0.05 THz), and they are normalized such that $\lambda = \int d\omega J(\omega)$. The spectral density peaks at 2.2 meV (0.54 THz) and decays at higher frequencies. However, the spectral density shows another peak at 29.8 meV (7.2 THz) in the range of the longitudinal optical phonon, which has been predicted and shown to play a role in phonon-mediated exciton relaxation and dephasing [156, 157, 165]. Our calculations show that exciton formation distorts the NC lattice primarily along coordinates of low-frequency torsional and spheroidal phonon modes, but non-negligible EXPC to optical modes, in addition to the large density of phonon states at those higher frequencies, support their role in exciton dynamics.

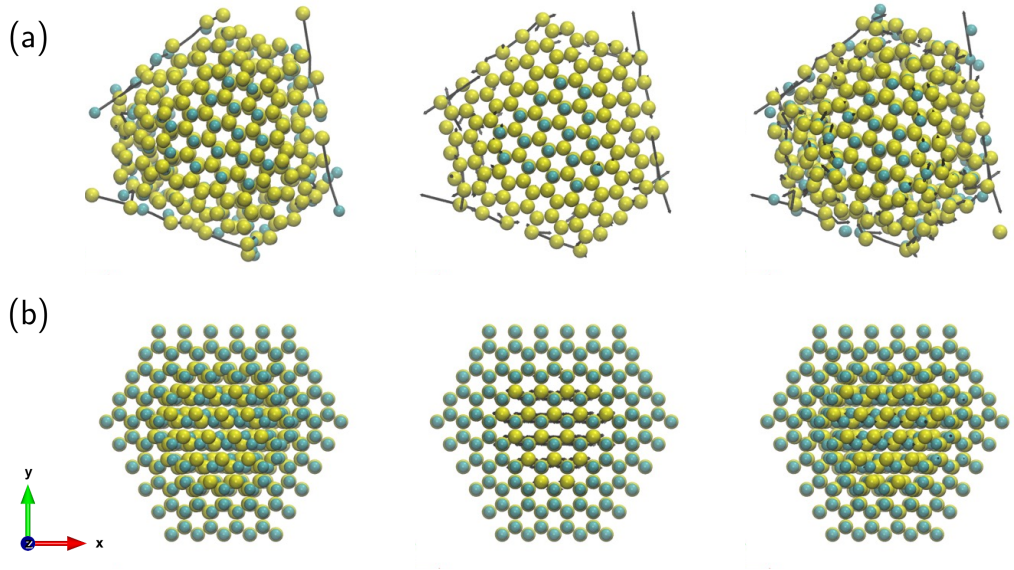

Figure 2.7: (a) Surface mode for a 3.9 nm CdSe nanocrystal (NC) with mode distance of 1.76 nm, a frequency of 4.18 meV (1.01 THz), and a reorganization energy of 0.0617 meV. (b) Interior mode for a 3.9 nm CdSe NC with mode distance of 0.850 nm, a frequency of 31.93 meV (7.72 THz), and a reorganization energy of 0.546 μeV.

Another question regarding EXPC in nanostructures is the effect of phonon confinement and whether phonon modes localized near the NC surface are inherently more strongly coupled to excitons than modes localized in the interior of the NC. To investigate these surface effects, we define the distance of phonon mode α from the center of the NC as

$$r_\alpha \equiv \sum_{\mu k} e^2_{\alpha,\mu k} r_\mu \,, \tag{2.49}$$

where r_μ is the distance of atom μ from the center of the NC. Note that phonon modes composed primarily of motion from surface atoms have a large value of r_α, and they can be delocalized over the NC. Fig. 2.7 shows two different phonon modes of a 3.9 nm CdSe NC;

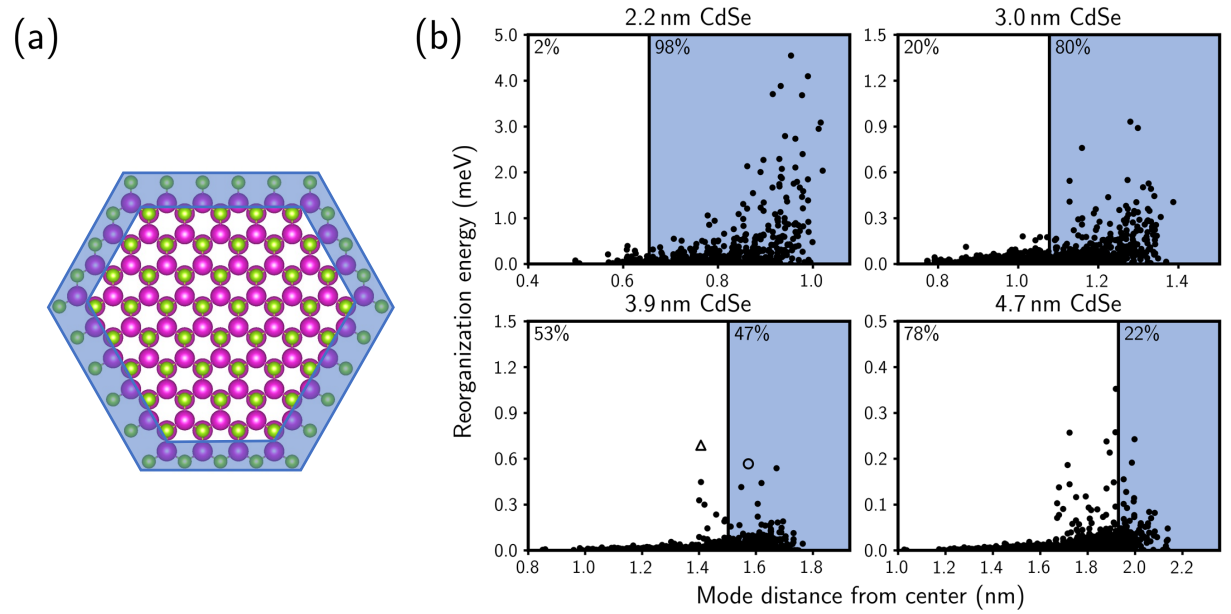

Figure 2.8: (a) Cross-section of a 3.9 nm CdSe NC with the outer ML shaded in blue. (b) Reorganization energy with phonon mode distance from the NC center for a series of CdSe NCs. Modes in the blue shaded regions are localized to the NC surface. The circle and triangle in the bottom left panel indicate the torsional and breathing modes illustrated in Fig. 2.6b,c, respectively. The numbers in the top left of each panel correspond to the percent contributions of the interior (white) and surface (blue) modes to the total reorganization energy.

the first corresponds to a mode with a large value of r_α, and the second corresponds to a mode with a small value of r_α.

Fig. 2.8a depicts a cross-section of a 3.9 nm CdSe NC with the outermost monolayer (ML) of atoms highlighted in blue. The reorganization energy of each mode as a function of the mode distance from the NC center is illustrated in Fig. 2.8b. For the smallest NC with a diameter of 2.2 nm, phonon modes localized to the outer ML have a total reorganization energy of 202 meV, which is 98% of the total reorganization energy. For this system, 92% of the modes are localized to the outer ML because of the relatively large surface area to volume ratio for an NC of such small size. The EXPC to these modes is relatively strong, as the exciton extends to the surface of the NC due to the large quantum confinement.

The contribution to the reorganization energy from surface modes decreases with increasing NC diameter. This trend is a result of the decreasing surface area to volume ratio as well as the decreasing quantum confinement in larger NCs, which leads to localization of the exciton wave function near the center of the NC and reduces the EXPC to surface modes. For a 4.7 nm CdSe NC, the interplay between surface and interior modes favors the interior

modes, which contribute 18 meV or 78% of the total reorganization energy. EXPC of interior modes with larger r_α values is greater than that of interior modes localized in the center of the NC. However, the total number of interior modes increases linearly with NC size and dominates contributions to the reorganization energy for large NCs.

The increased EXPC to surface modes in smaller NCs may explain photoluminescence measurements that observe broadened and red-shifted emission, which is attributed to emission from NC surface states, which increases with decreasing NC size [157, 166, 167]. Larger coupling of the exciton to surface modes in smaller NCs may facilitate phonon-mediated exciton trapping to surface states, thereby increasing photoluminescence from the surface.

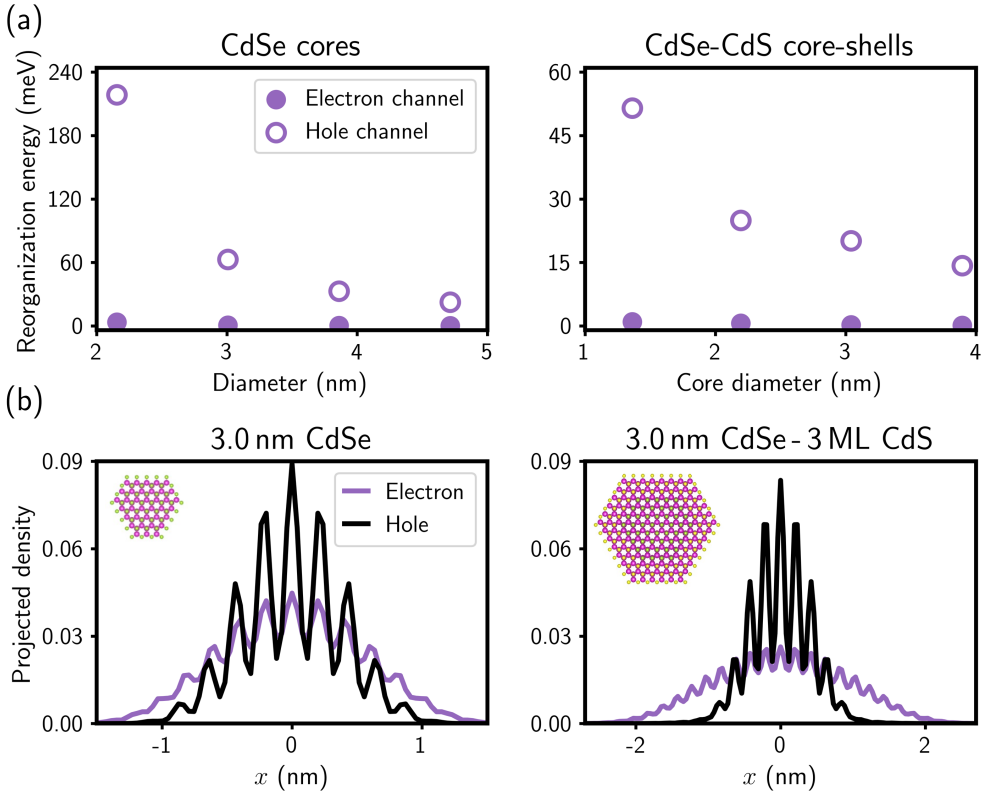

Figure 2.9: (a) Reorganization energies for CdSe (left) and CdSe/CdS core/shell (right) NCs of various sizes divided into contributions from the electron and hole channels. Reorganization energies for the core/shell NCs are an order of magnitude smaller than those of bare CdSe NCs. (b) Hole and electron carrier densities of the lowest-energy excitonic state for a 3.0 nm CdSe NC (left) and 3.0 nm CdSe/3 ML CdS NC (right).

The large contribution of surface modes to the reorganization energy of small NCs suggests that treatment of the NC surface, such as in core/shell NCs, could be used to control the magnitude of EXPC. As seen in Fig. 2.9a, the reorganization energy for CdSe cores with

3 MLs of CdS shell is about an order of magnitude smaller than for bare cores of the same size. These values, ranging from approximately 50 to 15 meV for CdSe core sizes ranging from 1.4 to 3.9 nm, agree with optical measurements of the Stokes shift [124].

This dramatic reduction is due to suppression of the hole channel of the EXPC (second term in the last line of Eq. (2.44)), which contributes more significantly to the reorganization energy (Fig. 2.9a). The quasi-type II band alignment of CdSe/CdS core/shell structures confines the exciton hole to the core, as illustrated in Fig. 2.9b. This hole confinement limits EXPC to modes that are delocalized over the NC. Because these low-frequency, delocalized modes generally have larger EXPC values than higher-frequency, localized modes, the overall reorganization energy is decreased in core-shell NCs.

For both core and core-shell systems, the hole channel of the EXPC is more significant than the electron channel because of the heavier hole effective mass, which makes the hole states more sensitive to the nuclear configuration, as well as the smaller energy spacing between hole states, which allows them to couple more readily *via* phonon absorption or emission.

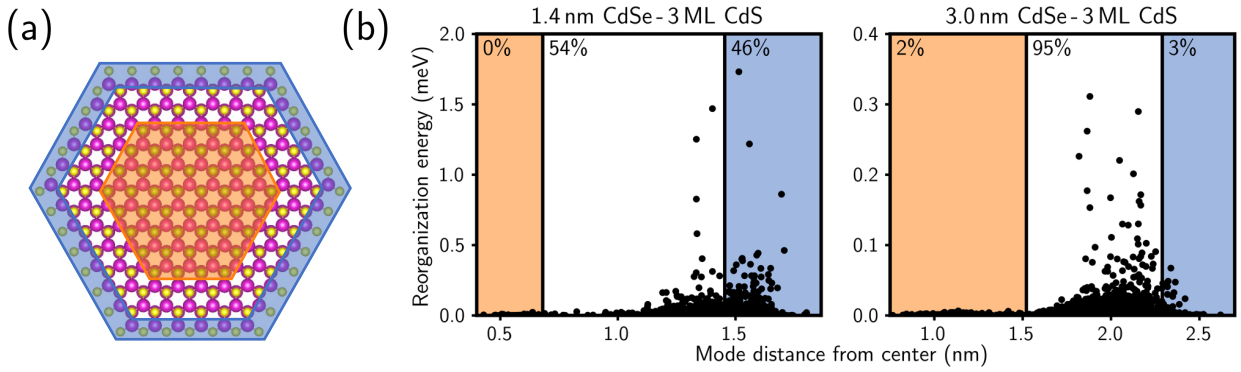

Figure 2.10: (a) Cross-section of a 3.0 nm CdSe/3 ML CdS NC with the core shaded in orange and the outer ML shaded in blue. (b) Reorganization energy with phonon mode distance from the NC center for two CdSe/CdS core/shell NCs. Modes in the orange and blue shaded regions are localized to the NC core and surface, respectively. The numbers in the top left of each panel correspond to the percent contributions of the core (orange), shell (white), and surface (blue) modes to the total reorganization energy.

An investigation of the reorganization energy with mode distance from the center for each core-shell NC (Fig. 2.10) shows that, despite the confinement of the hole to the core, modes localized to the core have a negligible contribution to the total reorganization energy. In the smallest core-shell system, a 1.4 nm CdSe/3 ML CdS NC, many modes are localized to the NC surface and comprise 46% of the reorganization energy. For larger core/shell systems, however, fewer modes are at the surface, and modes with r_α values that correspond to the NC shell make the most significant contributions to the reorganization energy. These

shell modes tend to be delocalized and consist of motion from both atoms near the surface and throughout the core. These results clearly indicate that, while the overall magnitude of EXPC is dictated by the relative localization of the carriers, EXPC is always strongest to those phonon modes that are delocalized across the NC and involve collective motion from many atoms in the system.

The approach outlined here provides a framework for computing EXPC in NCs that reproduces experimental results. Furthermore, our ability to calculate the EXPC to each phonon mode provides the first microscopic, atomistic approach of EXPC with frequency that reconciles discrepancies in previous observations regarding the relative magnitude of EXPC to acoustic versus optical phonons. We demonstrate that exciton formation distorts the NC lattice along phonon coordinates of low-frequency acoustic modes due to the inherently stronger coupling of excitons to these modes relative to that of excitons to optical modes. However, we also show that optical modes may be important in phonon-mediated exciton dynamics due to the large phonon density of states at those frequencies, which are at an energy scale that is more relevant for excitonic transitions. We also provide insight into the role of phonon confinement and the NC surface. Our results indicate that in small systems with diameters of less than 4 nm, where the number of surface modes is large and the exciton wavefunction is strongly quantum confined and extends to the NC surface, modes localized to the outer ML of the NC dominate contributions to the reorganization energy. However, the surface contribution decreases linearly with increasing system size. For all systems, even core/shell systems in which the exciton hole is confined to the core, EXPC is strongest to modes that are delocalized throughout the NC.

These calculations provide valuable insight into EXPC at the nanoscale. Furthermore, the framework presented here is general and can be applied to study anisotropic NCs, such as nanorods and nanoplatelets, to understand the role of dimensionality on EXPC, and to study III-V materials, such as InAs and InP, which have gained interest due to their nearinfrared emission. Finally, an accurate description of EXPC enables the understanding of timescales and mechanisms of phonon-mediated exciton dynamics, such as hot carrier cooling, exciton dephasing, and charge transport, which are essential in promoting the rational design of NCs with quantum yields necessary for the realization of new technologies.

2.3.1 Derivation of electron-nuclear coupling matrix elements

Consider the full, vibronic Schrodinger equation

$$H(\boldsymbol{r},\boldsymbol{R})|\Psi(\boldsymbol{r},\boldsymbol{R})\rangle = \varepsilon|\Psi(\boldsymbol{r},\boldsymbol{R})\rangle\,, \tag{2.50}$$

where $\boldsymbol{r}$ and $\boldsymbol{R}$ describe the electronic and nuclear coordinates, respectively, and the full Hamiltonian is given by

$$H(\boldsymbol{r},\boldsymbol{R}) = T\left(\boldsymbol{r}\right) + T\left(\boldsymbol{R}\right) + V\left(\boldsymbol{R}\right) + U\left(\boldsymbol{r},\boldsymbol{R}\right)\,. \tag{2.51}$$

In the above, $T(\boldsymbol{r})$ is the kinetic energy of the electrons, $T(\boldsymbol{R})$ is the kinetic energy of the nuclei, $V(\boldsymbol{R})$ is the nuclear potential, and $U(\boldsymbol{r},\boldsymbol{R})$ is the electron-nuclear potential.

In the Born-Huang approximation, the electronic Hamiltonian is given by

$$H_{\mathrm{el}}(\boldsymbol{r};\boldsymbol{R}) = T(\boldsymbol{r}) + U(\boldsymbol{r};\boldsymbol{R}) \tag{2.52}$$

with solutions

$$H_{\mathrm{el}}(\boldsymbol{r};\boldsymbol{R})|\phi_n(\boldsymbol{r};\boldsymbol{R})\rangle = E_n(\boldsymbol{R})|\phi_n(\boldsymbol{r};\boldsymbol{R})\rangle\,, \tag{2.53}$$

where the electronic states, $|\phi_n\rangle$, and energies, E_n, depend parametrically on the nuclear configuration.

The full vibronic wavefunction can be written as an expansion in terms of these electronic wavefunctions, which form a complete basis:

$$|\Psi(\boldsymbol{r},\boldsymbol{R})\rangle = \sum_{ni} \chi_{ni}(\boldsymbol{R})|\phi_n(\boldsymbol{r};\boldsymbol{R})\rangle\,, \tag{2.54}$$

where $\chi_{ni}(\boldsymbol{R})$ is the vibrational part of the wavefunction.

Alternatively, the full vibronic wavefunction can be written in terms of a different complete basis:

$$\Psi(\boldsymbol{r},\boldsymbol{R}) = \sum_{ni} \chi_{ni}(\boldsymbol{R})|\phi_n(\boldsymbol{r};\boldsymbol{R}_0)\rangle\,, \tag{2.55}$$

where $|\phi_n(\boldsymbol{r};\boldsymbol{R}_0)\rangle$ are solutions to the "static equation," which is given by

$$H_{\mathrm{el}}(\boldsymbol{r};\boldsymbol{R}_0)|\phi_n(\boldsymbol{r};\boldsymbol{R}_0)\rangle = E_n(\boldsymbol{R}_0)|\phi_n(\boldsymbol{r};\boldsymbol{R}_0)\rangle\,. \tag{2.56}$$

For clarity, we will now write $|\phi_n\rangle \equiv |\phi_n(\boldsymbol{r};\boldsymbol{R}_0)\rangle$.

The difference between the electronic Hamiltonian in the Born-Huang approximation and the static equation is defined as $\Delta U(\boldsymbol{r},\boldsymbol{R})$:

$$\Delta U(\boldsymbol{r},\boldsymbol{R}) \equiv H_{\mathrm{el}}(\boldsymbol{r},\boldsymbol{R}) - H_{\mathrm{el}}(\boldsymbol{r};\boldsymbol{R}_0) \tag{2.57}$$

$$= U(\boldsymbol{r},\boldsymbol{R}) - U(\boldsymbol{r};\boldsymbol{R}_0)\,. \tag{2.58}$$

Substituting Eq. (2.55) into the full Schrodinger Equation (Eq. (2.50)) and left-multiplying the equation by $\langle\phi_m|$, we have:

$$[T(\boldsymbol{R}) + V(\boldsymbol{R}) + E_n(\boldsymbol{R}_0) + \langle\phi_n|\Delta U(\boldsymbol{r},\boldsymbol{R})|\phi_n\rangle - \varepsilon]\chi_{ni}(\boldsymbol{R}) + \sum_{m\neq n}\langle\phi_n|\Delta U(\boldsymbol{r},\boldsymbol{R})|\phi_m\rangle\chi_{mi}(\boldsymbol{R}) = 0\,. \tag{2.59}$$

In the crude adiabatic approximation, we assume that for $n \neq m$, $\langle\phi_n|\Delta U(\boldsymbol{r},\boldsymbol{R})|\phi_m\rangle = 0$. Thus, the vibrational Schrodinger Equation within the crude adiabatic approximation [168] is

$$\left[T\left(\boldsymbol{R}\right) + V\left(\boldsymbol{R}\right) + E_n\left(\boldsymbol{R}_0\right) + \left\langle\phi_n\left|\Delta U\left(\boldsymbol{r},\boldsymbol{R}\right)\right|\phi_n\right\rangle\right]\chi_{ni}\left(\boldsymbol{R}\right) = \varepsilon\chi_{ni}\left(\boldsymbol{R}\right)\,. \tag{2.60}$$

We use an atomic force field (such as a previously-parameterized Stillinger-Weber potential [103], U_{SW}), which approximates the ground Born-Oppenheimer potential energy surface:

$$U_{\mathrm{SW}} \approx V\left(\boldsymbol{R}\right) + E_0\left(\boldsymbol{R}\right) . \tag{2.61}$$

We can relate the crude adiabatic and Born-Oppenheimer potential energy surfaces by expanding $E_0\left(\boldsymbol{R}\right)$ in terms of $E_0\left(\boldsymbol{R}_0\right)$ using perturbation theory:

$$\begin{aligned} E_0\left(\boldsymbol{R}\right) =& E_0\left(\boldsymbol{R}_0\right) + \left\langle \phi_0 \left| \Delta U\left(\boldsymbol{r},\boldsymbol{R}\right) \right| \phi_0 \right\rangle \\ &+ \sum_{m\neq 0} \frac{\left\langle \phi_0 \left| \Delta U\left(\boldsymbol{r},\boldsymbol{R}\right) \right| \phi_m \right\rangle \left\langle \phi_m \left| \Delta U\left(\boldsymbol{r},\boldsymbol{R}\right) \right| \phi_0 \right\rangle}{E_0(\boldsymbol{R}_0) - E_m(\boldsymbol{R}_0)} + \dots . \end{aligned} \tag{2.62}$$

If we neglect terms that are second order and higher, we see that

$$E_0\left(\boldsymbol{R}\right) \approx E_0\left(\boldsymbol{R}_0\right) + \left\langle \phi_0 \left| \Delta U\left(\boldsymbol{r},\boldsymbol{R}\right) \right| \phi_0 \right\rangle , \tag{2.63}$$

so that the Stillinger-Weber potential can also be used to model the crude adiabatic ground potential energy surface. For crude adiabatic excited potential energy surfaces, we have

$$\begin{aligned} V\left(\boldsymbol{R}\right) + E_n\left(\boldsymbol{R}_0\right) + \left\langle \phi_n \left| \Delta U\left(\boldsymbol{r},\boldsymbol{R}\right) \right| \phi_n \right\rangle & \\ =& V\left(\boldsymbol{R}\right) + E_n\left(\boldsymbol{R}_0\right) + \left\langle \phi_n \left| \Delta U\left(\boldsymbol{r},\boldsymbol{R}\right) \right| \phi_n \right\rangle \\ &+ E_0\left(\boldsymbol{R}_0\right) + \left\langle \phi_0 \left| \Delta U\left(\boldsymbol{r},\boldsymbol{R}\right) \right| \phi_0 \right\rangle \\ &- E_0\left(\boldsymbol{R}_0\right) - \left\langle \phi_0 \left| \Delta U\left(\boldsymbol{r},\boldsymbol{R}\right) \right| \phi_0 \right\rangle \qquad (2.64) \\ =& V\left(\boldsymbol{R}\right) + E_0\left(\boldsymbol{R}_0\right) + \left\langle \phi_0 \left| \Delta U\left(\boldsymbol{r},\boldsymbol{R}\right) \right| \phi_0 \right\rangle \\ &+ E_n\left(\boldsymbol{R}_0\right) - E_0\left(\boldsymbol{R}_0\right) \\ &+ \left\langle \phi_n \left| \Delta U\left(\boldsymbol{r},\boldsymbol{R}\right) \right| \phi_n \right\rangle - \left\langle \phi_0 \left| \Delta U\left(\boldsymbol{r},\boldsymbol{R}\right) \right| \phi_0 \right\rangle . \qquad (2.65) \end{aligned}$$

In systems, such as semiconductors, where nuclear displacements away from the equilibrium configuration are relatively small, the electron-nuclear potential can be expanded around the equilibrium configuration and truncated at first order:

$$U(\boldsymbol{r},\boldsymbol{R}) \approx U(\boldsymbol{r},\boldsymbol{R_0}) + \left(\frac{\partial U(\boldsymbol{r},\boldsymbol{R})}{\partial \boldsymbol{R}}\right)_{\boldsymbol{R}_0} (\boldsymbol{R}-\boldsymbol{R}_0) \tag{2.66}$$

$$\Delta U(\boldsymbol{r},\boldsymbol{R}) \approx \left(\frac{\partial U(\boldsymbol{r},\boldsymbol{R})}{\partial \boldsymbol{R}}\right)_{\boldsymbol{R}_0} (\boldsymbol{R}-\boldsymbol{R}_0) \tag{2.67}$$

so that

$$\begin{aligned} V\left(\boldsymbol{R}\right) + E_n\left(\boldsymbol{R}_0\right) + \left\langle \phi_n \left| \Delta U\left(\boldsymbol{r},\boldsymbol{R}\right) \right| \phi_n \right\rangle & \\ =& V\left(\boldsymbol{R}\right) + E_0\left(\boldsymbol{R}_0\right) + \left\langle \phi_0 \left| \Delta U\left(\boldsymbol{r},\boldsymbol{R}\right) \right| \phi_0 \right\rangle \\ &+ \left(E_n(\boldsymbol{R}_0) - E_0(\boldsymbol{R}_0)\right) \\ &+ \left[\left\langle \phi_n \left| \left(\frac{\partial U\left(\boldsymbol{r},\boldsymbol{R}\right)}{\partial \boldsymbol{R}} \right)_{\boldsymbol{R}_0} \right| \phi_n \right\rangle - \left\langle \phi_0 \left| \left(\frac{\partial U\left(\boldsymbol{r},\boldsymbol{R}\right)}{\partial \boldsymbol{R}} \right)_{\boldsymbol{R}_0} \right| \phi_0 \right\rangle \right] (\boldsymbol{R}-\boldsymbol{R}_0) . \end{aligned} \tag{2.68}$$

We see that all of the potential energy surfaces are parallel with vertical shifts given by

$$\left(E_n(\boldsymbol{R}_0) - E_0(\boldsymbol{R}_0)\right) \tag{2.69}$$

and horizontal shifts given by

$$\left[\left\langle \phi_n \left| \left(\frac{\partial U\left(\boldsymbol{r},\boldsymbol{R}\right)}{\partial \boldsymbol{R}}\right)_{\boldsymbol{R}_0} \right| \phi_n \right\rangle - \left\langle \phi_0 \left| \left(\frac{\partial U\left(\boldsymbol{r},\boldsymbol{R}\right)}{\partial \boldsymbol{R}}\right)_{\boldsymbol{R}_0} \right| \phi_0 \right\rangle\right] . \tag{2.70}$$

Therefore, all crude adiabatic potential energy surfaces share the same vibrational frequencies and modes, which can be calculated using the same atomic force field.

Similarly, the coupling between the electronic states, or corrections to the crude adiabatic approximation, can be expanded around the equilibrium configuration and truncated at first order in the atomic displacements:

$$\left\langle \phi_n \left| \Delta U\left(\boldsymbol{r},\boldsymbol{R}\right) \right| \phi_m \right\rangle \approx \left\langle \phi_n \left| \left(\frac{\partial U\left(\boldsymbol{r},\boldsymbol{R}\right)}{\partial \boldsymbol{R}}\right)_{\boldsymbol{R}_0} \right| \phi_m \right\rangle \left(\boldsymbol{R}-\boldsymbol{R}_0\right) . \tag{2.71}$$

As described in Sec. 2.1, we take the electronic Hamiltonian, which includes $T\left(\boldsymbol{r}\right) + U\left(\boldsymbol{r},\boldsymbol{R}\right)$, as the single-particle Hamiltonian within the semiempirical pseudopotential method at the equilibrium nuclear configuration, $\boldsymbol{R}_0$:

$$\hat{h}_{\mathrm{qp}} = -\frac{1}{2}\nabla_{\boldsymbol{r}}^2 + \sum_{\mu} \hat{v}_{\mu}\left(\boldsymbol{r};\boldsymbol{R}_0\right) , \tag{2.72}$$

where $\hat{v}_{\mu}\left(\boldsymbol{r};\boldsymbol{R}_0\right)$ is the effective pseudopotential for atom μ. We then use the filter diagonalization technique to solve for quasiparticle states $\left|\phi_n\left(\boldsymbol{r};\boldsymbol{R}_0\right)\right\rangle$ near the band edge.

Within our semiempirical pseudopotential electronic structure model, the single-particle electron-nuclear coupling matrix elements to first order in the atomic displacements are given by

$$v'_{rs,\mu} = \int d\boldsymbol{r} \phi_r^*\left(\boldsymbol{r};\boldsymbol{R}_0\right) \left(\frac{\partial \hat{v}\left(\boldsymbol{r},\boldsymbol{R}\right)}{\partial R_{\mu k}}\right)_{\boldsymbol{R}_0} \phi_s\left(\boldsymbol{r};\boldsymbol{R}_0\right) , \tag{2.73}$$

where $R_{\mu k}$ is the coordinate of atom μ in the $k \in \{x,y,z\}$ direction and $\hat{v}\left(\boldsymbol{r},\boldsymbol{R}\right)$ is the total pseudopotential given by a sum over atomic pseudopotentials:

$$\hat{v}\left(\boldsymbol{r},\boldsymbol{R}\right) = \sum_{\mu} \left[1 + a_4^{\mu}\left(\frac{\Omega_{\mu}\left(\left\{\boldsymbol{R}_{\nu\in N_{\mu}}\right\}\right)}{\Omega_{\mu,0}} - 1\right) + a_5^{\mu}\left(\frac{\Omega_{\mu}\left(\left\{\boldsymbol{R}_{\nu\in N_{\mu}}\right\}\right)}{\Omega_{\mu,0}} - 1\right)^3\right] v_{\mu}\left(\left|\boldsymbol{r}-\boldsymbol{R}_{\mu}\right|\right) , \tag{2.74}$$

where Ω_{μ} is the volume of the tetrahedron formed by the nearest neighbors of atom μ, and $\Omega_{\mu,0}$ is the reference volume of that tetrahedron in an unstrained crystal. The index $\nu \in N_{\mu}$ runs over the nearest neighbors of atom μ. In the above, $v_{\mu}\left(\left|\boldsymbol{r}-\boldsymbol{R}_{\mu}\right|\right)$ is the part of the atomic pseudopotential that just depends on the position of atom μ, $\boldsymbol{R}_{\mu}$.

The derivative of this pseudopotential with respect to $R_{\mu k}$ is given by:

$$\frac{\partial \hat{v}\left(\boldsymbol{r},\boldsymbol{R}\right)}{\partial R_{\mu k}} = \left[1 + a_4^\mu \left(\frac{\Omega_\mu\left(\left\{\boldsymbol{R}_{\nu\in N_\mu}\right\}\right)}{\Omega_{\mu,0}} - 1\right) + a_5^\mu \left(\frac{\Omega_\mu\left(\left\{\boldsymbol{R}_{\nu\in N_\mu}\right\}\right)}{\Omega_{\mu,0}} - 1\right)^3\right] \frac{\partial v_\mu\left(|\boldsymbol{r}-\boldsymbol{R}_\mu|\right)}{\partial R_{\mu k}} + \sum_{\nu\in N_\mu} \Omega_{\mu,0}^{-1} \frac{\partial \Omega_\nu\left(\{\boldsymbol{R}_{\kappa\in N_\nu}\}\right)}{\partial R_{\mu k}} \left[a_4^\nu + 3a_5^\nu \left(\frac{\Omega_\mu\left(\left\{\boldsymbol{R}_{\nu\in N_\mu}\right\}\right)}{\Omega_{\mu,0}} - 1\right)^2\right] v_\nu\left(|\boldsymbol{r}-\boldsymbol{R}_\nu|\right) . \tag{2.75}$$

As described in Sec. 2.3, the quasiparticle matrix elements given by Eq. (2.73) can be multiplied by coefficients obtained by solving the Bethe-Salpeter to obtain the exciton-nuclear coupling matrix elements. These can be transformed to phonon mode coordinates to obtain the final exciton-phonon couplings.

Chapter 3

Circumventing the phonon bottleneck by multiphonon-mediated hot exciton cooling at the nanoscale

Understanding the mechanisms of nonradiative decay of electronic excited states in semiconductor nanocrystals (NCs) is key to developing NC-based applications with decreased thermal losses and increased device efficiencies. In this chapter, we use the framework introduced in Ch. 2 and develop a theory for phonon-mediated exciton dynamics. We simulate hot exciton cooling in NCs to address the longstanding controversy of the phonon bottleneck [59], which hypothesized slow cooling in quantum confined structures. Contrary to the phonon bottleneck, we find that cooling in CdSe NCs occurs in tens of femtoseconds (fs), in agreement with recent two-dimensional electronic spectroscopy experiments, *via* a cascade of relaxation events due to efficient multiphonon emission processes. The cooling timescale increases with increasing NC size due to decreased exciton-phonon coupling (EXPC) in larger systems. Similarly, cooling in CdSe/CdS core/shell NCs is an order of magnitude slower than in bare CdSe cores. These simulations provide the first unified, microscopic theory for hot exciton cooling in nanoscale systems that accurately describes electron-hole correlations, EXPCs, and multiphonon-mediated exciton dynamics. Our findings reconcile previous experimental discrepancies and provide design principles for NCs with tuned EXPC and cooling timescales.

3.1 Introduction

Hot exciton cooling is the process by which excited carriers nonradiatively relax to the band edge in semiconductor materials [5, 169]. In bulk semiconductors, Fröhlich interactions between excitons and phonons as well as continuous densities of electronic and phonon states allow for efficient cooling that occurs on timescales of $\sim$1 ps or less [170–172]. However, in semiconductor NCs, confinement changes the nature of EXPC and leads to the discretization

of both electronic and phonon states. The electronic energy gaps, especially near the conduction band edge, can be hundreds of meV (Fig. 2.2b) whereas phonon frequencies are 30 meV or less (Fig. 2.4a). This energy mismatch has led to the hypothesis of a phonon bottleneck in NCs [59], where cooling *via* phonon emission would require multiphonon processes that would be inefficient [173], leading to very slow relaxation.

Experimental measurements of this cooling process in NCs rely on time-resolved spectroscopy, such as transient absorption, and have yielded conflicting results. Some experiments show slow relaxation that occurs on timescales of 10 ps or longer [33, 37, 51–55], which support the phonon bottleneck hypothesis. These measurements were primarily performed on larger, self-assembled III-V NCs [174], which are in the weak confinement regime and which tend to have many localized trap states associated with defects. Other experiments, especially on colloidal II-VI NCs in the strong confinement regime, have observed relaxation that occurs within hundreds of fs with carrier energy loss rates that are much faster than those of bulk carriers [56–58, 63, 64, 175, 176].

This fast relaxation was explained by an Auger-assisted cooling mechanism that circumvents the phonon bottleneck [177, 178]. In this mechanism, illustrated schematically in Fig. 3.1b, the hot hole quickly relaxes to the band edge *via* phonon emission, which is possible due to the higher density of hole states. Then, the hot electron relaxes to the band edge by nonradiatively re-exciting the hole in an Auger-like process, and finally the hole relaxes again. The Auger cooling mechanism has been supported by observations that relaxation is faster in smaller NCs [56, 62, 64, 175, 176], in which Coulomb-mediated electron-hole correlations are larger and Auger rates are faster [81]. Additionally, relaxation timescales increase drastically in NCs that are passivated with hole-accepting pyridine ligands [33, 35, 57], indicating that electron-hole correlations are important in the cooling mechanism. Other studies suggest that fast relaxation is due to efficient multiphonon emission [176] or due to coupling of electrons and/or holes to vibrational modes of surface passivating ligands [35, 63].

These conflicting measurements as well as the computational challenges [61, 65, 154] associated with accurately calculating excitons and their phonon-mediated dynamics in systems with thousands of valence electrons have led to outstanding questions about the timescales and mechanisms of hot exciton cooling in confined semiconductor NCs [5, 169]. However, a fundamental understanding of the cooling process is essential to developing NC systems with decreased thermal losses and increased quantum yields.

In this chapter, we develop an atomistic theory to describe hot exciton cooling in NCs of experimentally relevant sizes. Our framework for phonon-mediated exciton dynamics accounts for electron-hole correlations [81], accurate descriptions of EXPCs [82], and multiphonon processes. With this unified approach, the timescales and mechanisms of hot exciton cooling emerge naturally from our simulations. We find that cooling occurs within tens of fs in CdSe NCs, in agreement with two-dimensional electronic spectroscopy measurements [85], and occurs an order of magnitude more slowly in CdSe/CdS core/shell NCs due to the weaker EXPC in these systems. We show that this ultrafast timescale is governed by *both* electron-hole correlations *and* multiphonon emission processes, which are made efficient by

the large number and frequency range of phonon modes in NC systems.

3.2 Describing phonon-mediated exciton relaxation

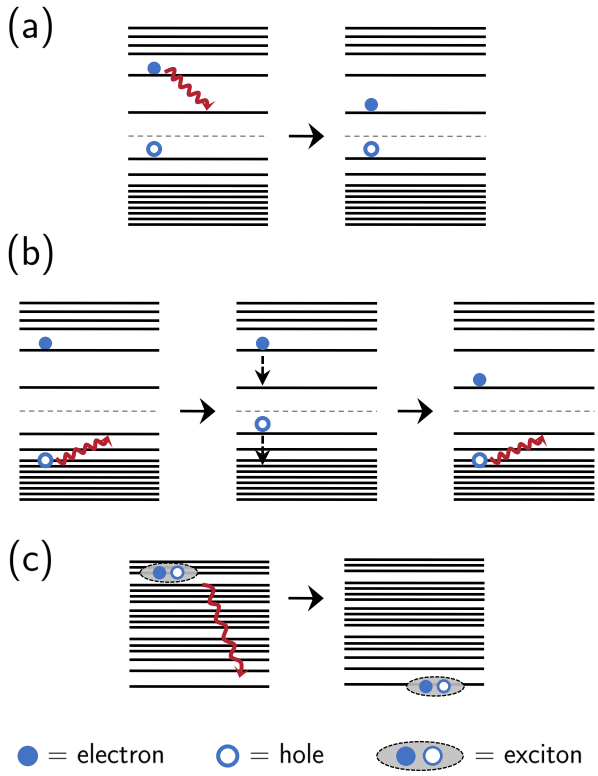

Figure 3.1: (a) The phonon bottleneck refers to phonon-mediated relaxation between single-particle electron states near the band edge, which would require the emission of tens of phonons due to the large energy gap between these electronic states. (b) The Auger-assisted cooling mechanism involves Coulomb-mediated interactions between single-particle electron and hole states. The hole first relaxes to the band edge *via* phonon emission. Then, the electron relaxes to the band edge by re-exciting the hole, which then again relaxes to the band edge. (c) Our formalism includes both electron-hole correlations and exciton-phonon interactions, circumventing the phonon bottleneck through a cascade of phonon-mediated transitions between excitonic states with smaller energy gaps.

The phonon bottleneck hypothesis is based on a single-particle picture of electronic states for which the energy spacing between states near the band edge becomes several hundreds of meV. In this case, because the phonon frequencies in these systems are ∼30 meV and lower, a process involving tens of phonons would be required for phonon-mediated relaxation, which

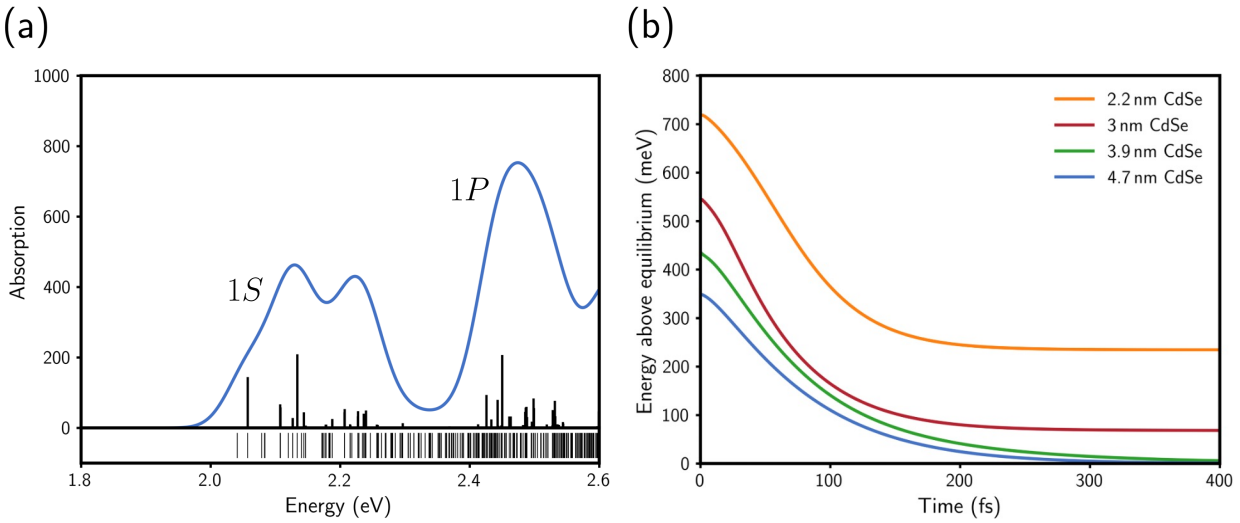

Figure 3.2: (a) The calculated linear absorption spectrum (top) and density of excitonic states (bottom) for a wurtzite 3.9 nm CdSe NC. The vertical lines in the top panel indicate the magnitude of the oscillator strength of the transition from the ground state to that excitonic state. Cooling from the $1P$ to the $1S$ excitonic states, whose transitions are labeled in the absorption spectrum, is the main subject of this work. (b) Single-phonon-mediated cooling simulated for wurtzite CdSe NCs of different sizes shows slow relaxation in smaller NCs because the excitonic energy gaps in those systems are larger than the highest phonon frequencies.

would be extremely slow (Fig. 3.1a). The Auger-like processes that have been invoked to explain the breaking of the phonon bottleneck require Coulomb-mediated interactions between single-particle electron and hole states (Fig. 3.1b). This picture is translated in our approach to a two-particle picture of *excitonic* states, where the phonon bottleneck is circumvented by a cascade of phonon-mediated transitions between excitonic states, which have smaller energy spacings and which inherently include electron-hole correlations (Fig. 3.1c). We calculate the linear absorption spectrum for a 3.9 nm CdSe NC and find that, while the spectrum features three main peaks, as illustrated in Fig. 3.2a, the underlying density of excitonic states is relatively high due to the dense spectrum of hole states. Some of these excitonic states correspond to bright transitions from the ground state with large oscillator strengths while others correspond to dim transitions for which the oscillator strengths are small. Thus, relaxation from the $1P$ excitonic state, in which the exciton electron is primarily composed of p-like quasi-electron states, to the $1S$ ground excitonic state, in which both the exciton electron and hole are primarily comprised of band edge single-particle states, occurs through a cascade of phonon-mediated excitonic transitions. While the largest energy gaps between these excitonic states are an order of magnitude smaller than those between

quasi-electron states, they can still be larger than the phonon frequencies. Thus, cooling solely *via* single-phonon transitions prevents full relaxation to the ground excitonic state (Fig. 3.2b), especially in smaller NCs for which confinement results in larger excitonic energy gaps, and multiphonon processes involving a few phonon modes are still essential to the cooling mechanism.

We use the Hamiltonian introduced in Ch. 2 to describe a manifold of excitonic states coupled to a bath of phonons to first order in atomic displacements:

$$H = \sum_n E_n \left|\psi_n\right\rangle \left\langle\psi_n\right| + \sum_\alpha \hbar\omega_\alpha b_\alpha^\dagger b_\alpha + \sum_{\alpha nm} V_{n,m}^\alpha \left|\psi_n\right\rangle \left\langle\psi_m\right| q_\alpha \,. \tag{3.1}$$

As detailed in Ch. 2, the excitonic energies, E_n, and states, $|\psi_n\rangle$, were calculated within the semiempirical pseudopotential method. We used the filter diagonalization method to solve for single-particle electron and hole states near the band edges [10, 26, 27] and then used these as input to the Bethe-Salpeter equation, which was solved to obtain correlated electron-hole states [81]. Phonon modes and frequencies, ω_α, were obtained by diagonalizing the dynamical matrix computed using an atomic force field [103].

Given this Hamiltonian, phonon-mediated transition rates between excitonic states n and m can be computed using Fermi's golden rule, which assumes weak system-bath coupling and employs the Markovian approximation:

$$\Gamma_{n\to m} = \frac{1}{\hbar^2}\int_{-\infty}^{\infty} dt e^{i(E_n - E_m)t/\hbar} \sum_\alpha V_{n,m}^\alpha V_{m,n}^\alpha \langle q_\alpha(t) q_\alpha(0)\rangle_{\text{eq}} \,, \tag{3.2}$$

where $\langle \dots \rangle_{\text{eq}}$ denotes an equilibrium average over bath coordinates. Because Eq. (3.1) describes the EXPC to first order in phonon mode coordinates, the Fermi's golden rule rates given by Eq. (3.2) only describe excitonic transitions that occur *via* the absorption or emission of a single phonon.

To account for multiphonon processes, we performed a unitary polaron transformation [83, 84, 179, 180] to the Hamiltonian in Eq. (3.1):

$$\tilde{H} = e^S H e^{-S} \tag{3.3}$$

$$= \exp\left[-\frac{i}{\hbar}\sum_{\alpha k} \omega_\alpha^{-2} p_\alpha V_{k,k}^\alpha |\psi_k\rangle\langle\psi_k| \right] H \exp\left[\frac{i}{\hbar}\sum_{\alpha k} \omega_\alpha^{-2} p_\alpha V_{k,k}^\alpha |\psi_k\rangle\langle\psi_k| \right] \tag{3.4}$$

$$= \sum_n \big(E_n - \lambda_n\big)|\psi_n\rangle\langle\psi_n| + \sum_\alpha \hbar\omega_\alpha b_\alpha^\dagger b_\alpha + \sum_{n\neq m} \Big(\sum_\alpha \tilde{V}_{n,m}^\alpha q_\alpha - \tilde{\lambda}_{nm}\Big)|\psi_n\rangle\langle\psi_m| \,, \tag{3.5}$$

where

$$\lambda_n \equiv \frac{1}{2}\sum_\alpha \omega_\alpha^{-2}\left(V_{n,n}^\alpha\right)^2 \tag{3.6}$$

$$\tilde{\lambda}_{nm} \equiv \frac{1}{2}\sum_\alpha \omega_\alpha^{-2}\tilde{V}_{n,m}^\alpha\left(V_{n,n}^\alpha + V_{m,m}^\alpha\right) \tag{3.7}$$

$$\tilde{V}_{n,m}^\alpha \equiv \exp\left[-\frac{i}{\hbar}\sum_\alpha \omega_\alpha^{-2}p_\alpha V_{n,n}^\alpha\right] V_{n,m}^\alpha \exp\left[\frac{i}{\hbar}\sum_\alpha \omega_\alpha^{-2}p_\alpha V_{m,m}^\alpha\right]. \tag{3.8}$$

In the above equations, p_α is the momentum of phonon mode α, and λ_n is the reorganization energy of exciton n, which was introduced in Ch. 2.3. A detailed derivation and description of the polaron-transformed Hamiltonian is given in Sec. 3.2.1.

With respect to the polaron-transformed Hamiltonian, Fermi's golden rule transition rates can be computed as

$$\Gamma_{n\to m} = \frac{1}{\hbar^2}\int_{-\infty}^{\infty} dt e^{i(\varepsilon_n-\varepsilon_m)t/\hbar}\langle g_{n,m}(t)g_{m,n}(0)\rangle_{\text{eq}}\,, \tag{3.9}$$

where $\varepsilon_n \equiv E_n - \lambda_n$ is the energy of exciton n scaled by its reorganization energy, and $g_{n,m} \equiv \sum_\alpha \tilde{V}_{n,m}^\alpha q_\alpha - \tilde{\lambda}_{nm}$ is the coupling between the polaronic states n and m. Note that $g_{n,m}$ includes exponential functions of the phonon momenta, so multiphonon-mediated transitions are accounted for even in the lowest-order perturbation theory rate given by Eq. (3.9). This point is further illustrated in Sec. 3.2.1.

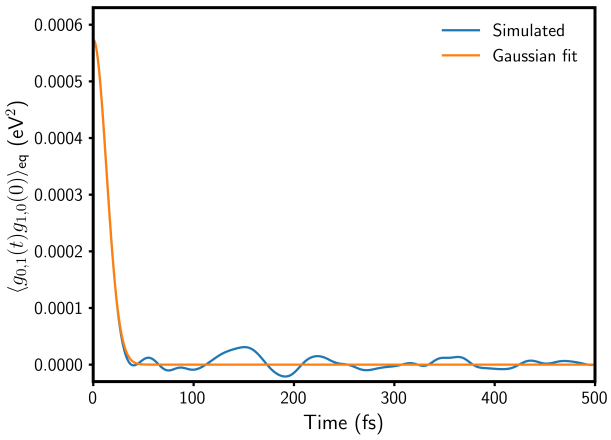

Figure 3.3: The correlation functions $\langle g_{n,m}(t)g_{m,n}(0)\rangle$ quickly decay to zero, followed by long-lived noise. Thus, the correlation functions are calculated to short times and then approximated by Gaussian functions.

The correlation functions in Eq. (3.9) were evaluated within a harmonic approximation by sampling from a thermal distribution of bath coordinates and propagating classical trajectories. As illustrated in Fig. 3.3, the correlation functions are overdamped, featuring a decay to zero followed by long-lived noise due to statistical fluctuations. Therefore, we facilitate convergence by propagating and averaging trajectories to short times and then approximating the correlation functions as Gaussian functions. However, the timescales on which the correlation functions decay are not necessarily faster than those of the system dynamics, so we calculated non-Markovian relaxation rates. We also applied the standard quantum correction scheme [181], which assumes that the real part of the quantum correlation function is equal to the classical correlation function computed here. Thus, the final transition rates are given by

$$\Gamma_{n\to m}(t) = \left[\frac{2}{1+e^{-\beta\hbar(\varepsilon_n-\varepsilon_m)}}\right]\frac{1}{\hbar^2}\int_0^t d\tau \cos\left((\varepsilon_n-\varepsilon_m)\tau/\hbar\right)\langle g_{n,m}(\tau)g_{m,n}(0)\rangle_{\mathrm{eq}}\,. \tag{3.10}$$

We computed rates for all excitonic transitions and used them to build a kinetic master equation and propagate phonon-mediated exciton dynamics.

3.2.1 Derivation and analysis of polaron-transformed Hamiltonian

The standard Hamiltonian that describes a manifold of excitonic states and phonons that are coupled to first order in the atomic displacements is given by [87]:

$$\boldsymbol{H} = \boldsymbol{H}_S + H_B + \boldsymbol{V}_{SB} \tag{3.11}$$

$$= \sum_n E_n \left|\psi_n\right\rangle\left\langle\psi_n\right| + \sum_\alpha \hbar\omega_\alpha b_\alpha^\dagger b_\alpha + \sum_{\alpha nm}\sqrt{\frac{\hbar}{2\omega_\alpha}}V_{n,m}^\alpha \left|\psi_n\right\rangle\left\langle\psi_m\right|\left(b_\alpha^\dagger + b_\alpha\right) \tag{3.12}$$

$$= \sum_n E_n \left|\psi_n\right\rangle\left\langle\psi_n\right| + \frac{1}{2}\sum_\alpha\left[p_\alpha^2+\omega_\alpha^2 q_\alpha^2\right] + \sum_{\alpha nm} V_{n,m}^\alpha \left|\psi_n\right\rangle\left\langle\psi_m\right| q_\alpha\,. \tag{3.13}$$

Note that operators in the system subspace are bolded, and Eq. (3.13) makes use of the relationships between the Bosonic creation and annihilation operators and the position and momentum operators.

We will now perform a unitary polaron transformation [83, 179]:

$$\tilde{\boldsymbol{H}} = e^{\boldsymbol{S}}\boldsymbol{H}e^{-\boldsymbol{S}}\,, \tag{3.14}$$

$$= \exp\left(-\frac{i}{\hbar}\sum_\alpha \omega_\alpha^{-2}p_\alpha \boldsymbol{V}_D^\alpha\right)\boldsymbol{H}\exp\left(+\frac{i}{\hbar}\sum_\alpha \omega_\alpha^{-2}p_\alpha \boldsymbol{V}_D^\alpha\right)\,, \tag{3.15}$$

where we have defined the diagonal of a system-subspace operator, $\boldsymbol{A}$, as $\boldsymbol{A}_D$, so that

$$\boldsymbol{V}_D^\alpha \equiv \sum_{kl} V_{k,l}^\alpha \delta_{k,l}\left|\psi_k\right\rangle\left\langle\psi_l\right|\,. \tag{3.16}$$

Because the matrices $\left[\boldsymbol{V}_D^\alpha, \boldsymbol{V}_D^\beta\right] = 0$ for all α and β, the exponential of a sum in the unitary matrix can be written as a product of exponential functions:

$$e^{\boldsymbol{S}} = \exp\left(-\frac{i}{\hbar}\sum_\alpha \omega_\alpha^{-2} p_\alpha \boldsymbol{V}_D^\alpha\right) \tag{3.17}$$

$$= \exp\left(\sum_\alpha \sqrt{\frac{\omega_\alpha}{2\hbar}}\omega_\alpha^{-2}\left(b_\alpha^\dagger - b_\alpha\right)\boldsymbol{V}_D^\alpha\right) \tag{3.18}$$

$$= \prod_\alpha \exp\left(\sqrt{\frac{\omega_\alpha}{2\hbar}}\omega_\alpha^{-2}\left(b_\alpha^\dagger - b_\alpha\right)\boldsymbol{V}_D^\alpha\right). \tag{3.19}$$

This unitary operator is simply the position shift operator, so that its effect on operators of the bath subspace is:

$$e^{\boldsymbol{S}} b_\alpha e^{-\boldsymbol{S}} = b_\alpha - \sqrt{\frac{\omega_\alpha}{2\hbar}}\frac{\boldsymbol{V}_D^\alpha}{\omega_\alpha^2} \tag{3.20}$$

$$e^{\boldsymbol{S}} b_\alpha^\dagger e^{-\boldsymbol{S}} = b_\alpha^\dagger - \sqrt{\frac{\omega_\alpha}{2\hbar}}\frac{\boldsymbol{V}_D^\alpha}{\omega_\alpha^2} \tag{3.21}$$

$$e^{\boldsymbol{S}} q_\alpha e^{-\boldsymbol{S}} = q_\alpha - \frac{\boldsymbol{V}_D^\alpha}{\omega_\alpha^2} \tag{3.22}$$

$$e^{\boldsymbol{S}} p_\alpha e^{-\boldsymbol{S}} = p_\alpha\,. \tag{3.23}$$

For an operator in the system subspace, $\boldsymbol{A}$, we will define

$$\tilde{\boldsymbol{A}} \equiv e^{\boldsymbol{S}} \boldsymbol{A} e^{-\boldsymbol{S}}\,. \tag{3.24}$$

Note that $\tilde{\boldsymbol{A}}$ is an operator in both the system and bath subspaces. Given these relationships, we can transform each term in the Hamiltonian in Eq. (3.13).

System Hamiltonian: $\tilde{\boldsymbol{H}}_S$

First, we will transform the system Hamiltonian:

$$\tilde{\boldsymbol{H}}_S = e^{\boldsymbol{S}} \boldsymbol{H}_S e^{-\boldsymbol{S}} \tag{3.25}$$

$$= e^{\boldsymbol{S}}\left(\sum_n E_n \left|\psi_n\right\rangle\left\langle\psi_n\right|\right) e^{-\boldsymbol{S}} \tag{3.26}$$

$$= \prod_{\alpha\beta} \exp\left(\sqrt{\frac{\omega_\alpha}{2\hbar}}\omega_\alpha^{-2}\left(b_\alpha^\dagger - b_\alpha\right)\boldsymbol{V}_D^\alpha\right)\boldsymbol{H}_S \exp\left(\sqrt{\frac{\omega_\beta}{2\hbar}}\omega_\beta^{-2}\left(b_\beta^\dagger - b_\beta\right)\boldsymbol{V}_D^\beta\right) \tag{3.27}$$

$$= \boldsymbol{H}_S\,. \tag{3.28}$$

Because $[\boldsymbol{H}_S, \boldsymbol{V}_D^\alpha] = 0$, the system Hamiltonian is unchanged.

Bath Hamiltonian: $\tilde{H}_B$

Now, we will transform the bath Hamiltonian:

$$\tilde{H}_B = e^{\boldsymbol{S}} H_B e^{-\boldsymbol{S}} \tag{3.29}$$

$$= \frac{1}{2}\sum_\alpha p_\alpha^2 + \frac{1}{2}\sum_\alpha \omega_\alpha^2 \left(q_\alpha - \frac{\boldsymbol{V}_D^\alpha}{\omega_\alpha^2}\right)^2 \tag{3.30}$$

$$= \frac{1}{2}\sum_\alpha p_\alpha^2 + \frac{1}{2}\sum_\alpha \omega_\alpha^2 \left(q_\alpha^2 - \frac{2\boldsymbol{V}_D^\alpha}{\omega_\alpha^2} q_\alpha + \frac{\left(\boldsymbol{V}_D^\alpha\right)^2}{\omega_\alpha^4}\right) \tag{3.31}$$

$$= \frac{1}{2}\sum_\alpha p_\alpha^2 + \frac{1}{2}\sum_\alpha \omega_\alpha^2 q_\alpha^2 - \sum_\alpha \boldsymbol{V}_D^\alpha q_\alpha + \frac{1}{2}\sum_\alpha \omega_\alpha^{-2}\left(\boldsymbol{V}_D^\alpha\right)^2 \tag{3.32}$$

$$= H_B - \sum_\alpha \boldsymbol{V}_D^\alpha q_\alpha + \frac{1}{2}\sum_\alpha \omega_\alpha^{-2}\left(\boldsymbol{V}_D^\alpha\right)^2 \ . \tag{3.33}$$

System-bath coupling: $\tilde{\boldsymbol{V}}_{SB}$

Finally, we will transform the exciton-phonon coupling:

$$\tilde{\boldsymbol{V}}_{SB} = e^{\boldsymbol{S}} \boldsymbol{V}_{SB} e^{-\boldsymbol{S}} \tag{3.34}$$

$$= e^{\boldsymbol{S}} \left[\sum_\alpha \sqrt{\frac{\hbar}{2\omega_\alpha}} \boldsymbol{V}^\alpha \left(b_\alpha^\dagger + b_\alpha\right)\right] e^{-\boldsymbol{S}} \tag{3.35}$$

$$= e^{\boldsymbol{S}} \sum_\alpha \sqrt{\frac{\hbar}{2\omega_\alpha}} \left[\boldsymbol{V}^\alpha b_\alpha^\dagger + b_\alpha \boldsymbol{V}^\alpha\right] e^{-\boldsymbol{S}} \tag{3.36}$$

$$= \sum_\alpha \sqrt{\frac{\hbar}{2\omega_\alpha}} \left[e^{\boldsymbol{S}} \boldsymbol{V}^\alpha e^{-\boldsymbol{S}} e^{\boldsymbol{S}} b_\alpha^\dagger e^{-\boldsymbol{S}} + e^{\boldsymbol{S}} b_\alpha e^{-\boldsymbol{S}} e^{\boldsymbol{S}} \boldsymbol{V}^\alpha e^{-\boldsymbol{S}}\right] \tag{3.37}$$

$$= \sum_\alpha \sqrt{\frac{\hbar}{2\omega_\alpha}} \left[\tilde{\boldsymbol{V}}^\alpha \left(b_\alpha^\dagger - \sqrt{\frac{\omega_\alpha}{2\hbar}} \frac{\boldsymbol{V}_D^\alpha}{\omega_\alpha^2}\right) + \left(b_\alpha - \sqrt{\frac{\omega_\alpha}{2\hbar}} \frac{\boldsymbol{V}_D^\alpha}{\omega_\alpha^2}\right) \tilde{\boldsymbol{V}}^\alpha\right] \tag{3.38}$$

$$= \frac{1}{2}\sum_\alpha \left[\tilde{\boldsymbol{V}}^\alpha \left(q_\alpha - \frac{i}{\omega_\alpha} p_\alpha\right) + \left(q_\alpha + \frac{i}{\omega_\alpha} p_\alpha\right) \tilde{\boldsymbol{V}}^\alpha - \omega_\alpha^{-2}\left(\tilde{\boldsymbol{V}}^\alpha \boldsymbol{V}_D^\alpha + \boldsymbol{V}_D^\alpha \tilde{\boldsymbol{V}}^\alpha\right)\right] \ . \tag{3.39}$$

Polaron-transformed Hamiltonian

Combining these results gives

$$\begin{aligned}\tilde{\boldsymbol{H}} =& \boldsymbol{H}_S + \frac{1}{2}\sum_\alpha \omega_\alpha^{-2}\left(\boldsymbol{V}_D^\alpha\right)^2 + H_B - \sum_\alpha \boldsymbol{V}_D^\alpha x_\alpha \\ &+ \frac{1}{2}\sum_\alpha \left[\tilde{\boldsymbol{V}}^\alpha\left(q_\alpha - \frac{i}{\omega_\alpha}p_\alpha\right) + \left(q_\alpha + \frac{i}{\omega_\alpha}p_\alpha\right)\tilde{\boldsymbol{V}}^\alpha - \omega_\alpha^{-2}\left(\tilde{\boldsymbol{V}}^\alpha \boldsymbol{V}_D^\alpha + \boldsymbol{V}_D^\alpha \tilde{\boldsymbol{V}}^\alpha\right)\right] \qquad (3.40)\\ =& \sum_n \left(E_n - \lambda_n\right)|\psi_n\rangle\langle\psi_n| + H_B \\ &+ \frac{1}{2}\sum_{\alpha n\neq m}\left[\tilde{V}_{n,m}^\alpha\left(q_\alpha - \frac{i}{\omega_\alpha}p_\alpha\right) + \left(q_\alpha + \frac{i}{\omega_\alpha}p_\alpha\right)\tilde{V}_{n,m}^\alpha\right]|\psi_n\rangle\langle\psi_m| \\ &- \sum_{n\neq m}\tilde{\lambda}_{nm}|\psi_n\rangle\langle\psi_m| \ , \qquad (3.41)\end{aligned}$$

where

$$\lambda_n \equiv \frac{1}{2}\sum_\alpha \omega_\alpha^{-2}\left(V_{n,n}^\alpha\right)^2 \qquad (3.42)$$

$$\tilde{\lambda}_{nm} \equiv \frac{1}{2}\sum_\alpha \omega_\alpha^{-2}\tilde{V}_{n,m}^\alpha\left(V_{m,m}^\alpha + V_{n,n}^\alpha\right) \qquad (3.43)$$

$$\tilde{V}_{n,m}^\alpha \equiv \exp\left(-\frac{i}{\hbar}\sum_\alpha \omega_\alpha^{-2}p_\alpha V_{n,n}^\alpha\right)V_{n,m}^\alpha \exp\left(+\frac{i}{\hbar}\sum_\alpha \omega_\alpha^{-2}p_\alpha V_{m,m}^\alpha\right) . \qquad (3.44)$$

We can replace the quantum position and momentum operators with their classical counterparts so that they commute with one another, simplifying the above equation to:

$$\begin{aligned}\tilde{\boldsymbol{H}} =& \sum_n \left(E_n - \lambda_n\right)|\psi_n\rangle\langle\psi_n| + H_B \\ &+ \sum_{\alpha n\neq m}\tilde{V}_{n,m}^\alpha|\psi_n\rangle\langle\psi_m| q_\alpha - \sum_{n\neq m}\tilde{\lambda}_{nm}|\psi_n\rangle\langle\psi_m| \ . \qquad (3.45)\end{aligned}$$

This Hamiltonian lends itself to a simple perturbation theory, where the first line on the right-hand side of Eq. (3.45) describes the system, where the energies of states are renormalized by the reorganization energies, and the bath. The second lines describe the coupling between states through the bath. The first term of the system-bath coupling, $\sum_\alpha \tilde{V}_{n,m}^\alpha|\psi_n\rangle\langle\psi_m| q_\alpha$, mirrors the EXPC in Eq. (3.13) but the EXPC matrix elements are dressed by exponential functions, which can be interpreted as a rescaling of the EXPC by a set of mode shifts that are related to the Franck-Condon factors of the system [179].

These exponential functions give rise to multiphonon processes in the Fermi's golden rule rate, which can be seen by performing a Taylor expansion of the exponential functions in

$\tilde{V}^{\alpha}_{n,m} q_\alpha$. The zeroth order expansion yields the form of the original EXPC to first order in the phonon mode coordinates, which gives rise to single-phonon processes. Higher order terms of the expansion describe the EXPC to higher orders of the phonon mode coordinates, accounting for multiphonon processes:

$$\begin{aligned}\tilde{V}^{\alpha}_{n,m} q_\alpha =& V^{\alpha}_{n,m} q_\alpha \\ &- \frac{i}{\hbar} \sum_{\beta} \omega_\beta^{-2} p_\beta \left(V^{\beta}_{n,n} - V^{\beta}_{m,m} \right) V^{\alpha}_{n,m} q_\alpha \\ &+ \frac{1}{\hbar^2} \sum_{\beta\gamma} \omega_\beta^{-2} \omega_\gamma^{-2} p_\beta p_\gamma V^{\beta}_{n,n} V^{\gamma}_{m,m} V^{\alpha}_{n,m} q_\alpha \\ &+ \dots . \end{aligned} \tag{3.46}$$

3.3 Ultrafast relaxation enabled by efficient multiphonon emission

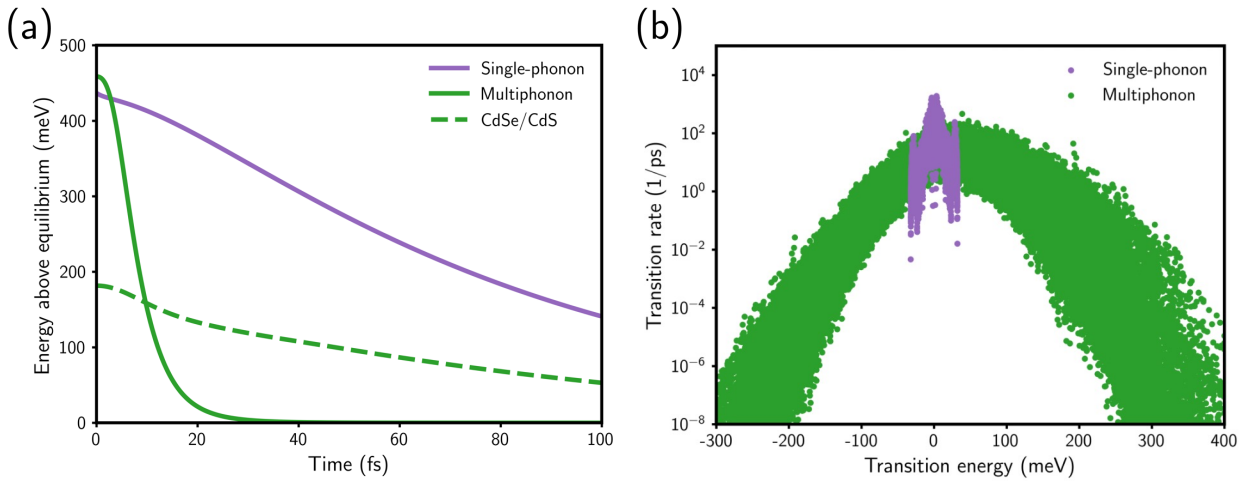

Figure 3.4: (a) The average energy above thermal equilibrium calculated for a 3.9 nm CdSe NC shows that cooling simulated using multiphonon rates occurs within 30 fs, much faster than when simulated using single-phonon rates. Cooling is an order of magnitude slower in a 3.9 nm CdSe NC with 3 monolayers of CdS shell. (b) The transition rates calculated for a 3.9 nm CdSe NC within the single-phonon and multiphonon schemes. The single-phonon rates vanish for transition energies larger than the greatest phonon frequency while the multiphonon rates cover a wide range of transition energies.

Hot exciton cooling dynamics were simulated for a 3.9 nm CdSe NC using master equations generated from both the single-phonon and non-Markovian, multiphonon rates. Fig 3.4a shows the average energy, which is calculated as

$$\langle E(t)\rangle = \sum_n E_n\big(p_n(t) - p_{n,\mathrm{eq}}\big) \tag{3.47}$$

$$\langle \varepsilon(t)\rangle = \sum_n \varepsilon_n\big(p_n(t) - p_{n,\mathrm{eq}}\big) \tag{3.48}$$

for the single-phonon and multiphonon schemes, respectively, where $p_n(t)$ is the population of state n at time t and $p_{n,\mathrm{eq}}$ is the population of state n at thermal equilibrium. Within the multiphonon scheme, the average energy relaxes within 30 fs, much faster within the single-phonon scheme.

Examining the transition rates as a function of transition energy, illustrated in Fig. 3.4b, demonstrates that the single-phonon rates are larger for low-energy transitions, but there are no single-phonon transitions between excitonic states that have energy differences greater than ∼32 meV (*i.e.*, greater than the largest phonon energy). The multiphonon rates, however, cover the full range of transition energies, making accessible many more relaxation channels and leading to cooling that occurs five times faster than cooling resulting from single-phonon processes alone. The fast multiphonon relaxation is a result of the large number of phonon modes (approximately 3000 modes for a 3.9 nm CdSe NC) that quasi-continuously span a wide frequency range. Thus, many phonon combinations satisfy the energy conservation requirement for phonon-mediated exciton transitions, leading to efficient relaxation *via* the emission of multiple phonons. The asymmetry in rates about 0 meV transition energy reflects detailed balance, which is enforced by the quantum correction factor introduced in Eq. (3.10). Furthermore, Fig. 3.4b shows a Gaussian relationship between the transition energy and the transition rate instead of the exponential dependence of the rate on the energy gap that results from the assumption that only the highest-frequency modes participate in nonradiative transitions [182].

Fig. 3.4a also shows that the timescale of energy relaxation for a 3.9 nm CdSe core with 3 monolayers of CdS shell is an order of magnitude slower than that of a bare CdSe core. The core/shell NC has a larger number of modes that span a wider frequency range, due to the higher optical frequencies of the CdS shell. However, the overall magnitude of EXPC is a factor of three smaller in the core/shell NC, suggesting that EXPC plays a large role in determining the timescale of cooling.

To allow for comparison between our calculations and experimental measurements, we simulate changes in the absorption spectrum of a system initially excited to the $1P$ excitonic state as it relaxes to the $1S$ ground excitonic state. The ground state absorption [183] is given by

$$\sigma_{\mathrm{gs}}(\omega) \propto \sum_n |\boldsymbol{\mu}_n|^2 \omega \delta(\omega - E_n)\,, \tag{3.49}$$

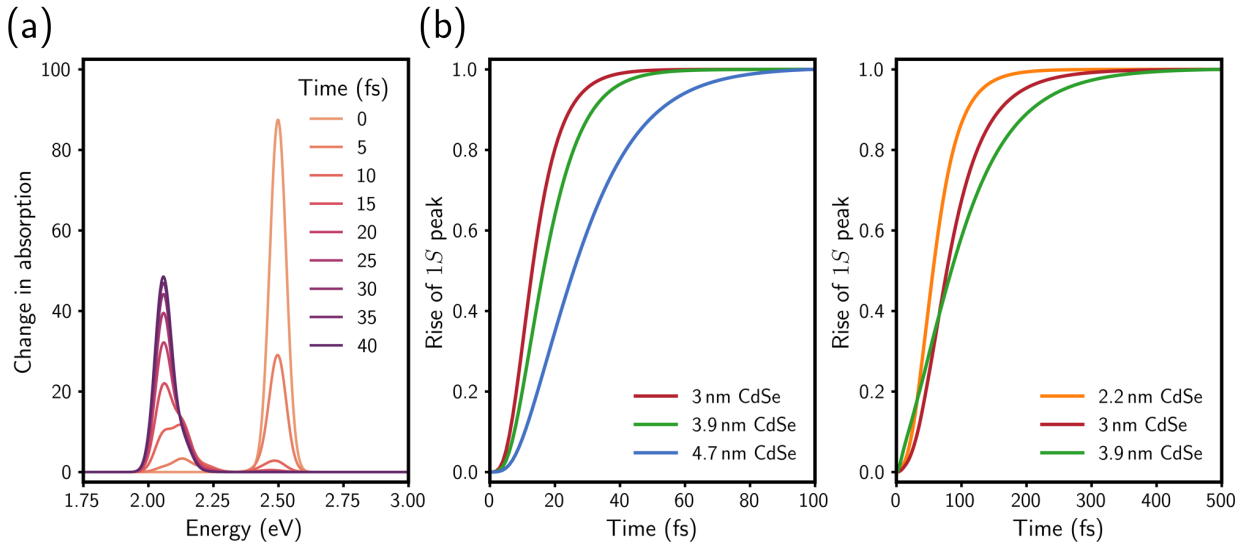

Figure 3.5: (a) The calculated change in absorption, $-\Delta\sigma(\omega, t)$, for a 3.9 nm CdSe NC. The rise of the $1S$ ground excitonic peak reflects the process of hot exciton cooling. (b) The calculated rise of the $1S$ ground excitonic peak for CdSe (left) and CdSe/CdS core/shell (right) NCs with 3 monolayers of CdS shell. Cooling is faster for smaller core sizes and in bare core NCs than in core/shell NCs.

where $\boldsymbol{\mu}_n$ is the transition dipole moment from the ground state to excitonic state n:

$$\boldsymbol{\mu}_n = \sum_{ai} c_{a,i}^n \int d\boldsymbol{r} \phi_a(\boldsymbol{r}) \boldsymbol{r} \phi_i(\boldsymbol{r}) \,. \tag{3.50}$$

Here, $c_{a,i}^n$ are the Bethe-Salpeter coefficients introduced in Eq. (2.4), and $\phi_a(\boldsymbol{r})$ and $\phi_i(\boldsymbol{r})$ are the real-space quasi-electron and quasi-hole wavefunctions, respectively. Assuming that the electric field, $\mathcal{E}$, is weak, such that the population of the ground state remains approximately 1 and that population of the excited state is proportional to $\mathcal{E}^2$, the time-dependent excited state absorption is given by:

$$\sigma_{\text{exc}}(\omega, t) \propto \sum_n |\boldsymbol{\mu}_n|^2 \omega \big(1 - \mathcal{E}^2 p_n(t)\big) \delta(\omega - E_n) \,, \tag{3.51}$$

where $p_n(t)$ is the population of state n at time t. Thus, the change in absorption is given by

$$\Delta\sigma(\omega, t) = \sigma_{\text{gs}}(\omega) - \sigma_{\text{exc}}(\omega, t) \tag{3.52}$$

$$\propto -\omega \mathcal{E}^2 \sum_n |\boldsymbol{\mu}_n|^2 p_n(t) \delta(\omega - E_n) \,. \tag{3.53}$$

The change in absorption, $-\Delta\sigma(\omega, t)$, for a 3.9 nm CdSe NC is illustrated in Fig. 3.5a, showing a fast decay of the $1P$ excitonic peak and a slower rise of the $1S$ ground excitonic peak. The dynamics of the rise of the $1S$ reflect those of hot exciton cooling. Fig. 3.5b depicts the rise dynamics of CdSe NCs and CdSe/CdS core/shell NCs with 3 monolayers of CdS shell. In agreement with experiment, our simulations show faster cooling for smaller CdSe NCs. Smaller NCs have larger excitonic gaps due to quantum confinement and a smaller number of phonon modes, but they have stronger EXPC than larger NCs. Similarly, core/shell NCs, which have significantly weaker EXPC due to suppressed coupling to surface phonon modes [82], show cooling that is an order of magnitude slower than those of bare cores.

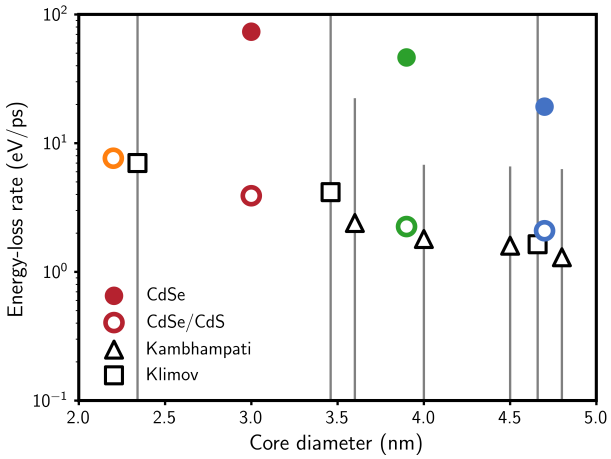

Figure 3.6: The energy loss rates calculated for CdSe and CdSe/CdS core/shell NCs. Core/shell structures all have 3 monolayers of shell. The black symbols correspond to measurements performed on CdSe NCs using transient absorption by Klimov *et al.* [56] and state-resolved pump-probe spectroscopy by Cooney *et al.* [64]. Vertical grey lines correspond to experimental error bars.

For each system, the rise dynamics were fit to an exponential function, and the extracted timescale was divided by the energy difference between the $1P$ and $1S$ excitonic peaks to yield an energy loss rate. The calculated energy loss rates are illustrated in Fig. 3.6 along with those measured experimentally using transient absorption spectroscopy [56] and state-resolved pump-probe spectroscopy [64]. While Fig. 3.6 initially suggests that the calculated energy loss rates for CdSe NCs are much larger than the measured values, those experiments use ∼100 fs pulses that obscure the observation of dynamics between states with spectral overlap, like those measured here, and they measure NCs with very low photoluminescence quantum yields of around 1%. Two-dimensional electronic spectroscopy measurements, which are able to clearly resolve the features corresponding to excitonic relaxation, on

3.5 nm CdSe NCs show that hot exciton cooling occurs within ∼30 fs [85], which is consistent with our findings.

3.4 Cooling timescales are governed by exciton-phonon couplings and phonon frequency range

To better understand the mechanism and role of different phonon frequencies in the cooling process, we calculated the rates and simulated dynamics for a 3.9 nm CdSe NC while eliminating low-frequency modes (Fig. 3.7a). We see that the timescale of relaxation doubles when modes with frequencies less than 1.5 THz (6.2 meV) are eliminated. When additional low-frequency modes are eliminated, relaxation becomes extremely slow. As illustrated by the transition rates calculated using these different schemes, low-frequency modes are crucial for efficient relaxation, especially for transitions between states that are close in energy. For example, when modes less than 4.0 THz (16.5 meV) are eliminated, all transitions with that energy or smaller must occur *via* multiphonon (*i.e.*, absorption and emission) processes of higher-frequency modes, which have weaker EXPC than lower-frequency modes, decreasing those transition rates by over an order of magnitude.

We also computed dynamics while eliminating low-frequency modes and rescaling the remaining EXPCs by a factor that kept consistent the reorganization energy of the ground state exciton, resulting in a modified spectral density (inset of Fig. 3.7b). We find small changes in the relaxation timescale, but no more than by a factor of three, indicating that the timescale of relaxation is largely governed by the overall magnitude of EXPC, and it is not sensitive to the distribution of those couplings to modes of different frequencies. Still, we see that the transition rates are slower in the modified spectral densities that do not include modes with frequencies less than 4.0 THz, suggesting that energy conservation requirement is more difficult to satisfy with a smaller frequency range of the bath.

Finally, we return to the Auger-assisted cooling mechanism, which was first proposed to explain the breaking of the phonon bottleneck [178]. We projected our simulated exciton cooling dynamics for a 3.9 nm CdSe NC to a single-particle picture of noninteracting electron-hole pair states, shown in Fig. 3.8, and find that the Auger cooling mechanism emerges naturally from our excitonic dynamics. The hole quickly relaxes to the band edge *via* phonon emission followed by electron relaxation by ∼400 meV that results in hole re-excitation, and then the hole once again relaxes to the band edge. This result indicates that both Coulomb-mediated electron-hole correlations, which are inherent in our formalism, and multiphonon-mediated excitonic transitions are required to circumvent the phonon bottleneck and lead to ultrafast timescales of hot exciton cooling.

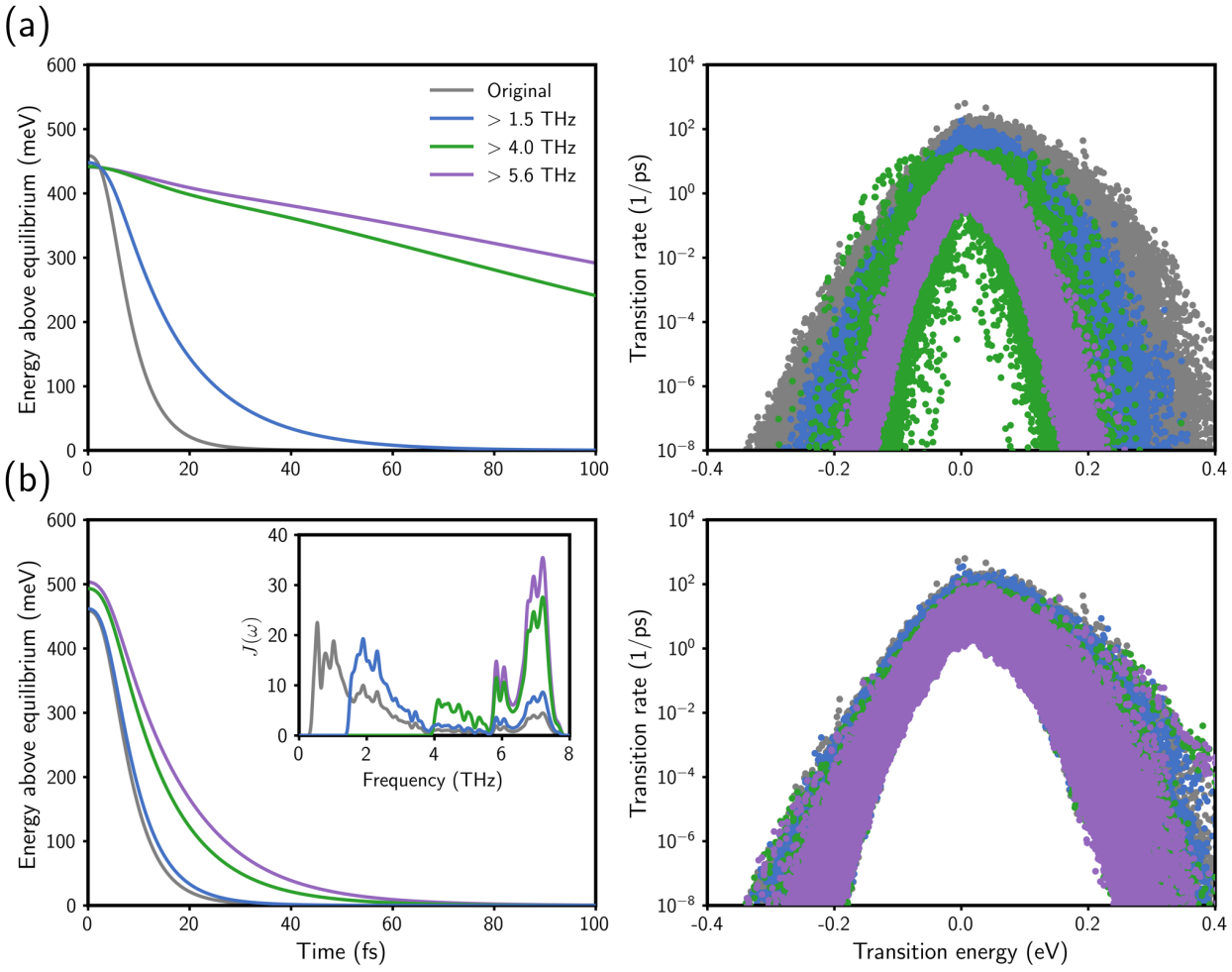

Figure 3.7: (a) Dynamics (left) and transition rates (right) calculated for a 3.9 nm CdSe NC while eliminating low-frequency modes. (b) Dynamics (left) and transition rates (right) calculated for a 3.9 nm CdSe NC while eliminating low-frequency modes and rescaling EXPCs to maintain the ground excitonic state reorganization energy. Rescaling EXPCs results in modified spectral densities, which are shown in the inset.

3.5 Conclusions

Hot exciton cooling in confined semiconductor NCs involves rich physics, including electron-hole correlations, EXPC, and multiphonon-mediated nonradiative transitions—all of which are required to break the phonon bottleneck and enable fast relaxation. We have developed the first atomistic theory that describes multiphonon-mediated exciton dynamics in NCs of experimentally relevant sizes. Our approach yields cooling timescales of tens of fs, which are

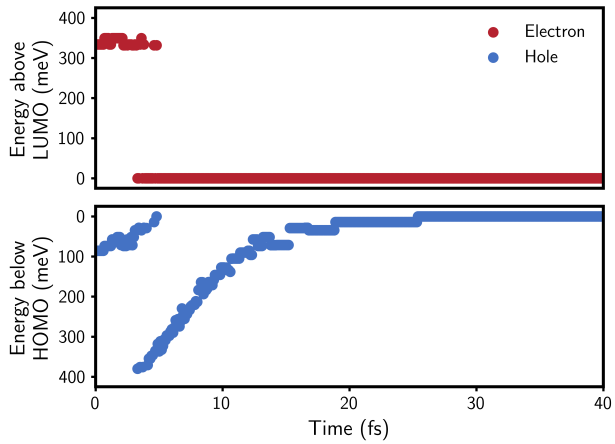

Figure 3.8: Projection of exciton cooling dynamics for a 3.9 nm CdSe NC onto a single-particle picture shows consistency with the Auger cooling mechanism. Hole relaxation is followed by an Auger-like process that leads to electron relaxation and hole re-excitation. The hole then relaxes again.

consistent with two-dimensional electronic spectroscopy measurements of similar systems. These ultrafast timescales are enabled by a cascade of multiphonon-mediated transitions between excitonic states that are relatively close in energy. These nonradiative transitions are made efficient by the large number of phonon modes in NCs that span a wide frequency range. The timescale of cooling is governed largely by the overall magnitude of EXPC, so that larger cores show slower relaxation, and core/shell NCs show relaxation that is slower by an order of magnitude.

This approach provides fundamental insights to phonon-mediated exciton dynamics at the nanoscale, which differ significantly from those in molecular and bulk semiconductor systems. These simulations provide the first unified, microscopic theory for hot exciton cooling in nanoscale systems that addresses longstanding questions regarding the timescales and mechanisms of this process and that provides design principles for NCs with tuned EXPC and cooling timescales. The framework presented here is sufficiently general that it can be used to study timescales and mechanisms of exciton dephasing and carrier trapping, dynamics in NCs of different dimensionalities, such as in nanorods and nanoplatelets, and materials, including III-V and perovskite semiconductors. Further elucidating the principles of phonon-mediated dynamics at the nanoscale is key to ultimately tuning these processes to realize novel phenomena in NC systems and NC-based applications with higher device efficiencies.

Chapter 4

Dynamic lattice distortions driven by surface trapping in semiconductor nanocrystals

Nonradiative processes limit optoelectronic functionality of nanocrystals (NCs) and curb their device performance. Ch. 3 investigated the timescales and mechanisms of hot exciton cooling, the process by which one exciton nonradiatively relaxes to the band edge of a NC. However, in many NC-based devices, NCs are exposed to high energy and/or high intensity excitation conditions, where several excitations are formed. In this chapter, we aim to understand the dynamic structural origins of nonradiative relaxation processes under such excitation regimes by performing atomistic simulations to corroborate femtosecond electron diffraction measurements. Experimental investigation of the excitation energy dependence in a core/shell system shows that hot carriers created by a photon energy considerably larger than the band gap induce structural distortions at NC surfaces on few picosecond (ps) timescales that are associated with the localization of trapped holes. On the other hand, carriers created by a photon energy close to the band gap of the core in the same system result in transient lattice heating that occurs on a much longer 200 ps timescale, dominated by an Auger heating mechanism. Elucidation of the structural deformations associated with the surface trapping of hot holes provides atomic-scale insights into the mechanisms deteriorating optoelectronic performance and a pathway towards minimizing these losses in NC-based devices. The content of this chapter is adopted with permission from Guzelturk, B.; Cotts, B. L.; Jasrasaria, D.; *et al.* Dynamic lattice distortions driven by surface trapping in semiconductor nanocrystals. *Nat. Commun.* **2021**, *12*, 1860.

4.1 Introduction

Nonradiative relaxation processes in materials represent fundamental loss mechanisms, which set performance limits in electronics, optoelectronics, and photocatalysis. Nonradiative re-

laxation events become further critical in devices of quantum-confined materials, such as nanocrystals (NCs) and nanowires, due to their high surface-to-volume ratios. As such, intensive research efforts have been focused on identifying nonradiative losses and the means to circumvent them in nanomaterials [184, 185]. Among these, colloidal semiconductor NCs have attracted significant technological interest due to their appealing optoelectronic properties [186, 187], which are tunable *via* shape, size, composition, and surface chemistry [1, 9, 185, 188]. Today, state of the art NCs can reach near-unity radiative efficiencies [68], but these are typically measured under moderately weak excitation conditions. In applications, such as lasers [189], photodetectors [190], multiexciton-harvesting solar cells [191], and electrically pumped LEDs [192], NCs are commonly exposed to high energy and/or high intensity excitation conditions, where nonradiative relaxation rapidly escalates.

Previously, high photon energy excitation of NCs has been shown to cause increased blinking [193], reduced photoluminescence quantum yields [194, 195], and increased photoionization [196]. These observations have suggested that hot carriers in NCs can lead to severe charge trapping, increasing nonradiative losses. In addition, Auger recombination (AR) becomes dominant in NCs that have more than one exciton [34]. In AR, one exciton nonradiatively recombines by transferring its energy to another carrier, hence substantially curbing the performance of NC lasers[197] and LEDs [198]. Although earlier works focused on identifying optical signatures associated with such nonradiative processes [199, 200], more recent works have begun to point to the fundamental role of dynamic structural fluctuations interrelated with nonradiative relaxation processes in NCs [117, 152, 165, 201–205]. In this context, neutron scattering measurements corroborated by molecular dynamics (MD) simulations [117] and correlative transmission electron microscopy (TEM) studies [202] have indicated that NC surfaces are mechanically soft, and thus may accelerate nonradiative relaxation processes. Nevertheless, such structural deformations associated with nonradiative relaxation in photoexcited NCs have remained elusive to date and have never been directly probed on ultrafast timescales.

In this chapter, we describe femtosecond electron diffraction [206] measurements on prototypical cadmium chalcogenide colloidal NCs to directly probe the atomic scale responses following photoexcitation. We investigate the effects of excitation photon energy on the transient atomic responses in thin film samples of core/shell CdSe/CdS and core-only CdSe NCs. We find that AR dominates the transient heating of the core/shell NCs when multiexcitons are generated in the core by photons with energies close to the band gap. The transient heating response is corroborated by MD simulations. On the other hand, we find that localized disordering is induced, in addition to transient heating, when multiexcitons are generated predominantly in the shell by photons with energies much larger than the band gap. These localized structural deformations arise from the trapping of hot holes at NC surfaces. Kinetic models considering these nonradiative relaxations capture the experimentally measured dynamics well. Furthermore, we present measurements on a core-only sample, which indicate that hole trapping occurs under both excitation photon energies but with different temporal dynamics, implying the presence of an energy barrier for hot hole surface-trapping in this system.

4.2 Ultrafast electron diffraction of CdSe/CdS nanocrystals

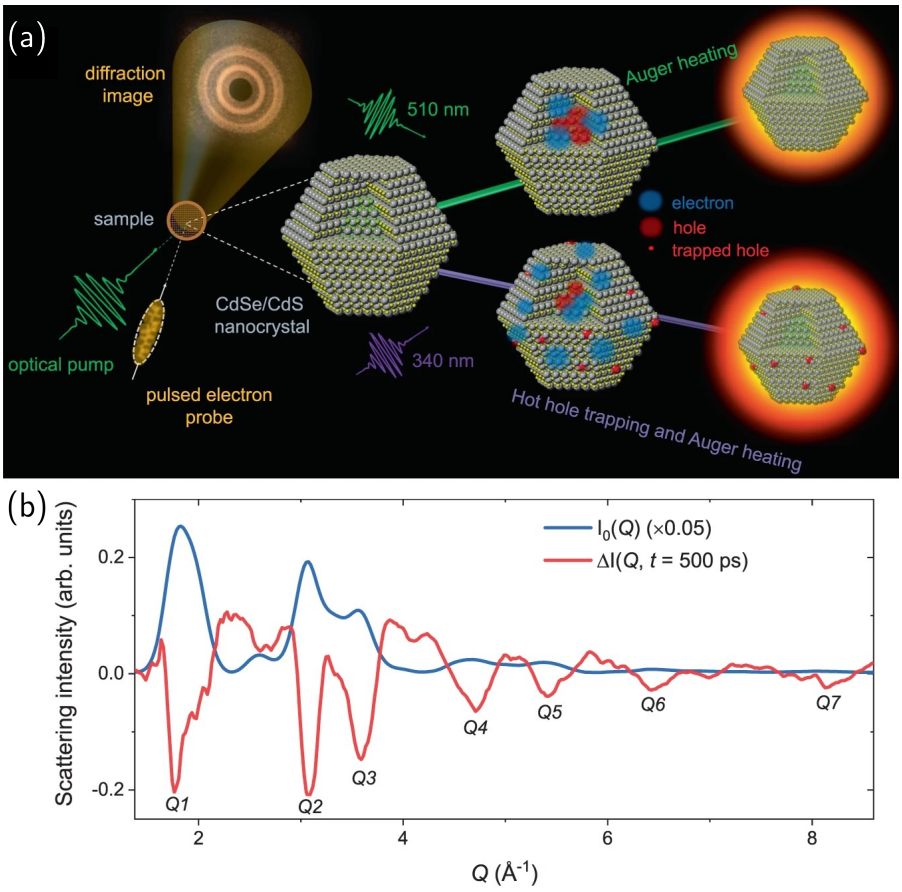

Figure 4.1: Femtosecond electron diffraction on colloidal NCs. (a) Schematic demonstration of the femtosecond electron diffraction, where we perform optical pump/electron-beam diffraction probe experiments on colloidal NCs deposited on TEM grids. We observe dynamic lattice heating and localized surface disordering associated with nonradiative relaxation in NCs. In a core/shell CdSe/CdS NC, Auger heating dominates the response with 510 nm excitation (green), while hot carrier surface trapping prevails with 340 nm excitation (purple). Electrons and holes are denoted by blue and red, respectively. (b) $I_0(Q)$ is the radially integrated diffraction intensity (blue) in a core/shell CdSe/CdS NC in the absence of optical pump. $\Delta I(Q, t = 500\,\text{ps})$ is the transient change in the diffraction intensity (red) measured at a pump/probe delay of 500 ps with 510 nm excitation under a fluence of 2.1 mJ cm^{-2}. Different diffraction peaks are labeled as $Q1 - Q7$.

Fig. 4.1a schematically depicts the femtosecond electron diffraction measurements performed in a transmission geometry, where we monitor the diffraction from NC thin films deposited on TEM grids as a function of pump-probe delay. Fig. 4.1b shows the radially integrated diffraction intensity in the absence of optical pump, $I_0(Q)$, where Q is the scattering vector as well as the transient change in the diffraction intensity $\Delta I(Q,t)$, measured at a pump-probe delay of $t = 500\,\text{ps}$ of a core/shell CdSe/CdS sample excited at 510 nm. The intensity of all diffraction peaks, labeled from $Q1$ to $Q7$, decreases transiently while the intensity in the diffuse scattering region (in-between the peaks) increases. The relative loss of diffraction peak intensity implies that the NCs become transiently disordered after photoexcitation.

4.3 Excitation with low photon energy in the core/shell nanocrystal

We first discuss measurements of the core/shell sample when excited at 510 nm, which predominantly excites the CdSe core.

4.3.1 Understanding relationships between Debye Waller factor, atomic mean square displacement, and temperature increase

Fig. 4.2 shows the relative diffraction intensity, $I(t)/I_0$, at four different diffraction peaks. Changes in $I(t)/I_0$ become progressively larger for higher Q peaks. This Q-dependence resembles a transient heating response known as the Debye-Waller (DW) effect, where diffraction peak intensities decrease as the material heats up due to increased atomic motion.

For a given temperature, the Debye-Waller factor (DWF) of a system can be computed at different Q values according to different assumptions [207]. Under the assumption of harmonic and isotropic atomic motion, the DWF is given by

$$\text{DWF}_{h,i} = \exp\left(-\frac{Q^2\langle u^2\rangle}{3}\right), \tag{4.1}$$

where Q is the magnitude of the scattering vector, and $\langle u^2\rangle$ is the mean square displacement (MSD) of atomic positions around an equilibrium configuration. When the atomic motion is assumed to be harmonic but not isotropic, the expression for the DWF is given by

$$\text{DWF}_{h} = \exp\left(-\langle \boldsymbol{Q}\cdot\boldsymbol{r}\rangle^2\right), \tag{4.2}$$

where $\boldsymbol{Q}$ is the scattering vector, and $\boldsymbol{r}$ are the atomic positions. Finally, when there are no assumptions made regarding the nature of atomic motion, the DWF is calculated as

$$\text{DWF} = \exp\left(\langle i\boldsymbol{Q}\cdot\boldsymbol{r}\rangle^2\right). \tag{4.3}$$

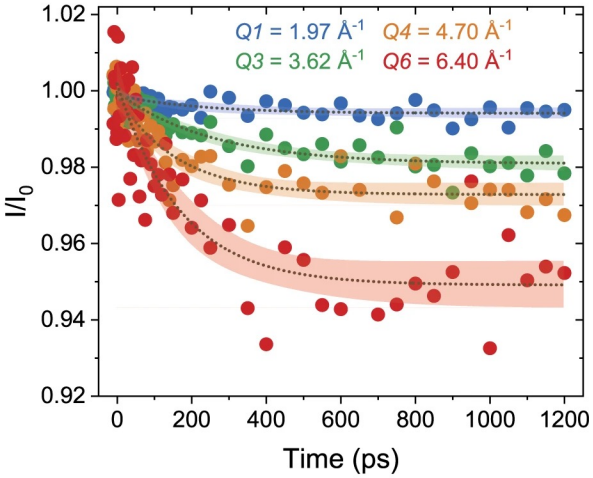

Figure 4.2: Femtosecond electron diffraction of a core/shell CdSe/CdS NC after optical excitation at 510 nm with a fluence of 2.1 mJ cm^{-2}. $I(t)/I_0$ is the relative diffraction intensity as a function of pump/probe delay shown for four different diffraction peaks, $Q1$, $Q2$, $Q3$, and $Q6$.

The DWF was computed according to each of these three expressions for a core/shell CdSe/CdS structure using the atomic positions from an equilibrium MD trajectory. The configurations of the CdSe and CdSe/CdS structures were obtained using the methods described in Ch. 2.1. Details of these configurations used here are collected in Table 4.1. All MD simulations were performed using the LAMMPS code [208] and an interaction potential with Lennard Jones and Coulomb terms that was previously parameterized for CdSe and CdS [123]. All trajectories are equilibrated at a given temperature using the Langevin thermostat implemented in LAMMPS.

Table 4.1: Core/shell CdSe/CdS NC configurations. All structures have a core diameter of 3.9 nm.

Configuration	Total diameter (nm)
$Cd_{462}Se_{462}$	3.9
$Cd_{2637}Se_{483}S_{2154}$	7.3
$Cd_{7872}Se_{483}S_{7389}$	10.3

As illustrated in Fig. 4.3a, for the examined range of Q values, the computed DWF are consistent with one another, even when the assumptions of harmonic and isotropic atomic motion are relaxed. Even though the CdSe/CdS structure has anharmonic and anisotropic

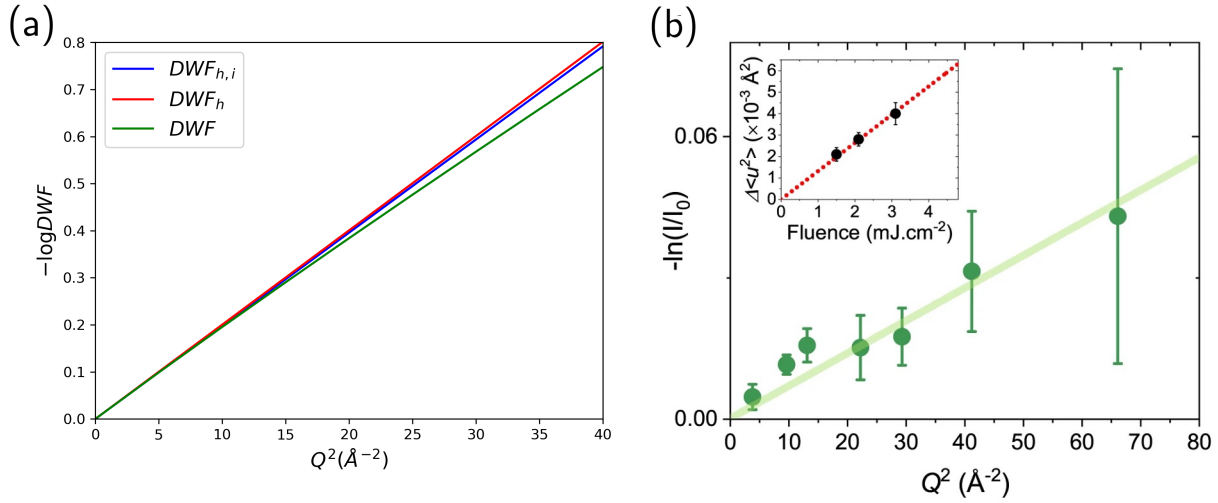

Figure 4.3: The log of the Debye-Waller factor (DWF) as a function of the square of the scattering vector, Q^2. (a) DWFs were calculated under the three different levels of approximation in Eqs. (4.1)-(4.3) for a CdSe/CdS core/shell nanocrystal (NC) with eight monolayers of shell using an equilibrium molecular dynamics simulation at 300 K. (b) $-\ln(I(t)/I_0)$ at t=1000 ps for a CdSe/CdS core/shell NC after optical excitation at 510 nm with a fluence of 2.1 mJ cm^{-2}. The inset shows the calculated induced atomic mean squared displacements, $\langle \Delta u(t)^2 \rangle$, for three different fluences. The error bars show standard error.

atomic motion, especially near the core/shell interface and NC surface, the small ratio of surface area to volume in this large NC leads to minimal differences. Because the deviation between the DWFs calculated at different levels of approximation is minimal over this range of Q values, the use of the experimentally measured DWF to compute the atomic MSD is justified for these systems.

Indeed, in agreement with the DW effect, the measured change in diffraction intensity, $-ln(I(t)/I_0)$, as a function of Q^2 at $t = 1000$ ps shows a linear relationship with zero intercept (Fig. 4.3b). This relationship holds for all fluences studied between 1.5 and 3.1 mJ cm^{-2}, implying that the time-dependent structural response of the core/shell NCs, when excited by 510 nm, primarily originates from transient heating. We use the change in DWF to estimate $\langle \Delta u(t)^2 \rangle$ according to Eq. (4.1), as shown in the inset of Fig. 4.3b, which scales linearly as a function of fluence, indicating that the absorbed energy density per NC also increases linearly with the excitation fluence.

Additionally, to relate the transient change in atomic MSD to changes in the temperature, equilibrium MD trajectories at different temperatures (150K, 300K, 310K, 320K, 400K, and 500K) were used to compute the MSD for the CdSe/CdS core/shell NC. The relationship between MSD and temperature was found to be linear with a slope of 0.000223 Å/K

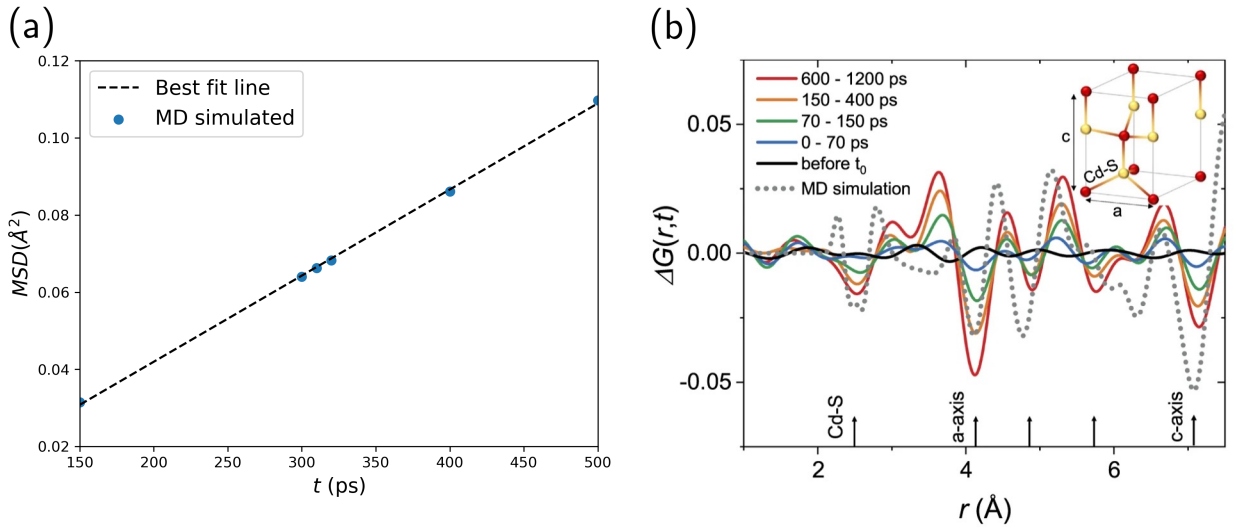

Figure 4.4: (a) Atomic MSD calculated for a core/shell CdSe/CdS NC with eight monolayers of shell using equilibrium MD simulations at different temperatures ranging from 150 K to 500 K, showing a linear relationship between MSD and temperature. (b) $\Delta G(r,t)$ is the differential atomic pair distribution function measured with respect to $G(r)$ of unexcited NCs at chosen time delays t. $\Delta G(r, \Delta T = 14\,\mathrm{K})$ is calculated using equilibrium MD simulations at different temperatures (grey, dotted line). The inset depicts a wurtzite CdS unit cell.

(Fig. 4.4a), in agreement with literature values for similar systems [207]. This value was used to compute the temperature rise of the NC after optical excitation.

To gain better insight into the structural deformations occurring in response to photoexcitation in these NCs, we calculate a differential atomic pair distribution function (PDF), $\Delta G(r,t)$, to revealing transient changes in the atomic pair correlations [209, 210]. In wurtzite CdSe (or CdS), the first atomic pair correlation peak is at 2.5 Å, which corresponds to the first nearest neighbor Cd–Se (or S) bond distance [211]. Higher order correlations, including those corresponding to the distances across the a- and c-axes of the unit cell (inset of Fig. 4.4) at 4.1 and 7.1 Å, respectively, are also observed. At each correlation distance, we observe a transient dip at the peak center and a rise on each side, as shown in Fig. 4.4b. This indicates that atomic pair correlations are transiently broadened, as expected from transient heating of the NCs [210].

To further validate this conclusion, we perform MD simulations to calculate $\Delta G(r, \Delta T)$ resulting from a static temperature increase of ΔT. Using the relationships between DWF, atomic MSD, and temperature increase determined above, an overall temperature increase of $\Delta T = 14\,\mathrm{K}$ was estimated under an excitation fluence of $2.1\,\mathrm{mJ\,cm^{-2}}$. Thus, to compute $\Delta G(r, \Delta T)$, two MD trajectories of the CdSe/CdS NC were equilibrated at 300 K and 314 K. The radial distribution function, $g(r)$, was computed directly using LAMMPS from the

equilibrium trajectory at each temperature and then transformed to the atomic PDF:

$$G(r) = 4\pi\rho_0 r[g(r) - 1]\,, \tag{4.4}$$

where ρ_0 is the average number density. The PDF at each temperature was then smoothed using a moving average technique with a smoothing window of 0.14 Å. Finally, the differential atomic PDF was computed by subtracting the atomic PDF at each temperature:

$$\Delta G(r, \Delta T = 14\,\mathrm{K}) = G(r, T = 314\,\mathrm{K}) - G(r, T = 300\,\mathrm{K})\,. \tag{4.5}$$

The simulated $\Delta G(r, \Delta T = 14\,\mathrm{K})$ is plotted in Fig. 4.4b, showing good agreement with the experimental $\Delta G(r, t)$, further supporting our conclusion that the lattice response in this case is dominated by transient heating.

4.3.2 Understanding long-lived heating response

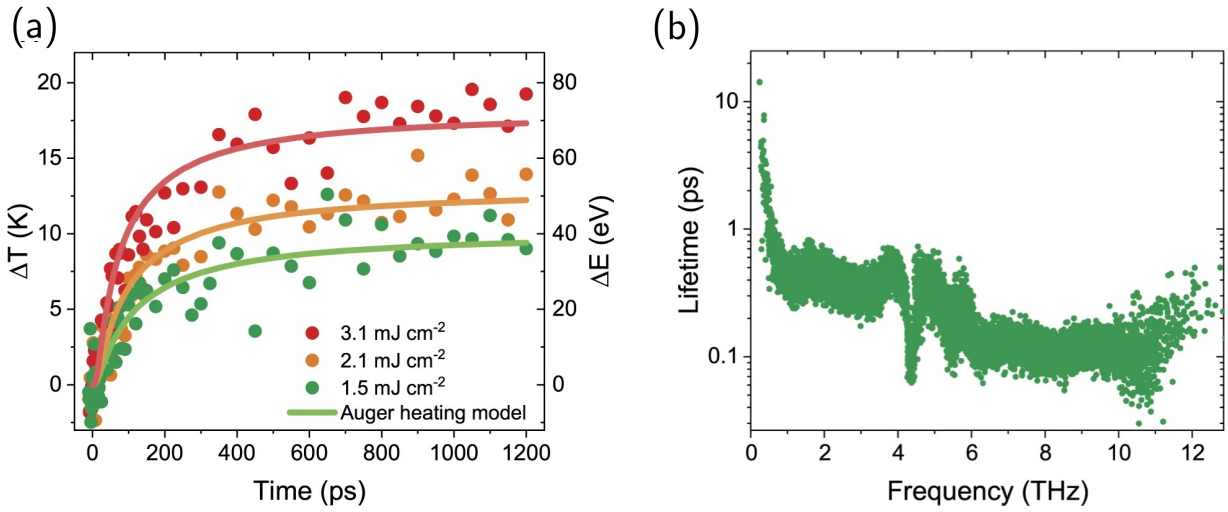

Figure 4.5: (a) $\Delta T(t)$ shows the transient increase in lattice temperature, and $\Delta E(t)$ shows the transient energy that is transferred from the initially optically-excited carriers to the lattice. The points show values computed from experimental diffraction data while the solid lines are simulated from a kinetic Auger heating model. (b) The phonon relaxation lifetimes for a core/shell CdSe/CdS NC with four monolayers of shell computed using equilibrium MD simulations at 300 K.

The transient changes in atomic MSD were converted to changes in lattice temperature $\Delta T(t)$ and energy $\Delta E(t)$, under the assumption that all excess energy from hot carriers was

transferred to the lattice (Fig. 4.5a). The change in lattice temperature was fit phenomenologically using a single exponential function, giving lifetimes on the order of 200 ps. This timescale implies an exceptionally gradual heating of the NCs, which could be explained either by (1) a bottleneck during the course of energy transfer from hot carriers into optical phonons and then into acoustic phonons [126], or (2) an Auger heating mechanism [212]. A bottleneck between hot carriers and optical phonons is not considered, as prior reports, as well as the simulations performed in Ch. 3, have established that this process is fast (*i.e.*, on the order of femtoseconds) in colloidal NCs [213]. However, a bottleneck may exist in the down-conversion of the emitted optical phonons into acoustic ones, where the acoustic phonons are more prominent in the DW response because of their larger contribution to atomic MSD [214]. Previously, a bottleneck between optical and acoustic phonons has been alluded to in lead-halide perovskites through a hot phonon bottleneck effect [126] due to the efficient up-conversion of acoustic phonons into the optical ones.

To assess this mechanism, MD simulations were used to calculate the phonon density of states and corresponding phonon relaxation lifetimes of a core/shell CdSe/CdS structure with four monolayers of CdS shell, shown in Fig. 4.5b. As described in detail in Ch. 2.3, the phonon lifetimes (*i.e.*, the T_1 timescale of relaxation of a populated phonon mode) were computed within linear response for each phonon mode [215–217].

The calculated phonon lifetimes are illustrated in Fig. 4.5b, showing sub-ps lifetimes for all modes except the lowest-frequency acoustic phonons, for which the lifetimes reach $\sim$10 ps. This timescale is still an order of magnitude faster than the observed heating of the NCs. While the phonon lifetimes are computed within linear response, *i.e.*, in the regime of a mode being slightly perturbed, we would expect the lifetime to be even shorter for response from a larger perturbation as well as for higher temperatures. Furthermore, while these results were computed for a core-shell structure with four monolayers of CdS shell, we believe that the lifetimes would not change significantly for a structure with eight monolayers of shell, for which the computational cost of computing and diagonalizing the dynamical matrix to compute the phonon density of states was prohibitive. Calculations of phonon lifetimes on the core-only structure at 300 K were comparable to the lifetimes for the four monolayer core/shell structure (Fig. 2.4b). This result suggests that the phonon lifetimes for the eight monolayer core/shell would be very similar to those shown here. Therefore, we rule out the hot phonon bottleneck as the primary mechanism underlying the observed slow heating response.

Next, we evaluated the hypothesis of an Auger heating mechanism, which arises due to the generation of hot carriers at delayed times *via* sequential AR events. We proposed a simple kinetic model that considers the Auger heating mechanism, where the rate of heating is approximately equal to the rate of AR. We considered the dependence of the AR rate [93] on the average number of excitons per NC, $\langle N \rangle$, as $\frac{N(N-1)}{2\tau_{\mathrm{AR}}}$, where τ_{AR} is the biexciton AR lifetime. We calculate $\langle N \rangle$ based on the absorption cross-section at 510 nm, which is $\sim$10 for a fluence of 1 mJ cm^{-2} and scales linearly with the fluence. Using these initial conditions, we solved the coupled differential equations of the kinetic model using the Gillespie algorithm

[218]. The biexciton AR lifetime was fit to simultaneously reproduce the experimental data, yielding $\tau_{AR} = 625\,\text{ps}$ in the eight monolayer core/shell NC, which is in excellent agreement with measurements and calculations of the same system [93, 219]. The Auger heating model (solid lines in Fig. 4.5a) completely captures the experimental dynamics, including both the timescale as well as the signal amplitude. This strongly implies that Auger heating is the predominant mechanism contributing to the transient heating of the core/shell NCs when many excitons are generated near the band edge in the core of the NCs.

4.4 Excitation with high photon energy in the core/shell nanocrystal

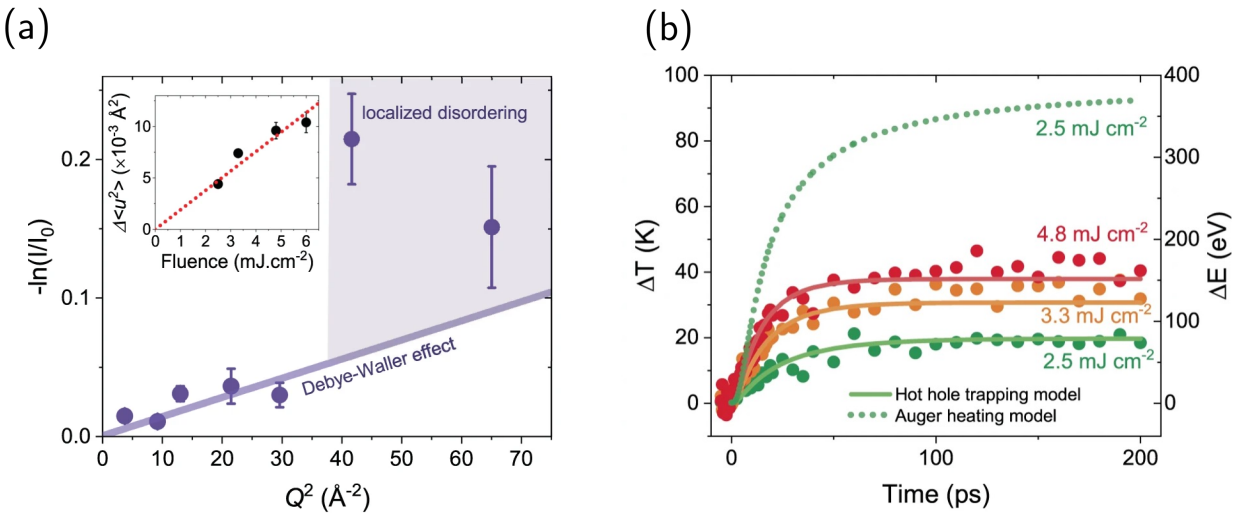

Figure 4.6: Femtosecond electron diffraction of a core/shell CdSe/CdS NC after optical excitation at 340 nm with a fluence of $2.5\,\text{mJ}\,\text{cm}^{-2}$. (a) $-\ln(I(t)/I_0)$ at t=200 ps plotted as a function of Q^2 show strong deviation from linearity for higher-Q peaks. This result indicates transient lattice disorder that cannot be explained from the Debye-Waller effect alone. The inset shows the calculated induced atomic MSD, $\langle \Delta u(t)^2 \rangle$, for three different fluences, and the error bars show standard error. (b) $\Delta T(t)$ and $\Delta E(t)$ computed from experimental diffraction data (points), simulated from a kinetic Auger heating model (dotted line), and simulated from a kinetic fast-trapping model (solid lines).

We now discuss 340 nm excitation of the core/shell NCs. Fig. 4.6b shows that the change in diffraction intensity occurs significantly faster (∼20 ps) under this excitation condition. Fig. 4.6a plots $-\ln(I(t)/I_0)$ by Q^2 at $t = 200\,\text{ps}$. Although low-Q diffraction peaks (Q1-Q5)

show a linear-like response, higher Q peaks ($Q6$ and $Q7$) strongly deviate from this linearity. This deviation happens consistently for all studied fluences between 2.5 and 6.0 mJ cm^{-2}. This suggests additional transient deformations occurring in these NCs concurrently with the transient heating. Particularly, the deviation at high Q implies that the induced disorder is linked to the formation of short-lengthscale, localized lattice deformations. This can be understood with the fact that a diffraction peak at Q probes a real space order of $2\pi/Q$, (*i.e.*, the $Q6$ peak at 6.4 Å^{-1} probes ∼1 Åin real space).

Hot carriers in the NCs can be trapped via localization of the carriers at the NC surfaces at ps timescales [199, 220–222], causing broad defect emission [220], reduced photoluminescence quantum yields [195], and increased blinking [193, 223]. *Ab initio* calculations have also suggested that trapping may be linked with the dynamic atomic fluctuations of the poorly passivated surface chalcogen atoms [222, 224–226]. Our observations here indicate that the localized lattice deformations are formed on ps timescales under 340 nm excitation, where hot carriers are dominantly excited in the shell region close to the surface of the NCs. In this context, we hypothesize that the localized atomic deformations arise from dynamic reconstruction of the NC surfaces as hot carriers localize at poorly passivated surface atoms forming surface small polarons [205]. To validate this hypothesis, we investigate $\Delta T(t)$ (Fig. 4.6b), which is estimated from the lower-Q peaks exhibiting DW-like response. Note here that, the $\langle N \rangle$ ∼100 at 2.5 mJ cm^{-2} estimated from the absorption cross-section at 340 nm. We find that the Auger heating model substantially overestimates the amplitude of $\Delta T(t)$ by a factor of four, as indicated by the dashed line in Fig. 4.6b. This implies that Auger heating must be suppressed in this case. Consistent with the hypothesis, AR has been observed to be repressed in the NCs with surface trapped holes [227] as the trapping leads to spatial separation of electrons and holes in a NC. We extend our kinetic model to account for the suppression of Auger heating due to competition with fast hot carrier surface trapping. We apply the time constant for formation of the localized deformations as the time scale for hot carrier trapping. As seen by the solid lines in Fig. 4.6b, this model agrees well with the experimental $\Delta T(t)$, which strongly implies that the transient structural response in the case of 340 nm excitation is dominated by the localized surface carrier trapping.

Both types of hot carriers are created in the shell region by 340 nm. Based on only this information, we cannot differentiate which carrier dominates the trapping process. However, with 510 nm excitation, hot carriers are created predominantly in the core region. Due to the band alignment between CdSe and CdS, electrons can be delocalized throughout the whole NC, while holes are localized to the core [93]. No significant localized deformations are observed with 510 nm excitation, which implies that the delocalized hot electrons cannot be the main cause of the surface trapping. Thus, hot holes must govern the formation of localized deformations as they trap at the NC surfaces. This is consistent with prior theoretical work in cadmium chalcogenide NCs, which have suggested that the main carrier that leads to trapping is the hole due to poorly passivated surface chalcogen atoms [203, 205, 222].

4.5 Excitation of the core-only nanocrystal

We also measure the transient structural responses in a CdSe core-only NC sample, which is the same size core used in the core/shell sample. We observe that the localized lattice deformations, evidenced by an increased loss at high Q diffraction peaks, occur under both excitation cases, while the effect is much more pronounced for the 340 nm excitation. The localized distortions emerge with a faster (7 ± 3 ps) time constant with 340 nm excitation, while the localized lattice disordering proceeds with a slow time constant of 167 ± 70 ps with the 510 nm excitation. This indicates that hot holes generated by 510 nm are not energetic enough to cause localized surface trapping, while those generated by 340 nm are. In the case of 510 nm excitation, AR leads to the generation of energetic hot holes at later times, which underlies the slower formation of localized deformations. This observation implies that there is a finite energy barrier for the formation of localized surface hole traps. Considering the excess energy of the hot holes in the core-only and core/shell NCs, we estimate that the energy barrier for hole trapping is between 0.1 and 0.36 eV.

4.6 Conclusions

Femtosecond electron diffraction applied to colloidal semiconductor NCs directly visualizes nonradiative relaxation occurring in photoexcited semiconductor NCs in real time with an atomic-scale resolution. With this, we uncover the dynamical structural responses associated with the formation of localized surface charge traps and AR. We show that hot holes with excess kinetic energy induce short range atomic deformations extending $\sim$0.15 Åas these carriers localize at surface trapping sites and form small surface polarons. Our results indicate that excitation energy management in NCs by minimizing the excess energy of hot hole is crucial to suppress nonradiative losses associated with surface trapping. As such, high energy excitation in NC lasers and energetic hole injection in LEDs should be avoided to minimize undesired surface trapping, important for wider technological deployment of semiconductor NCs in applications.

Chapter 5

Effects of exciton delocalization on the photoluminescence of near-infrared emissive InAs/InP/ZnSe nanocrystals

While the development of II-VI colloidal nanocrystals (NCs), such as the CdSe/CdS NCs that have been the focus of Chs. 2-4, with near-unity photoluminescence quantum yields (PLQYs) has been achieved [68], the development of bright III-V colloidal NCs, such as InAs, InP, GaAs, is still underway. These III-V materials are different from their II-VI counterparts in that they can emit in the near-infrared (NIR) region [228] as opposed to the visible region, and they have more significant dielectric screening [77, 229], which impacts their electronic properties. NIR-emissive NCs are important for diverse applications, such as bioimaging devices, telecommunications technologies, and down-conversion emitters for high-performance luminescent solar concentrators.

In this chapter, we use a combination of theoretical and experimental approaches to synthesize bright, NIR luminescent InAs/InP/ZnSe core/shell/shell NCs and elucidate fundamental material attributes that remain obstacles for development of near-unity PLQY NIR NCs. We employ atomistic electronic structure calculations to explore charge carrier behavior at the nanoscale affected by interfacial atomic structures and find that significant exciton occupation of the InP shell occurs in most cases despite expectations based on the InAs/InP type I bulk band alignment. Furthermore, the density of the valence band maximum (VBM) state extends anisotropically through the (111) crystal planes to the terminal InP surfaces/interfaces, indicating that surface defects located on the (111) facets play an outsized role in disrupting the VBM and quenching photoluminescence. We use this insight to develop synthetic methods for InAs/InP/ZnSe NCs that improve the emissive qualities of NIR emitters with large, tunable Stokes ratios, narrow emission linewidths, and high PLQYs, which reach 60±2%. The content of this chapter is adopted with permission from Enright, M. J.; Jasrasaria, D.; Hanchard, M. M.; *et al.* Role of atomic structure on exciton dynamics and photoluminescence in NIR emissive InAs/InP/ZnSe quantum dots. *J. Phys. Chem. C* **2022**, *126*, 7576.

5.1 Introduction

A substantial body of research over several decades has led to the development of colloidal nanocrystals (NCs) with optoelectronic properties in the ultraviolet (UV) and visible regions of the electromagnetic spectrum, which in turn has led to remarkable advancements that include new commercial technologies [230–236]. NCs with near-infrared (NIR, 750-1400 nm) emission have not yet attained the same utility despite exceptional promise across a wide spectrum of applications for which they are uniquely suited, such as photovoltaic energy conversion, luminescence concentration, telecommunications, and *in vivo* imaging [228, 231, 235–240]. Advancement of technologies based on NIR NC materials has been challenging for reasons that are physicochemical in nature due to the limited number of semiconductor materials that exist with useful, easily tunable optical properties at NIR frequencies, which has frustrated their development as compared to their UV and visible counterparts [228, 231, 233, 235–243]. It also remains a specific and urgent need to provide new NC material systems that are both cadmium- and lead-free, yet still afford NIR capabilities such as high photoluminescence quantum yields (PLQYs), stability against photodegradation, and narrow emission profiles [89, 244–250]. Realization of new NCs with these attributes are a prerequisite for development of high-performance technologies.

Among candidate semiconductor materials, InAs offers potential advantages as a central core for NCs with NIR optical gaps. Most notable is the body of prior work that demonstrates good prospects for developing InAs-based NCs offering higher PLQYs than other comparable NIR materials, including rare earth nanocrystals, silver chalcogenide nanocrystals, carbon nanotubes, Si nanoparticles, and organic dyes [251–256]. Unshelled, InAs cores have very low PLQYs – typically less than 2% due to rapid surface trapping of charges from poor surface passivation and localized states resulting from surface oxidation. These impacts can be remediated in part by encapsulation of the InAs core within a wide band gap, epitaxial shell material. Effective shell phases narrow emission linewidths and increase radiative recombination efficiencies through charge carrier confinement and passivation of the InAs core [90, 257, 258]. With few exceptions, the highest PLQY InAs NCs described in the current literature are ones passivated by cadmium chalcogenide protective shells, with reported PLQYs in excess of 80% [259]. However, the increased brightness is often accompanied by large bathochromic shifts, which are changes in the spectral band position toward longer wavelengths, of several hundred meV that can push the emission band beyond the NIR region [239, 258–260].

The encapsulation of other III-V cores, such as InP, within wide band gap II-VI shells has yielded PLQYs of >80% for InP/ZnSe and InP/ZnSeS [261–263]. However, for the InAs cores of interest in the current work, large lattice mismatches between InAs and wide band gap materials like ZnSe (6.4%) and ZnS (10.7%) limit defect-free growth of these layers to only a few monolayers at most [89, 264]. Studies investigating the incorporation of multiple intermediate layers and alloys to relieve strain and facilitate thicker ZnSe or ZnS shell growth yielded emitters with only modest PL quantum efficiencies [259, 264]. Further efforts using an alloyed core and a large interior shell obtained 75% PLQY for In(Zn)As/In(Zn)P/GaP/ZnS

NCs [265]. Bright, NIR emissive InAs/InP/ZnSe NCs with 76% PLQY have also been reported, though the specific structural and electronic attributes that enable bright quantum yields are not yet understood, especially when contrasted with the <30% PLQYs typically observed InAs/InP/ZnSe NCs [266].

Here, we examine InAs/InP/ZnSe NCs – heavy-metal-free, core/shell/shell heterostructure luminophores with exceptional promise for use in, for example, active absorber/emitter materials in high-performance LSCs for photovoltaic energy conversion. We employ a combination of experimental and computational strategies to develop a deeper understanding of the atomic-scale structural and electronic properties that enable (or inhibit) NIR emission in these NC heterostructures. Synthetically, we developed replicable methods for the synthesis of InAs/InP/ZnSe NCs with PLQYs of up to 60±2% and emission full width at half-maximum (FWHM) as narrow as 130 meV with tunable Stokes ratios and emission between 800 and 900 nm. Atomistic electronic structure calculations of InAs/InP NCs indicate that charge carriers in these materials are poorly confined to the InAs core despite the nested, type I band structure of the bulk materials. We find that the electron wavefunction extends isotropically into the shell but remains close to the InAs/InP interface. The hole, however, delocalizes anisotropically into the InP layer primarily in the [111] direction. Atomically resolved microscopy of InAs/InP/ZnSe NCs reveals that the growth process is also strongly anisotropic, leading to a shell encapsulation that is nonuniform (even in the brightest samples) and thinner in the [111] direction. An accompanying theoretical assessment of InP surface defects shows that the extent of overlap between surface defect states and the NC valence band states is orientation-dependent, such that defects located along the ⟨111⟩ axes play an outsized role in influencing the NC band structure, while defects elsewhere are surprisingly found to have almost no impact.

5.2 Synthesis and characterization of InAs/InP/ZnSe nanocrystals

InAs/InP/ZnSe core/shell/shell NCs are prepared in a three-step process, where InAs cores are nucleated by hot injection followed by epitaxial growth of InP and ZnSe shells. The evolving optical properties of the reaction mixture were followed by absorbance and photoluminescence spectroscopy, and high-angle annular dark-field-scanning transmission electron microscopy (HAADF-STEM) images of the final multishell NCs were obtained to ascertain their atomic structure. The progression of photophysical/spectroscopic properties through an illustrative sequence of growth stages is shown in Figs. 5.1a,b. Encapsulation within InP and ZnSe both lead to bathochromic shifts in the lowest energy excitonic transition in the absorbance spectra. Emission is extremely weak or not detected throughout InP shell growth but becomes pronounced upon ZnSe encapsulation — an impact that is marked even without a complete ZnSe monolayer. Ideally, the indicated sequences would lead to the schematic core/shell/shell structure illustrated in Fig. 5.1c. Representative STEM data

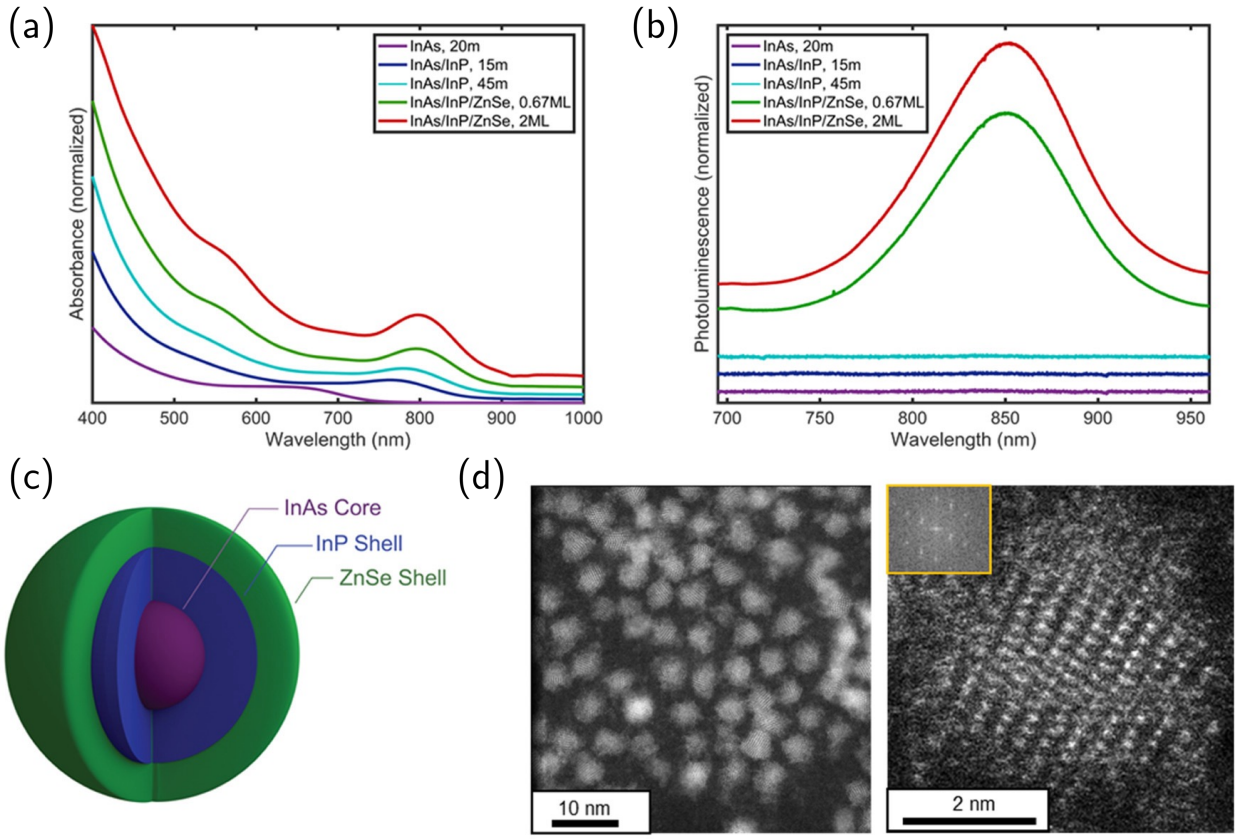

Figure 5.1: Synthesis of InAs/InP/ZnSe NCs with 1 nm thick InP and 2 monolayer thick ZnSe shells monitored by intermittent extractions over the course of the reaction. (a) The evolving absorbance and (b) photoluminescence of the NCs show an initial bathochromic shift of almost 100 nm upon initial growth of the InP shell followed by sharpening of absorbance features from the InAs core and InP shell when encapsulated within ZnSe. Photoluminescence is not observed until particles are treated with ZnSe. (c) A depiction of a spherical, core/shell/shell, InAs/InP/ZnSe NC. (d) Transmission electron micrographs of InAs/InP/ZnSe with 1 nm thick InP shells and a 10 nm scale bar (left) and an atomically resolved NC observed from the (211) plane with a 2 nm scale bar (right) with the inset of the power spectrum indicating the (211) zone axis.

shown in Fig. 5.1d demonstrate the high level of atomic order present in the InAs/InP/ZnSe NCs that are formed, as evidenced by the representative (211) zone axis projection shown in the inset.

The InP shell thickness is controlled using a successive ionic layer adsorption and reaction (SILAR) approach. Increasing the InP shell thickness but omitting the ZnSe shell, however, yields invariably weakly luminescent heterostructures with less than <1% PLQY.

STEM data (shown in Fig. 5.1d) reveal that the progression of shell growth is associated with the formation of increasingly anisotropic (tetrahedral-like) heterostructures. The phenomenon of zincblende crystal structures with a slightly tetrahedral shape has been observed previously for the growth of InAs/InP NC materials [265, 267, 268]. At the termination of the InP shell growth, subsequent encapsulation with ZnSe can be affected to give highly emissive InAs/InP/ZnSe particles – NCs with 60±2% PLQY and a narrow emission FWHM of 132 meV.

5.3 Atomistic electronic structure calculations of InAs/InP nanocrystals

The optimized sequence of growth steps outlined above yields NCs with large, but still far from unity, values of PLQY, and there remains a clear opportunity to better the performance of these and related materials to meet the most demanding requirements for applications in NC technologies. Theoretical investigations based on and extending from the current experimental data provide a means to bridge the gap in the current understanding of the atomic and electronic features of the structure that underpin performance in this case. While the nested type I bulk band alignment would suggest that InAs/InP/ZnSe NCs could give bright NIR emitters, strong quantum confinement of carriers in InAs and InP NCs complicates this oversimplified picture. To better understand the properties of these nanostructures, we performed atomistic electronic structure calculations on InAs/InP core/shell NCs of experimentally relevant sizes.

First, we developed a model within the semiempirical pseudopotential method that involved fitting pseudopotentials for In, As, and P that simultaneously reproduces accurate band structures for both bulk InAs and bulk InP [77, 229] using the process described in detail in Ch. 2.2. The band offsets between the constituent materials, which are of critical importance for studying core/shell systems, were set manually so that the valence band maximum of InP lies 0.42 eV below that of InAs [269, 270]. The sensitivity of the core/shell NC electronic structure to this parameter was also examined. The band offset value has an impact on the extent to which the valence band edge hole localizes to the InAs core, with a larger band offset increasing localization, but with no significant qualitative differences. To further validate this pseudopotential model, we performed calculations of the fundamental gaps of a series of zincblende InAs and InP NCs of different sizes and found excellent agreement with gaps calculated previously using the semiempirical pseudopotential method as well as those measured experimentally [77, 89, 229, 271, 272].

Core/shell NC configurations for InAs/InP NCs were obtained using the methods outlined in Ch. 2.2 The passivation pseudopotentials on the surface of the NC model the exterior ZnSe shell used as passivation layers experimentally. Exploration of defects at an InP/ZnSe interface from an incomplete ZnSe shell are modeled through the creation of phosphorus dangling bonds at the InP surface. Details of the nine NC structures studied here are col-

lected in Table 5.1. The quasiparticle and excitonic states were calculated *via* the procedures described in Ch. 2.2.

Table 5.1: Core/shell InAs/InP NC configurations.

Configuration	Core diameter (nm)	Shell thickness (nm)
$In_{555}As_{28}P_{504}$	1.5	1.1
$In_{1073}As_{28}P_{1056}$	1.5	1.6
$In_{1985}As_{28}P_{1976}$	1.6	2.2
$In_{1073}As_{152}P_{932}$	2.5	1.1
$In_{2081}As_{152}P_{1936}$	2.5	1.6
$In_{3319}As_{152}P_{3152}$	2.5	2.2
$In_{1421}As_{276}P_{1184}$	3.1	1.1
$In_{2391}As_{276}P_{2124}$	3.1	1.6
$In_{4045}As_{276}P_{3820}$	3.1	2.2

5.4 Investigating exciton delocalization into InP shell

The projected electron and hole carrier densities for the ground excitonic state of a 2.5 nm InAs NC with a 1.1 nm InP shell are depicted in Fig. 5.2a. Despite conventional wisdom that the type I band alignment of InAs/InP would confine carriers to the core, both the electron and hole are delocalized throughout the NCs with 53.8 and 26.5% of the electron and hole densities, respectively, in the shell [269]. Unsurprisingly, the electron is more delocalized than the hole due to its lighter effective mass. These results are indicative of InAs/InP nanostructures having a quasi-type II band structure as opposed to the type I band structure present in bulk materials [265]. Fig. 5.2b shows that carrier occupancy of the shell increases with both decreasing InAs core size and increasing InP shell thickness. This delocalization is attributed to the large exciton Bohr radii in InAs and InP, which are 34 and 15 nm, respectively, indicating that the carriers on the NCs are strongly quantum confined and thus have sufficient kinetic energies to tunnel through the confining potential created by the InAs/InP band offset and into the shell [273]. The electron-hole interactions are not strong enough to overcome the strong quantum confinement and localize the carriers to the InAs core.

Our calculations demonstrate that the electron in the ground state exciton tunnels isotropically into the shell. The hole, however, exhibits a facet-dependent delocalization into the InP shell through the (111) facets. Growth of an InP shell causes compression of the InAs core, as shown by molecular dynamics-based geometry optimization illustrated in Fig. 5.3, which causes the InAs valence band maximum (VBM) to decrease in energy. This VBM energy decrease has been shown to be a facet-dependent effect that locally decreases

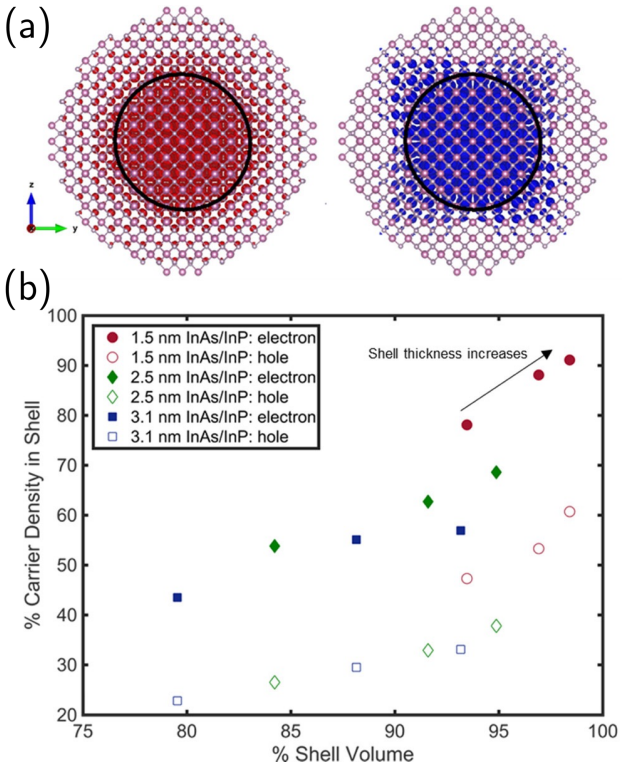

Figure 5.2: (a) Projected densities of the electron (red) and hole (blue) of the ground state exciton of an InAs/InP NC with a 2.5 nm diameter InAs core with a 1.1 nm InP shell. (b) As the relative shell volume of structures increases with thicker shells, the percentage of the carrier density in the shell increases for both electrons and holes.

the InAs/ InP valence band offset most significantly along the (111) facets, facilitating tunneling of the hole wavefunction in those directions [98, 270].

Comparing these observations with atomically resolved STEM images in Fig. 5.4, we have identified that the axes with a greater hole density correspond to directions of the narrowest radius in the synthesized NCs. Fig. 5.4a depicts the projected density of an excitonic hole from the (110) orientation. From this orientation, delocalization in the ⟨111⟩ directions to the surface is straightforwardly observed. The extent of charge carrier delocalization to the InP shell suggests that the InP shells do a poor job of confining charge carriers to the InAs core and indicates that the InP/ZnSe interface is particularly important for exciton confinement. An atomically resolved STEM image of an identically oriented NC (Fig. 5.4b) reveals that directions of hole delocalization align with directions of shorter radii in the slightly asymmetric, synthesized NCs. Fig. 5.4c depicts the projected excitonic hole density as viewed from the (111) orientation where tetrapodal, anisotropic delocalization into the shell is readily observed with a hole density from one of the [111] axes projecting perpendicular to the

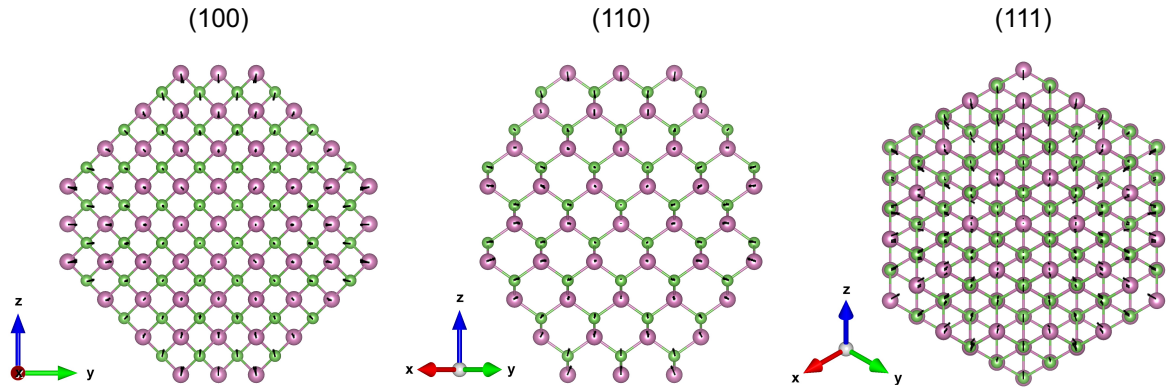

Figure 5.3: Molecular dynamics-based geometry optimization shows that growth of an InP shell on an InAs core, here a 1.1 nm InP shell on a 2.5 nm diamter InAs core, causes relatively isotropic compression of the InAs core. The black arrows indicate the magnitude and direction of each atom's displacment relative to the unstrained InAs core configuration.

plane of view. Fig. 5.4d shares the same (111) orientation, as is confirmed by the inset of the power function. The matched electronic structure calculations and atomically resolved STEM images highlight the importance of uniform InP and ZnSe passivation to insulate excitons and mitigate deleterious outcomes from holes delocalizing to passivated surfaces.

5.5 InP surface states quench luminescence

Due to delocalization of the ground state exciton out of the InAs core, defects at the InP/ZnSe interface may have a significant impact on the particle's optical properties. Prior work on highly emissive InP cores with ZnSe shells observed nonuniform shell growth caused by oxidation of surface indium and phosphorus to create $InPO_x$ and In_2O_3 defects during synthesis [274]. Oxidized phosphorus present at InP/ZnSe interfaces is known to form deep trap sites [275, 276].

To model defects at the InP surface, we perform calculations to obtain quasiparticle states of InAs/InP NCs with a passivation ligand pseudopotential removed from a single surface phosphorus atom, creating the equivalent of a phosphorus dangling bond [30]. We find that the unpassivated phosphorus atom creates a localized midgap quasiparticle state with an energy level between 200 and 500 meV above the quasiparticle VBM that depends on the specific location of the defect. Mid-gap states are not observed with the removal of a passivation ligand pseudopotential from an indium atom due to the relatively small electron effective mass. This finding is corroborated by the prior experimental work that has shown phosphorus dangling bonds formed through InP surface oxidation are responsible for deep trap states while unpassivated indium surface defects result in shallower mid-gap states [275,

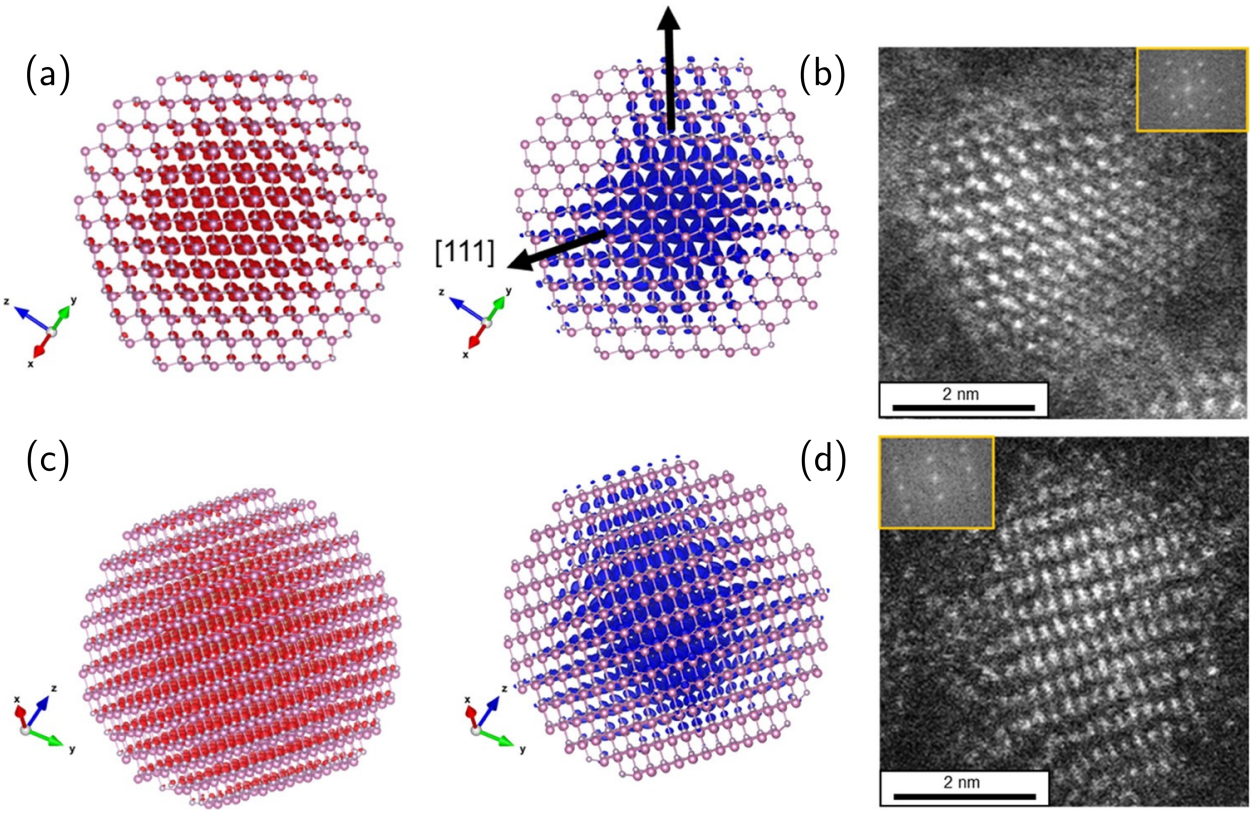

Figure 5.4: (a) Projected density of the exciton electron (red) and hole (blue) of an InAs/InP NC with a 2.5 nm core and 1.1 nm InP shell as viewed from the (110) orientation. (b) A similarly aligned atomically resolved TEM image of a single InAs/InP/ZnSe NC with a 2 nm scale bar and power function inset. (c) An alternate view of the electron (red) and hole (blue) densities displayed from the (111) orientation. (d) A similarly aligned atomically resolved TEM image of a single InAs/InP/ZnSe NC with a 2 nm scale bar and power function inset. Arrows indicating the [111] vectors are in plane with the projections.

276]. The directional delocalization of the VBM state extends far into the InP shell and has a density overlap with InP surface trap states on the (111) face. While the introduction of a phosphorus dangling bond does not change the energy of the VBM, significant trap-VBM density overlaps may promote phonon-mediated trapping of holes at the valence band edge, leading to quenching of luminescence.

As expected, we find that when the trap state is aligned with the lobes of the VBM density in the shell, the VBM has an increased localized density near the unpassivated phosphorus atom, as shown in the top of Fig. 5.5. Even with thin (1.1 nm) InP shells, there is almost no overlap between the trap state and the VBM when it is located away from the (111) facets. As the InP shell thickness increases, the hole density in the shell increases, but the

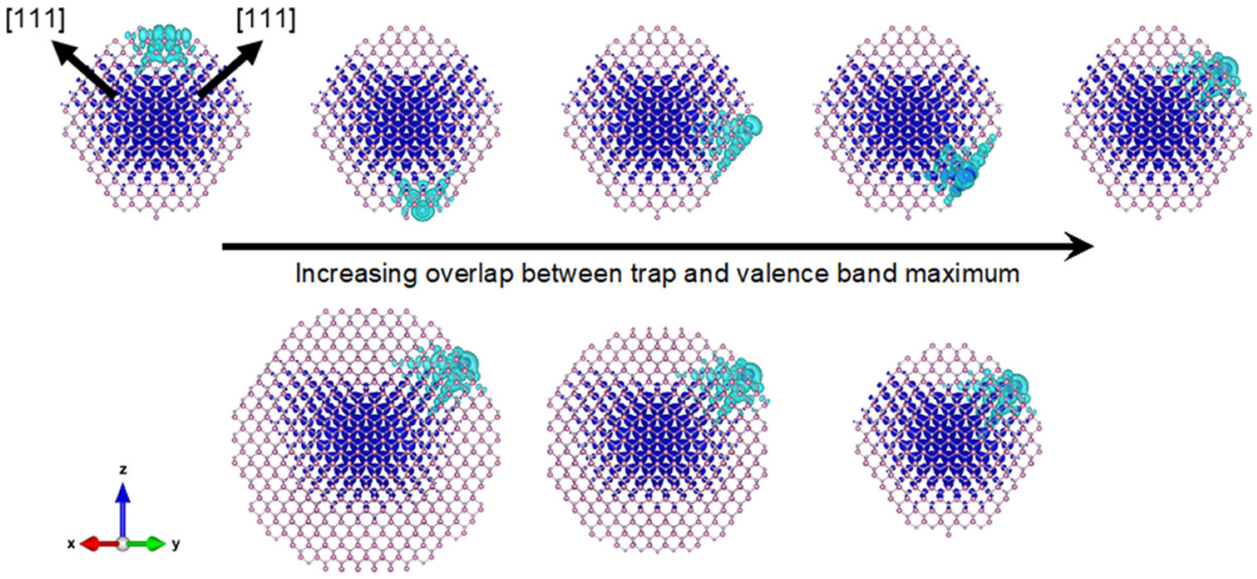

Figure 5.5: Trends of the density overlap between a surface defect state (cyan) and the single-particle valence band maximum state (blue) for defects located at the surface of InAs/InP NCs. The series on the top depicts a 2.5 nm InAs core and 1.1 nm InP shell NC with surface traps on different facets while the series on the bottom illustrates a 2.5 nm InAs core with InP shell thicknesses of 2.2, 1.6, and 1.1 nm. from left to right. Arrows indicating the [111] vectors are in plane with the projections.

density overlap between the defect state and the VBM decreases (bottom of Fig. 5.5). Across all InP thicknesses, defects located directly along the (111) axis present the greatest defect site-VBM overlap. To quantify the effect of the dangling bond on the VBM, we computed the overlap between the single-particle densities, $|\phi(\boldsymbol{r})|^2$, of the localized trap and the VBM:

$$\int_{-\infty}^{\infty} d\boldsymbol{r} \sqrt{|\phi_{\mathrm{VBM}}(\boldsymbol{r})|^2 |\phi_{\mathrm{trap}}(\boldsymbol{r})|^2}\,. \tag{5.1}$$

These values, as well as the trap state locations and energy levels, are collected in Table 5.2 and demonstrate that a dangling bond on the InP shell at the (111) surface can create a localized trap state that has a relatively large density overlap with the VBM, facilitating trapping of carriers to the surface and thereby decreasing PLQY. Thus, it is important to continue to improve development of particles with thick, uniform, protective ZnSe shells to prevent InP surface defects from quenching NC luminescence.

Table 5.2: Facet-dependent trap state energies and density overlaps with the VBM state. The structures here correspond to those illustrated in Fig. 5.5.

Nanocrystal	Trap facet	Energy above VBM (meV)	Overlap
2.5 nm InAs – 1.1 nm InP	$(\bar{1}11)$	218	0.231
2.5 nm InAs – 1.6 nm InP	$(\bar{1}11)$	227	0.147
2.5 nm InAs – 2.2 nm InP	$(\bar{1}11)$	210	0.129
2.5 nm InAs – 1.1 nm InP	$(01\bar{1})$	670	0.190
2.5 nm InAs – 1.1 nm InP	$(\bar{1}10)$	287	0.125
2.5 nm InAs – 1.1 nm InP	$(00\bar{1})$	455	0.034
2.5 nm InAs – 1.1 nm InP	(001)	455	0.034

5.6 Understanding trends in radiative lifetimes

Based on the decreased overlap between surface defects and the VBM with increased InP shell thickness, we compare the exciton lifetimes between InAs/InP/ZnSe NCs with different InP thicknesses. The PLQY for thick InP (1.5±0.1 nm)-shelled InAs/InP/ZnSe NCs can be improved from 1 to 51±3% by better passivating the surface with more uniform and thicker (3 monolayer) ZnSe shells. We compare a pair of NCs with nearly identical InAs cores and ZnSe shells but with 1.0±0.1 and 1.5±0.1 nm thick InP shells. The PLQY for the compared samples are 55±2 and 51±3%, respectively, enabling a more direct probe of the radiative lifetimes across the InP shell thickness since the NCs share similarly bright emission. Generally, there is a correlation between higher quality, defect-free materials with higher PLQY and longer radiative lifetimes. Thus, reduction of the overlap between surface defects and the VBM from thicker InP shells may be expected to reduce surface hole trapping and extend exciton lifetimes. However, as shown in Fig. 5.6a, we observe the exciton decay times to be 17.1±0.1 and 11±1 ns, respectively, for the 1.0±0.1 and 1.5±0.1 nm thick InP-shelled NCs, indicating that exciton lifetimes decrease with increased InP shell thickness.

Despite the expected decreased exciton trapping in the thicker-shelled InP NCs, the decreasing trend between the lifetime and shell thickness is attributed to the fact that the radiative lifetime, τ_{r}, depends on both the energy, ω, and the dipole moment, μ, of the transition according to:

$$\tau_{\mathrm{r}} = \frac{3\pi\varepsilon_0\hbar c^3}{\omega^3|\mu|^2}\,. \tag{5.2}$$

The optical gaps of InAs/InP/ZnSe NCs depend on both the core size and shell thickness, and they decrease with both increasing InAs core diameter and InP shell thickness. While the size of the core is the primary component of the NC that dictates the optical gap, the InP shell thickness also plays a notable role. Prior work suggests a decrease in the fundamental gap between bare 3.4 nm InAs and the same NCs with 2 nm InP shells of up to 200 meV [89]. This is corroborated by both our experimental work and calculations, as illustrated in Fig. 5.7. On the other hand, the transition dipole moment of the ground state exciton increases with increasing InAs and InP sizes, a trend that has been previously

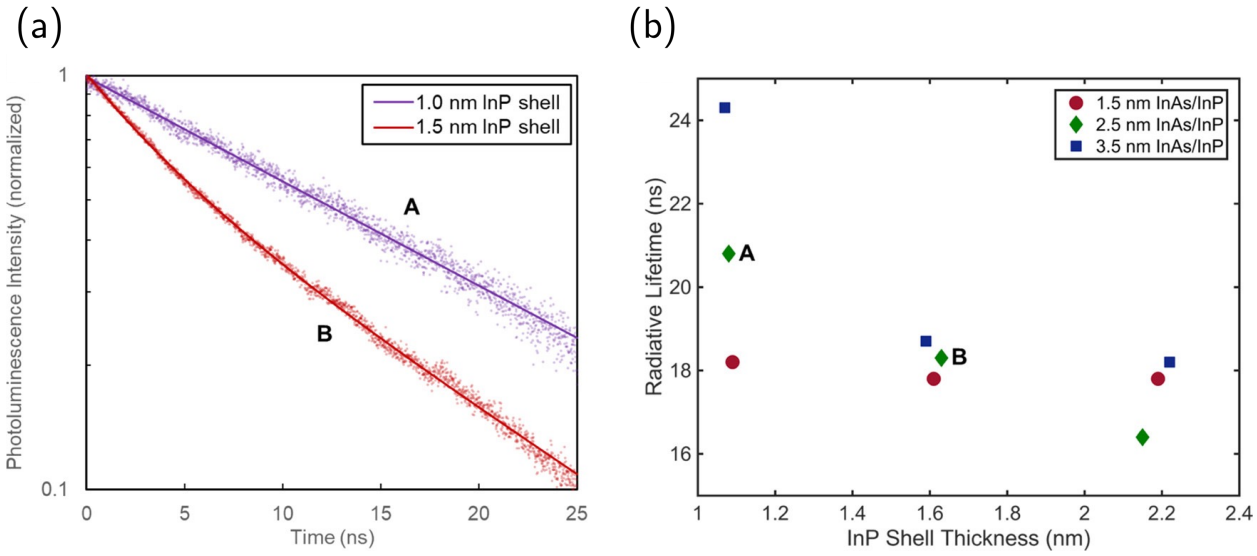

Figure 5.6: Exciton decay lifetimes of InAs/InP/ZnSe NCs. (a) Photoluminescence decay curves of the InAs/InP/ZnSe NCs with 2.7±0.2 nm InAs cores and 1.0±0.1 nm (violet) or 1.5±0.1 nm (red) thick InP shells with 3 monolayer thick ZnSe shells fitted with monoexponential decays. (b) Calculated radiative lifetimes for InAs/InP NCs across a spectrum of InAs core sizes and InP shell thicknesses. The InAs core and InP shell sizes of the NCs annotated A and B in panels (a) and (b) share similar sizes and highlight the decreasing trend between the radiative lifetime and shell thickness.

observed in other CdSe and InAs NC systems [277–279]. Together, the radiative lifetime depends inversely on the square of the transition dipole moment and inversely to the cube of the transition energy. Therefore, the radiative lifetime could increase or decrease with increasing shell thickness, depending on the rate of change of these properties with shell thickness for the specific material. As illustrated in Fig. 5.7, the transition energy weakly decreases with increasing InP shell thickness while the transition dipole moment increases significantly with increasing InP shell thickness, causing the radiative lifetime to decrease with increasing InP shell thickness. Fig. 5.6b depicts the combined effects of a decreasing optical gap and increasing dipole moment across particle sizes and shows the radiative lifetimes decrease with increasing InP shell thickness. Therefore, even though there may be reduced exciton trapping in thicker-shelled InP systems, suggesting improved surface passivation, the radiative lifetimes for excitons in InAs/InP/ZnSe NCs still decreases with thicker InP shells.

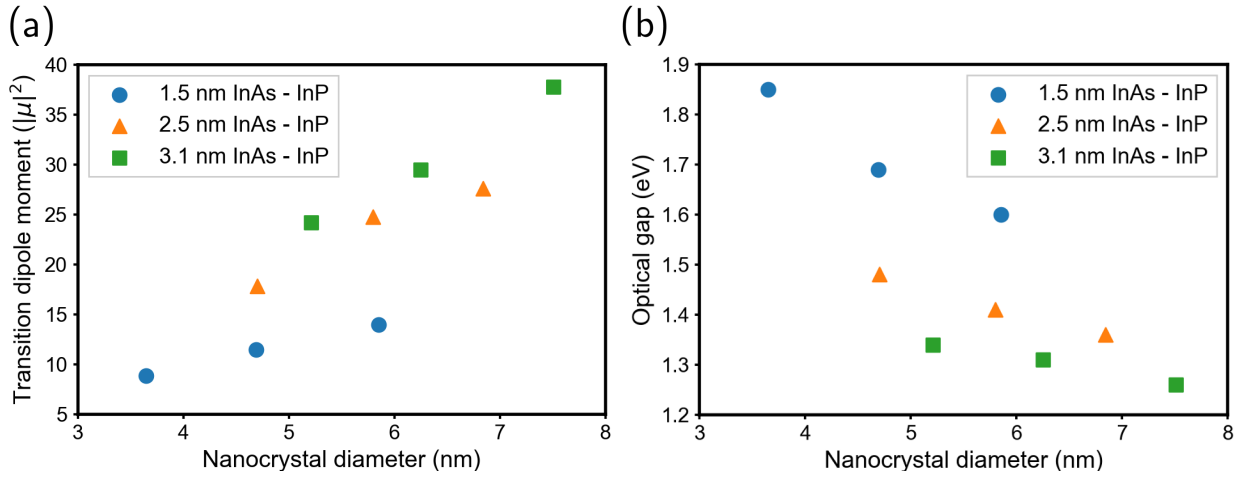

Figure 5.7: The (a) optical gaps and (b) transition dipole moments of InAs/InP NCs. The transition dipole moments increase with increasing core size and shell thickness while the optical gaps decrease with increasing core size and shell thickness.

5.7 Conclusions

InAs core/multishell NCs offer exceptional promise for myriad applications due to opportunities to tune the Stokes ratio and improve PLQY while retaining narrow emission. However, the current assessment of exciton lifetimes highlights the challenges in the development of highly luminescent InAs/InP/ZnSe NCs, especially if phosphorus dangling bonds are unavoidable. On one hand, it is important to increase the thickness of the InP shell to decrease hole trapping. On the other hand, charge carriers delocalize to the shell more readily in systems with thicker InP shells, leading to greater opportunities for nonradiative losses as luminescence is highly sensitive to InP surface/interfacial defects. Thus, improvements to NIR emissive InAs/InP/ZnSe necessitate the highest quality and uniform ZnSe shell encapsulation for thick-shelled InP NCs. While this is challenged synthetically due to the slightly anisotropic InAs/InP structure, the synthetic procedures adopted here have proven to be adaptable to independent size modulation of the core and both shells to facilitate growth of several monolayer thick passivating ZnSe layers on large Stokes ratio particles (*i.e.*, thick InP layers) to enhance luminescence. Growth of extremely thick ZnSe shells (>5 monolayers) in these systems, however, remains an unresolved synthetic challenge needing redress in future research. The scale of the challenge is well suggested by the past work. Near-unity CdSe/CdS NCs, for example, were prepared with 8-monolayer thick CdS shells [68], suggesting that further material development to obtain thicker, uniform ZnSe shells may yield enhancements of emission and stability for the InAs/InP/ZnSe system as well.

In this chapter, we demonstrated improvements for the synthesis of InAs/InP/ZnSe NCs that enable heavy metal-free, tunable, NIR emitters with 60±2% PLQY. While the NIR

emitters reported here are among the brightest, cadmium-free InAs emitters with larger Stokes ratios, there are still synthetic and material challenges that must be addressed to realize applications, such as high-performance luminescenct solar concentrators and other NIR technologies. A primary reason for this challenge is attributed to the significant charge carrier occupation of the InP shell due to the strong quantum confinement of carriers in these structures, complicating the type I bulk alignment expected from bulk band gaps. Furthermore, defects at the InP/ZnSe interface, especially along the (111) facets, and unpassivated phosphorus dangling bonds lead to localized, deep trap states that have large density overlaps with the NC valence band maximum. These defects facilitate carrier trapping and decrease PLQY. Luminescence in InAs/InP/ZnSe is extremely sensitive to the quality of surface passivation. While our synthetic approach enables >50% PLQY NIR emitters, there remain opportunities for further development of InAs heterostructure NC systems to maximize their utility and realize new technologies.

Chapter 6

Uncovering the role of hole traps in promoting hole transfer from multiexcitonic nanocrystals to molecular acceptors

Localized trap states, resulting from structural defects, especially those at surfaces and interfaces, are ubiquitous in experimental nanocrystal (NC) systems and can have serious deleterious effects on NC performance, as discussed in Chs. 4 and 5. Thus, understanding the populations and dynamics of these trap states is key to developing NC systems that mitigate the negative impacts of traps or utilize traps to enhance certain properties. Transient absorption (TA) spectroscopy is an experimental technique widely used to study the dynamics of various processes, such as trapping, nonradiative decay, or transferring of photoexcited carriers in NCs. TA spectra of these systems show broad, photoinduced absorption (PA) features that appear lower in energy than those of the band edge, which have been assigned to the PA of holes populating NC surface traps. While there has been experimental justification of this assignment, there has been little theoretical investigation. In this chapter, we use atomistic electronic structure calculations of CdSe NCs to characterize PA signals by computing oscillator strengths for sub-bandgap transitions of conduction band electrons, valence band holes, and surface-trapped holes. We find that, in the region of interest from 1.45 to 1.9 eV, oscillator strengths for transitions of trapped holes are significantly larger than those of electrons or valence band holes. We conclude that the low symmetry of localized surface trap states and optimal spatial overlap with highly oscillatory states deep in the valence band lead to large electric dipole matrix elements and increased oscillator strengths. Our results are consistent for CdSe and CdS cores, CdSe/CdS core/shell quantum dots, and CdSe nanorods.

After confirmation of this spectroscopic assignment, we use TA to study hole transfer from NCs excited under multiexcitonic regimes to a hole accepting ligand. In this regime, the multiple charge carriers within a NC can undergo undesired Auger recombination (AR)

events, which rapidly annihilate carriers on picosecond time scales and generate heat from absorbed photons instead of useful work. To probe the competition between AR and hole transfer in CdSe, CdS, and CdSe/CdS core/shell NCs of varying sizes, we use TA to monitor the PA features from both trapped holes and oxidized ligands under excitation fluences where the averaged initial number of excitons in a NC ranged from ∼1 to 19. We observe fluence-dependent hole transfer kinetics that last around 100 ps longer than the predicted Auger recombination lifetimes, and the transfer of up to 3 holes per NC. Theoretical modeling of the kinetics suggests that binding of hole acceptors introduces trapping states significantly different from those in native NCs passivated with oleate ligands. Calculations demonstrate that the AR lifetimes from initial states involving holes in these modified trap states are prolonged, which promotes the hole transfer efficiency. These results highlight the beneficial role of hole trapping states in devising hole transfer pathways in NC-based systems under multiexcitonic conditions. The content of this chapter is adopted with permission from Jasrasaria, D.; Philbin, J. P.; Yan, C.; Weinberg, D.; Alivisatos, A. P.; Rabani, E. Subbandgap photoinduced transient absorption features in CdSe nanostructures: The role of trapped holes. *J. Phys. Chem. C* **2020**, *124*, 17372 and Yan, C.; Weinberg, D.; Jasrasaria, D.; *et al.* Uncovering the role of hole traps in promoting hole transfer from multi-excitonic quantum dots to molecular acceptors. *ACS Nano* **2021**, *15*, 2281.

6.1 Introduction

Colloidal semiconductor nanocrystals (NCs) have many attractive properties, such as tunable band gaps, high photoluminescence quantum yields, and the ability to generate multiple charge carriers, that make them promising materials for solar harvesting applications [280–282], photocatalysis [283, 284], and other optoelectronic devices [68, 280, 285, 286]. Realization of these applications requires a better understanding of the dynamics of photoexcited charge separation and transfer in NCs. Many experimental studies employ ultrafast transient absorption (TA) spectroscopy as a time-resolved method to study charge carrier dynamics. In TA, a pump pulse at a certain energy and fluence generates an initial number of electron-hole pairs *via* optical excitation. After a time delay, a probe pulse is sent through the sample, and the ground state absorption spectrum is subtracted from the excited state absorption. This differential absorbance, ΔA, can be measured as a function of both the probe energy and the pump-probe time delay to understand the dynamics of different populations. Negative ΔA features are due to ground state bleaching, when ground state carriers have been depleted to excited states, or stimulated emission. Positive ΔA features are due to excited state absorption or product absorption.

Understanding chemical processes and kinetics through TA relies on the accurate assignment of differential absorbance features. The study of charge separation and transfer requires monitoring the populations of individual charge carriers, which can be difficult because the optical pump pulse always creates neutral excitations (*i.e.*, electron-hole pairs). Monitoring the population of excited electrons is possible through analysis of the conduction

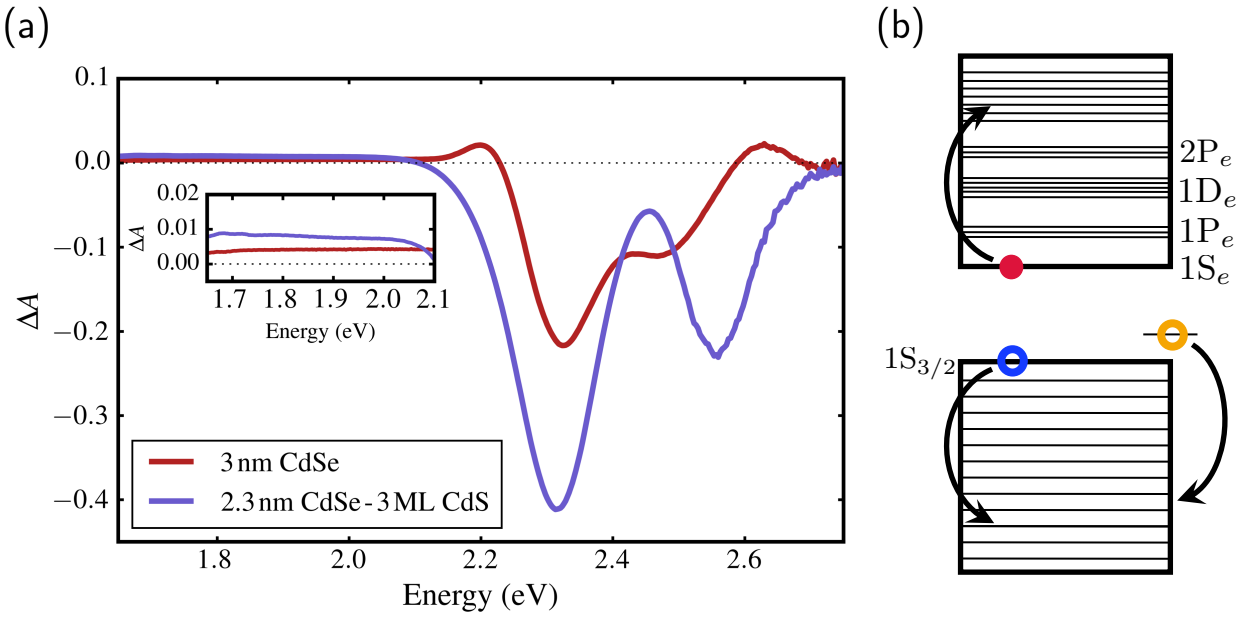

Figure 6.1: (a) Experimental TA spectra of a 3.0 nm CdSe core (maroon) with a 540 nm excitation wavelength and 7.0 ns pump–probe delay and 2.3 nm CdSe/3 monolayer CdS core/shell (purple) with a 545 nm excitation and 7.0 ns delay. The inset illustrates the broad, positive PA feature. (b) Energy level schematic of a CdSe core showing single-particle states. PA could be attributed to sub-bandgap transitions from the (i) conduction band edge (red), (ii) valence band edge (blue), or (iii) surface trap states (orange).

band bleach, which is one of the dominant features in TA spectra of NCs (Fig. 6.1a) and is caused by state filling of the $1S_e$ state with electrons upon photoexcitation from the pump pulse [56, 287, 288]. The intensity of this signal only reflects the population of electrons in the $1S_e$ state, however, and does not provide information about hole populations because of the high degeneracy of the valence band. This high density of valence band states generally makes tracking hole populations more difficult.

To address this challenge, many studies investigating charge separation and transfer in NCs use differential absorbance features that are lower in energy (higher in wavelength) than the band gap to monitor populations of individual carriers. At these lower energies, the probe does not have enough energy to create additional excitons *via* optical excitation across the band gap. Instead, these energies are probing sub-bandgap photoinduced absorption (PA) transitions of photogenerated electrons or holes to further in the conduction and valence bands, respectively [64, 287, 289–291]. These PA features always have positive differential absorbance, but they are much smaller in amplitude than the conduction band bleach and

often broad; therefore, attributing these signals to specific transitions or populations can be difficult.

Furthermore, because these sub-bandgap PA transitions are so low in energy, they often require probe energies in the infrared (IR) or near-IR (NIR) spectra. A sharper PA peak has been observed in the IR spectrum around 0.26 eV (4600 nm) in 4.5 nm CdSe NCs [292, 293], and broad features have been measured in the near-IR spectrum around 0.62-1.1 eV (2000-1100 nm) in CdSe [40, 42, 292, 293] and CdS NCs [294]. These features have been attributed to intraband transitions of band edge electrons and holes, respectively.

With probes in the visible region, several experiments have observed a broad, positive PA feature that appears at 1.45-1.9 eV (850-650 nm) in CdSe [295] and CdS [294, 296, 297] NCs, CdSe/CdS core/shell NCs [298], and CdS nanorods [298, 299]. These works attribute this broad feature to the PA of holes trapped at surface states of the NC. They observe a more rapid decay of this PA signal in the presence of a hole-accepting ligand phenothiazine (PTZ) [295] and no change in kinetics in the presence of an electron-accepting ligand benzoquinone (BQ) [295, 298, 300], suggesting this feature is associated with holes, not electrons. Additionally, they find that the rise time of this feature is slower than $\sim$200 fs, which is slower than expected cooling rates [295], and the decay kinetics match those of trap emission bands in photoluminescence spectroscopy [299], indicating the feature can be attributed specifically to trapped holes. While similar types of features have been studied computationally in small semiconducting clusters [301], this broad feature in NCs has not been assigned by first-principle or model calculations, and the origin of these photoinduced transitions, especially in the visible region, is not well understood.

Fig. 6.1a shows the TA spectra of 3.0 nm CdSe and 2.3 nm CdSe/3 monolayer CdS core/shell NCs with band edge excitations at a high fluence, for which an average of two excitons are created upon excitation. At the illustrated pump-probe delay of 7 ns, the average number of excitons remaining is less than one. Both spectra feature the large, negative conduction band bleach as well as the broad, positive PA feature from 1.65 to 2.05 eV, which is highlighted in the inset. This experimental data is representative of previously reported observations of broad, positive features in the visible region of TA studies of similar systems [294–299]. PA features can generally be attributed to the photoinduced absorption of (i) band edge electrons to higher in the conduction band, (ii) band edge holes to deeper in the valence band, and (iii) surface-trapped holes to the valence band, as illustrated in the model energy diagram in Fig. 6.1b.

Here, we perform atomistic calculations on CdSe and CdS NCs of experimentally relevant sizes to compute the oscillator strengths (OSs) of transitions from each of these three states, thereby investigating the energies and relative amplitudes of PA features, with a focus on those in the 1.45-1.9 eV (850-650 nm) region, in these systems. We find that sharper features in the IR region are due to the $1S_e$-$1P_e$ transition of conduction band edge electrons, and broad features in the NIR are dominated by PA of valence band holes; broad features in the 1.45-1.9 eV region are due to PA of surface-trapped holes.

6.2 Atomistic calculations of photoinduced absorption signals

We perform atomistic electronic structure calculations within the semiempirical pseudopotential method [10, 26, 27, 77] to obtain quasiparticle states of CdSe, CdS, and CdSe/CdS core/shell NCs as well as CdSe nanorods. Note that, while the discussion throughout the paper uses notation of the effective mass model to describe single-particle states (*i.e.*, $1S_e$, $1P_e$, etc.), these calculations have been performed within an atomistic approach.

NC configurations for CdSe, CdS, and CdSe/CdS nanostructures were obtained *via* the procedure described in Ch. 2.2. Hole trap states were modeled by the removal of a passivation ligand from a chalcogenide atom on the surface, which creates a localized trap state about 500-750 meV above the valence band maximum. Details of the NC configurations studied here are collected in Table 6.1.

Table 6.1: CdSe and CdS NC configurations. Cores are referenced by diameter, and nanorods are referenced by their diameter and length, respectively.

Nanocrystal	Configuration
2.5 nm CdSe	$Cd_{157}Se_{150}$
3.3 nm CdSe	$Cd_{355}Se_{338}$
4.0 nm CdSe	$Cd_{618}Se_{620}$
5.0 nm CdS	$Cd_{1292}S_{1267}$
2.3 nm CdSe / 3 monolayer CdS	$Cd_{525}Se_{132}S_{419}$
2.0 nm-10.0 nm CdSe	$Cd_{681}Se_{681}$

Experimentally, midgap hole trap states arise from unpassivated chalcogenide atoms on the surface of the NC. Within the semiempirical pseudopotential method, all surface Cd, Se, and S atoms are generally modeled with passivation ligand pseudopotentials, which push the energy of surface states out of the band gap. Therefore, a surface hole trap is modeled by a Se or S atom that is unpassivated [29, 229], which creates a localized midgap state about 0.5 eV above the valence band maximum. These energies are consistent with electron microscopy, absorption, and emission measurements on CdSe and CdS NCs, which have shown that dangling Se and S bonds create surface traps with similar energies [91, 302, 303].

Electron trap states are less common, both in theoretical models and in experimental systems, than midgap hole trap states in CdSe and CdS systems [67, 304]. Electrons have a relatively small effective mass (about 5 times smaller than holes in CdSe and CdS), so they are unlikely to form localized, midgap trap states, even when Cd atoms are left unpassivated.

To understand the origin of the PA signal in these systems, we compute the oscillator strengths (OSs) of intraband transitions from the conduction band edge, valence band edge,

and hole trap states. For a transition from state i to state j, the OS is calculated as

$$f_{ij} = \frac{4m_e}{3\hbar^2 e^2}(\varepsilon_j - \varepsilon_j)|\boldsymbol{\mu}_{ij}|^2\,, \tag{6.1}$$

where m_e is the mass of the electron, e is the charge of the electron, and $\boldsymbol{\mu}_{ij}$ is the electric dipole matrix element given by

$$\boldsymbol{\mu}_{ij} = e\int d\boldsymbol{r}\phi_i(\boldsymbol{r})\,\boldsymbol{r}\,\phi_j(\boldsymbol{r})\,, \tag{6.2}$$

where $\phi_i(\boldsymbol{r})$ is the single-particle (*i.e.*, electron or hole) wavefunction for state i with energy ε_i. The absorption cross section, σ, reflects the probability of absorption of each transition from a given state as well as the number of possible transitions [183]. It can be obtained as a function of the transition energy, ω, by performing a Boltzmann-weighted average over initial states i and summing over all possible transitions j:

$$\sigma_i(\omega) \propto \frac{1}{Z\sqrt{2\pi\gamma^2}}\sum_i e^{-\beta\varepsilon_i}\sum_j f_{ij}\exp\left[-\frac{1}{2}\left(\frac{\omega-(\varepsilon_j-\varepsilon_i)}{\gamma}\right)\right]. \tag{6.3}$$

Here, $\gamma = 0.042\,\text{eV}$ is the inhomogeneous broadening factor, and $Z = \sum_i e^{-\beta\varepsilon_i}$ is the partition function of initial states. $\beta = 1/k_BT$ at room temperature, 298 K. Only the partition function for the valence band edge has contributions from multiple states, as the spectrum of hole states is relatively dense, even near the band edge.

6.3 Energy scales and characteristics of photoinduced absorption signals

PA features were investigated in CdSe cores with a diameter of 4.0 nm as a representative system, because their PA features have been well characterized; they are often used in experimental studies of charge separation and transfer. The charge densities of the conduction band edge electron, valence band edge hole, and surface-trapped hole are illustrated in Fig. 6.2a, and the absorption cross sections with transition energies for each of these states are shown in Fig. 6.2b. Near-band-edge transitions are the most significant for the PA signal from the conduction band edge. In particular, the $1S_e$-$1P_e$ transition at 0.27 eV (4600 nm), which corresponds to the 0.26 eV IR feature observed and characterized for 4.5 nm CdSe cores [293], appears as a sharp peak with a very high amplitude. The $1S_e$-$2P_e$ transition is higher in energy (1.1 eV) and in agreement with calculations for CdSe cores of a similar size [17, 19, 305].

These conduction band PA features are sharp, reflecting the density of states near the conduction band edge, which is sparse due to quantum confinement and the relatively small electron effective mass. The energies of these sharp transitions are size dependent. Specifically, they will be higher in energy for smaller structures, in which the confinement energy is

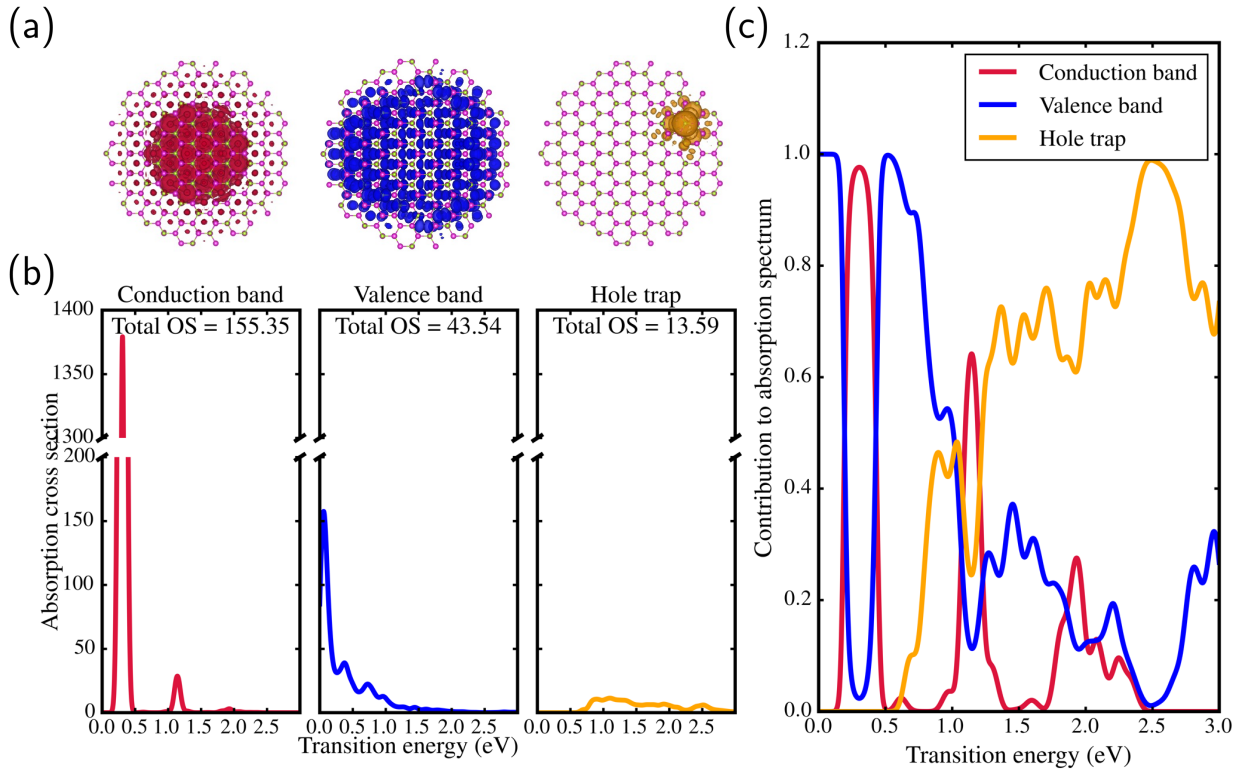

Figure 6.2: (a) Charge carrier densities for the conduction band edge (red), valence band edge (blue), and hole trap (orange) of a 4.0 nm CdSe core. (b) Absorption cross sections in arbitrary units for intraband transitions from each of these states. The total OS is the absorption cross section integrated over the transition energy range from 0 to 3 eV. (c) The contribution of each state to the total intraband absorption spectrum. The conduction and valence band edges dominate the PA spectrum for transition energies less than 1.4 eV while the hole trap state dominates for transition energies larger than 1.5 eV.

larger and the energy spacing between conduction band states is larger. Additionally, while transitions with changes in orbital angular momentum beyond ± 1 are allowed outside of the effective mass approximation, due to the breaking of spherical symmetry, they are still weak and have a negligible contribution to the PA. Because of the relatively large $1S_e$-$1P_e$ splitting, the TA pump creates electrons that populate only the $1S_e$ state, and the only significant PA signals are those corresponding to $1S_e$-nP_e transitions. At very high fluences, where the pump creates more than two excitons and the $1P_e$ state is also populated, additional features corresponding to $1S_e$-nD_e transitions are expected to appear.

Transitions near the band edge are also the most prominent features of the PA signal of the valence band edge. These features begin to appear at very low energies (0.01-0.5 eV),

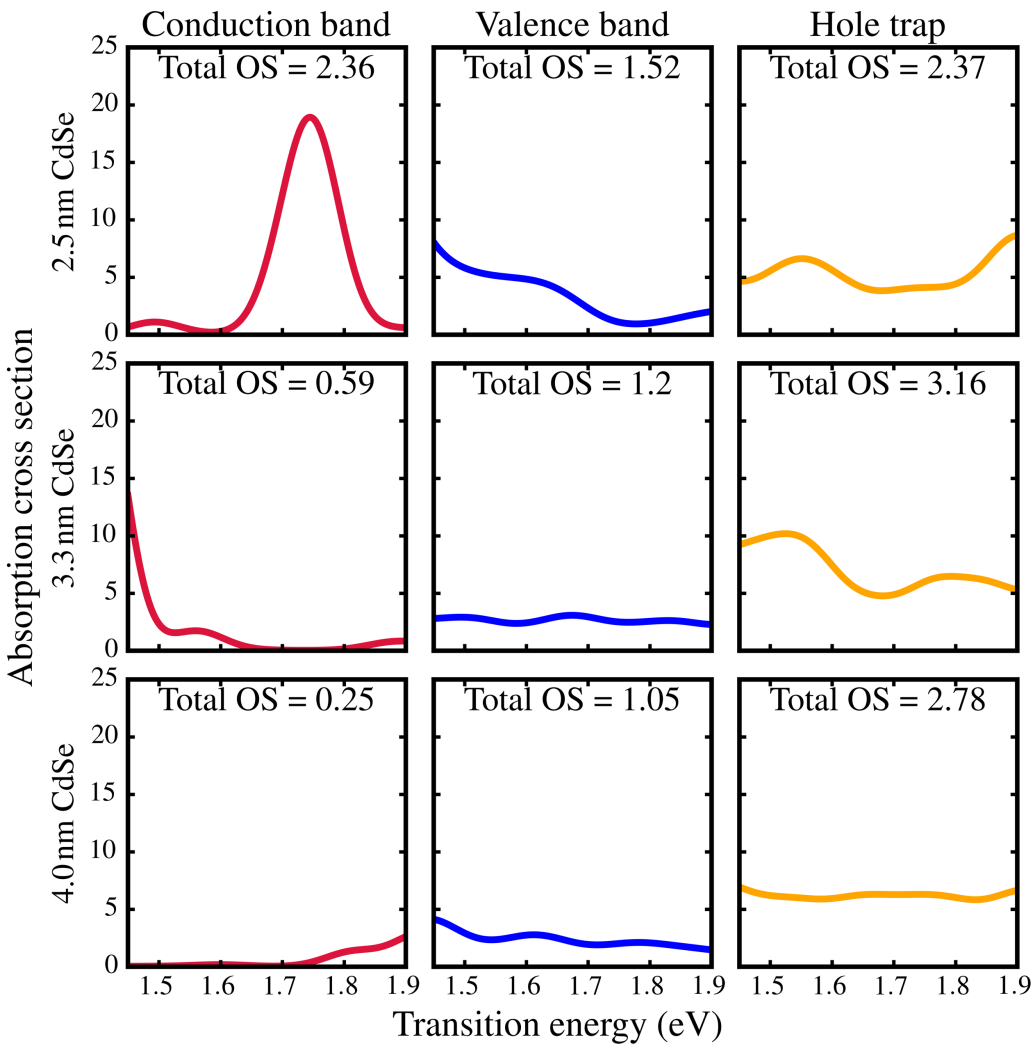

Figure 6.3: Absorption cross section in arbitrary units in the energy region of interest (1.45–1.9 eV, 850–650 nm) for CdSe cores with diameters of 2.5 (top), 3.3 (center), and 4.0 (bottom) nm. The smallest core has a peak corresponding to the $1S_e$–$2P_e$ transition. For the larger systems, these peaks are lower in energy due to smaller confinement energies. For all systems, the hole trap has the largest absorption cross section. This effect becomes more pronounced as the size of the system increases. The total OS is integrated over the transition energy range from 1.45 to 1.9 eV.

as the valence band is more dense near the band edge due to a larger effective mass and 2-fold degeneracy. Because of this high density of states, the TA pump creates holes not necessarily at the valence band maximum ($1S_{3/2}$ state) but at any of these near-band-edge

states, according to a Boltzmann probability, as shown in Eq. (6.3). Consequently, many transitions at a variety of energies satisfy a change in orbital angular momentum equal to ± 1 and therefore have a larger OS, resulting in broad and relatively size-independent PA features for the valence band hole.

The surface-trapped hole has a negligible absorption cross section for all transition energies less than 0.75 eV. This is because, while the hole-trapped state is localized to the surface, hole states near the valence band edge have the largest wave function amplitudes near the center of the NC, as shown in Fig. 6.2b. While the OSs for transitions from the trapped hole state remain small, they persist for higher-energy transitions, unlike those of the conduction and valence bands.

The absorption cross sections vary significantly over the full energy range 0.0-3.0 eV, but the PA from each state dominates the overall PA signal at different energy regimes (Fig. 6.2c). At the lowest energies (0.0-0.25 eV, greater than 5000 nm), valence band holes dominate the PA. In the IR region, the $1S_e$-$1P_e$ transition is dominant around 0.27 eV (4600 nm). At higher energies (0.5-1.0 eV, 2500-1250 nm), the valence band hole again has the largest contribution to the overall PA spectrum, corresponding to the broad feature around 0.7 eV observed in 4.0 nm CdSe and CdS cores [40, 294]. At energies higher than 1.5 eV (wavelengths shorter than 830 nm), trapped holes dominate the overall PA signal.

To better understand the PA signal due to trapped holes and its dependence on system size, we computed the absorption cross section for CdSe cores of different diameters, 2.5, 3.3, and 4.0 nm, and focused on the energy range of interest (1.45-1.9 eV, 850-650 nm). As depicted in Fig. 6.3, the trapped hole absorption cross section comprises a broad feature that is larger in amplitude than that of band edge electrons and holes. This phenomenon persists for CdSe cores of different diameters, 2.5, 3.3, and 4.0 nm, but is more obvious for larger cores.

This trend can be explained by the decreased confinement energy in larger systems, which causes the momentum of the excited electron or hole to increase with increasing NC size for a given excitation energy. These higher-momentum states have a significant amplitude throughout the NC, while lower-momentum states have a larger amplitude concentrated in the center and fewer nodes, as illustrated in Fig. 6.4. Therefore, the magnitude of the electric dipole matrix element, given by Eq. (6.2), is larger between the higher-momentum states in larger cores and surface trap states that are highly localized to the surface. Aside from contributions of the hole to the PA signal, the smallest core includes a sharper feature in this energy region due to the $1S_e$-$2P_e$ transition, which is not present in larger structures due to decreased quantum confinement and a lower-energy spacing between the $1S_e$ and $2P_e$ states (Fig. 6.3).

Finally, we performed calculations on a 5 nm CdS core, 2.3 nm CdSe/3 monolayer CdS core/shell NC, and 2.1 nm diameter-10 nm length CdSe nanorod, as these systems have been studied in the context of charge transfer as promising candidates for solar energy harvesting and other applications. Fig. 6.5 indicates that the PA signal in the region from 1.45 to 1.9 eV is again dominated by surface-trapped holes in these systems. In fact, the dominance of the trapped hole signal over the valence band signal is even more pronounced than those in the

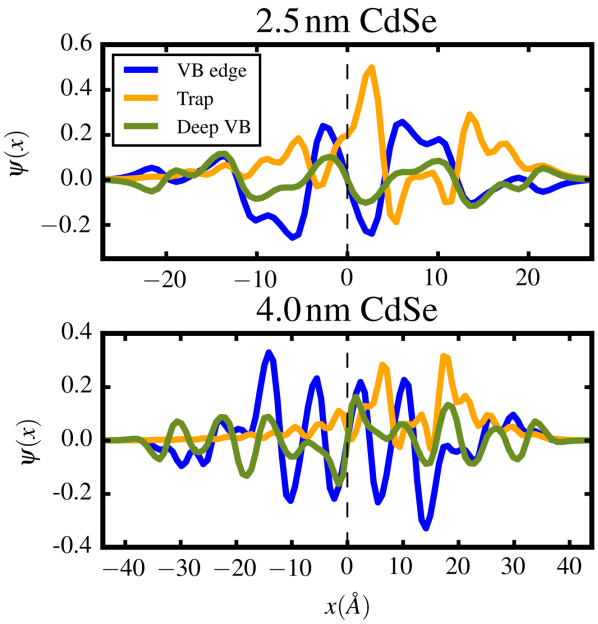

Figure 6.4: Projections of single-particle wave functions onto the x-axis of the valence band edge (blue), surface hole trap (orange), and a state 1.7 eV below the valence band maximum (green) in a 2.5 nm CdSe core (top) and 4.0 nm CdSe core (bottom). The deep valence band state is higher in momentum and more oscillatory in the 4.0 nm CdSe core due to a lower confinement energy. Also, note that, for both systems, the valence band states have inversion symmetry about $x = 0$, while the surface trap state does not have the symmetry.

CdSe cores shown above. This is again due to the fact that all these structures are even larger than the 4 nm CdSe core, so higher-energy states are more oscillatory with a significant amplitude throughout the NC. Interestingly, the dominance of the trapped hole contribution to the PA signal in the region from 1.45 to 1.95 eV is independent of the location of the surface trap, even for the highly anisotropic nanorods (Fig. 6.6). This effect can again be explained by the increased amplitude of higher-energy valence band states near the surface of the nanorods, where the surface trap states are localized.

Our results show that for transition energies greater than 1.45 eV in a variety of systems, the photoinduced absorption cross section of trapped holes is much larger than those of band edge electrons or holes. Deeper into the conduction and valence band are higher-momentum states that have more oscillatory wave function envelopes with relatively equal amplitudes throughout the NC. Band edge electrons and holes, however, have radially symmetric wave function envelopes that have a higher amplitude at the center. Surface-trapped holes break radial symmetry and have a larger amplitude in a more localized area of space, as depicted in Fig. 6.4. Therefore, the integral for the electric dipole matrix element has a larger value for transitions between the symmetric high-energy valence band states and the localized trapped

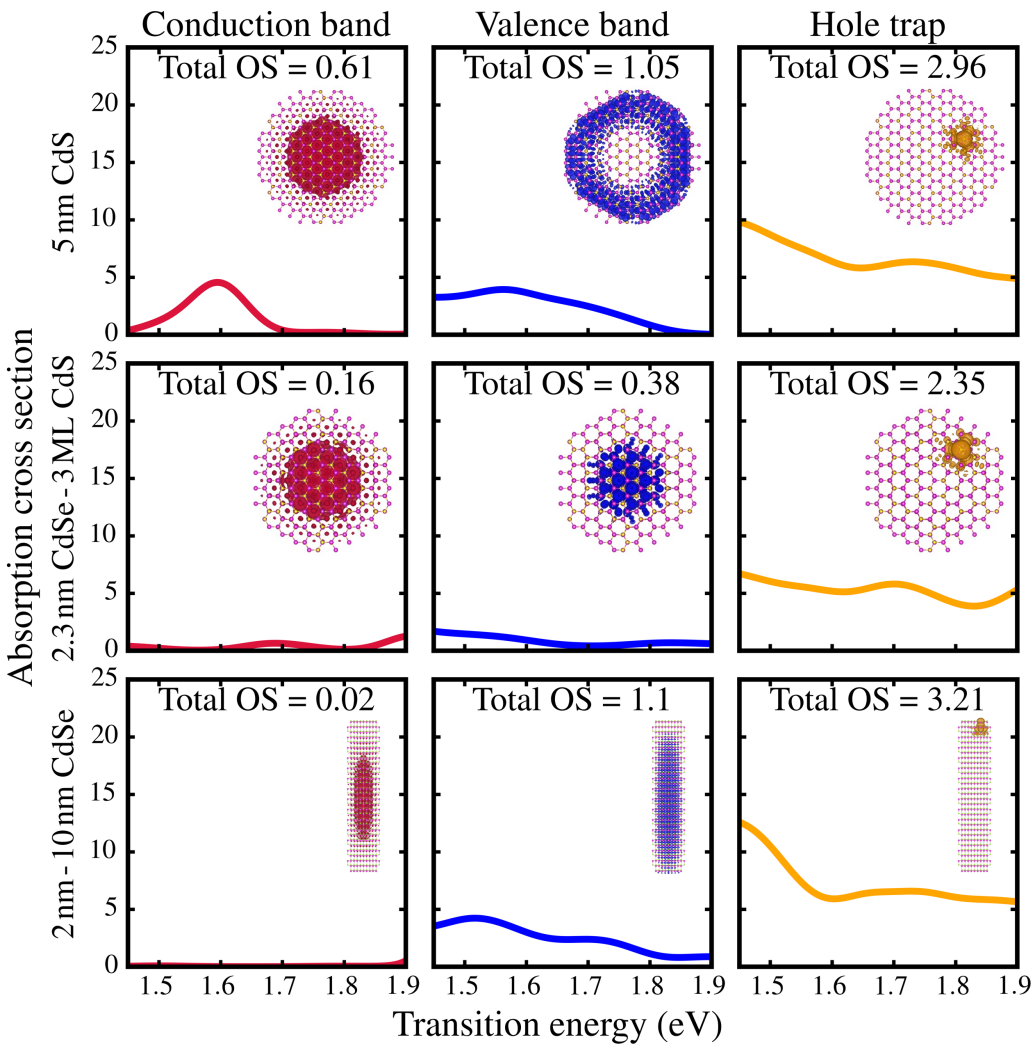

Figure 6.5: Absorption cross section in arbitrary units in the energy region of interest for a 5 nm CdS core (top), 2.3 nm CdSe / 3 monolayer CdS core/shell (center), and 2.1–10 nm CdSe nanorod (bottom). The insets illustrate the charge carrier densities. In these systems, the amplitude of the absorption cross section for the trapped hole state is more than 5 times larger than that for the valence band edge.

hole state [290], leading to a larger absorption cross section for large (greater than 1.45 eV) transition energies.

These conclusions will not depend significantly on the absolute energy of the hole trap state, and they should be consistent for shallow traps that have energies closer to the valence band maximum. The PA amplitude for shallow traps will be slightly decreased, due to the

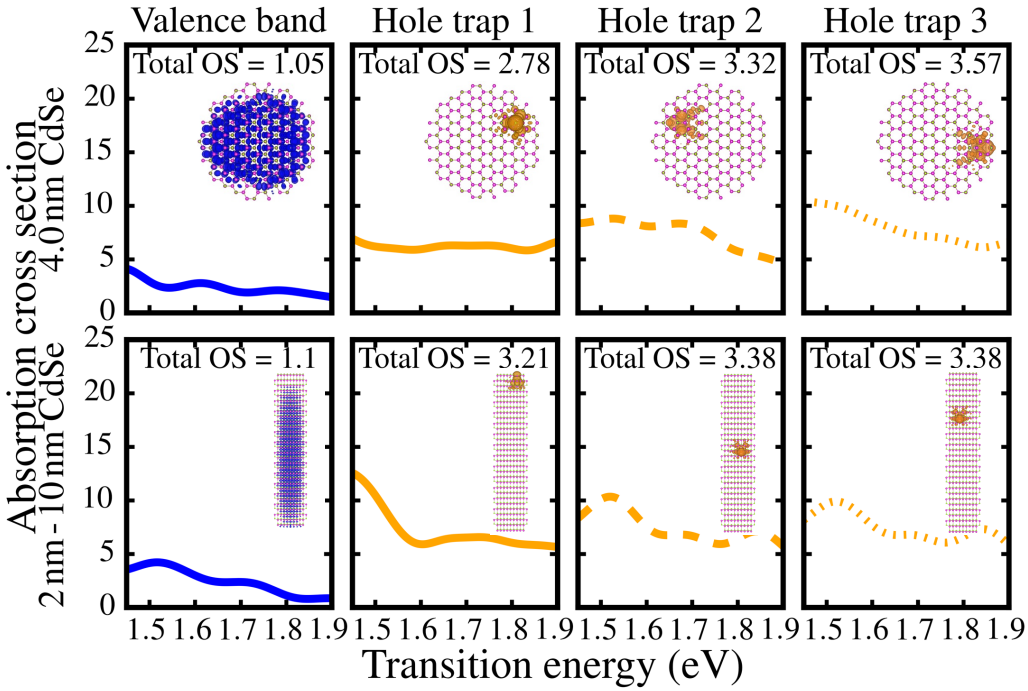

Figure 6.6: The absorption cross sections in arbitrary units in the energy region of interest for a 4 nm CdSe core (top) and 2.1 nm-10 nm CdSe nanorod (bottom) for valence band holes and surface-trapped holes at different locations. The amplitude and shape of the absorption cross section for the trapped hole state is consistent across different trap locations.

dependence of the oscillator strength on the energy between initial and final states, but the contribution of the trapped hole to the overall PA signal will remain significant.

Our findings are consistent with absorption sum rules, which state that the OS between a state and all other states must sum to 1 [306]. Because the OSs for low-energy transitions near the band edge are so strong for electrons and holes, the OSs for transitions to higher-energy states are weaker. On the other hand, surface trap states have very low OSs for these low-energy transitions, so they are relatively larger for transitions greater than 1.45 eV.

6.4 Using photoinduced absorption signals to monitor hole trapping and transfer

Through theoretical investigation of PA features due to band edge electrons and holes and surface-trapped holes, we see that the use of the broad PA feature greater than 1.45 eV (less than 850 nm) to measure the populations of trapped holes is justified. Additionally, unlike

the conduction band bleach feature, which saturates quickly under multiexcitonic conditions due to filling of the $1S_e$ state, the total PA signal is purely additive in the trapped hole region, assuming that the surface traps are spatially separated. This work facilitates the understanding of hole dynamics at high fluences, as the mapping remains linear between the PA amplitude and the number of trapped holes.

This feature is particularly important in studying in NCs because they, unlike molecular light absorbers, have the capacity to concentrate many excited charge carriers within a small volume following multiple photon absorption or charge multiplication processes, due to their large absorptivity and high density of available electronic states [280, 307]. The multiexcitonic state of a NC can enable photophysical processes that are inaccessible by single-excitonic states, such as the transfer of multiple charges on ultrafast time scales [298, 308] and the tunneling transport of electrons across high energy barriers [309]. The efficient extraction of charge carriers from multiexcitonic NCs would also be particularly useful for reactions related to photocatalytic solar fuel generation, as these chemical transformations universally involve multielectron catalysis.

The multiexcitonic state of a NC can undergo multiexcitonic dissociation to transfer charges to acceptors, thereby creating a charge-separated state, which generally has a long lifetime. However, as the excitons are confined in the small volume of a NC, the Coulomb interaction between multiple excitons unavoidably leads to Auger recombination (AR), which nonradiatively annihilates an exciton and creates a hot electron-hole pair. The AR rate increases nonlinearly with the number of excitons in a NC [307]. On fast time scales ranging from several to hundreds of picoseconds (ps), AR can swiftly annihilate charge carriers until the NC is brought to the single-excitonic state [307]. Hole transfer rates are typically much slower, and yet ideally NCs could be designed such that, when multiply excited, hole transfer could still compete efficiently against AR.

In metal chalcogenide NCs, hole trap states are prevalent on the surface due to underpassivated chalcogenide atoms [29, 304]. The multitude of these relatively localized hole traps play an important role in mediating hole transfer from delocalized valence band (VB) states to surface bound acceptors [294, 305, 310]. Hole-trapping states also affect the AR lifetimes by altering the electron-hole interactions and, therefore, significantly impacting the kinetic competition between hole transfer and AR dynamics [290, 311, 312]. As described earlier in this chapter, ultrafast transient absorption (TA) spectroscopy provides the time resolution required to directly track the population of holes in different states as they migrate from NCs to acceptors.

Thus, we utilized TA spectroscopy to investigate the hole transfer dynamics from three different cadmium chalcogenide NCs to a synthesized phenothiazine derivative, which binds to the NC surface via a carboxylate group. The NCs were excited by a pump pulse of 415 nm wavelength and the average initial number of excitons per NC was experimentally calibrated to range from $\sim$1 to 19. The hole acceptor, 4-(3-bromo-7-(dihexylamino)-10H-phenothiazin-10-yl)benzoic acid (NPTZ), was designed to carry functional groups on the phenothiazine ring to shift the PA signal of its oxidized form to the longer wavelength region >600 nm. The shifted PA feature enables us to track the hole transfer in CdSe and CdSe/CdS NCs by

avoiding interference with the exciton bleaching signal.

In the NC-NPTZ systems, the time-dependent populations of the trapped holes and the oxidized ligands were separately tracked and analyzed so that we could systematically investigate the interplay between charge trapping, hole transfer, and AR dynamics. To describe the observed kinetics, we test two types of kinetic models, informed by atomistic calculations of AR rates, where the hole trapping states are kinetically coupled to or decoupled from the VB populations. For NCs passivated with oleate ligands (referred to as native NCs), our results indicate that the hole trapping states exist in a fast trapping/detrapping equilibrium with the VB, and the trapped holes can be rapidly consumed by AR events. In contrast, NCs capped with bulky NPTZ ligands introduce hole-trapping states that are kinetically decoupled from VB states and have prolonged lifetimes, as they are unable to participate in AR. This result is supported by fluence dependent hole transfer kinetics that were observed at intermediate times of ∼10-100 ps, after AR would be expected to relax the NCs to single-excitonic states. These decoupled trapping states resemble the long-lived charge-separated states proposed to account for the "dark states" in NC single particle blinking experiments [313, 314].

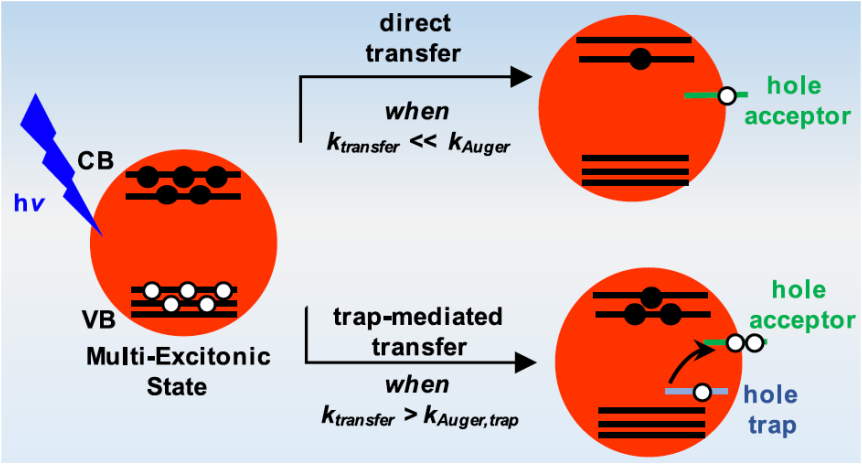

Figure 6.7: There are two primary mechanisms for hole transfer in multiexcitonic NCs. When the rate of hole transfer is faster than that of AR, direct transfer of the hole from the VB to the molecular acceptor occurs within 10 ps. When the rate of hole transfer is slower than that of AR, holes are trapped and undergo a trap-mediated transfer process that occurs on timecales of 10-100 ps.

As illustrated schematically in Fig. 6.7, direct transfer of holes from the NC to the acceptor occurs within 10 ps when the hole transfer rate is faster than the AR rate. When AR is faster than hole transfer, the long-lived, trapped holes can serve as a reservoir to temporarily store charges and then slowly transfer to NPTZ over the course of ∼10-100 ps.

In the most efficient system, up to three holes were transferred to NPTZ per CdS NC.

6.5 Slow Auger recombination of trapped holes enables hole transfer on longer timescales

To identify AR channels in the presence of hole-trapping states, AR lifetimes were computed and compared for two types of initial biexcitonic states: *i*) two electrons in the conduction band (CB) and two holes in the VB, and *ii*) two electrons in the CB, one hole in the VB, and one hole in a surface trapping state. CdSe NCs are chosen as a model system, and calculations were performed on CdSe NCs of different sizes.

6.5.1 Atomistic calculations of Auger recombination rates

NC configurations were obtained using the process described in Ch. 2.2. Details of the four structures modeled and studied here are collected in Table 6.2.

Table 6.2: CdSe NC configurations used for calculation of AR rates.

Configuration	Diameter (nm)
$Cd_{93}Se_{93}$	2.2
$Cd_{222}Se_{222}$	3.0
$Cd_{435}Se_{435}$	3.9
$Cd_{753}Se_{753}$	4.7

All calculations of single-particle electron and hole states, as well as excitonic states were performed within the semiempirical pseudopotential method, as described in Ch. 2.2. The biexcitonic AR lifetime, $\tau_{\mathrm{AR},2}$, was computed using Fermi's golden rule [81], where we average over thermally distributed initial biexcitonic states, $|B\rangle$, with energy E_B, and sum over all final decay channels into single excitonic states, $|S\rangle$, with energy E_S, which are coupled by the Coulomb scattering potential, V:

$$\tau_{\mathrm{AR},2}^{-1} = \sum_B \frac{e^{-\beta E_B}}{Z_B} \left[\frac{2\pi}{\hbar} \sum_S \left| \langle B|V|S\rangle \right|^2 \delta(E_B - E_S) \right]. \tag{6.4}$$

Here, $Z_B = \sum_B e^{-\beta E_B}$ is the partition function for initial biexcitonic states, and $\beta = 1/k_{\mathrm{B}}T$ at room temperature (298 K). The delta function enforces energy conservation between initial and final states and, here, was approximated using:

$$\delta(x) = \begin{cases} 1/2dE & -dE < x < dE \\ 0 & \text{otherwise} \end{cases}, \tag{6.5}$$

where dE is a parameter. We report AR lifetimes for $dE = 10\,\text{meV}$, but the conclusions remain consistent for dE values ranging from 10-100 meV.

The initial biexcitonic and final single excitonic states are given, respectively, by:

$$|B\rangle = \sum_{b,j} \sum_{c,k} c^B_{b,j} c^B_{c,k} \phi_b(\boldsymbol{r}_e) \phi_c(\boldsymbol{r}'_e) \phi_j(\boldsymbol{r}_h) \phi_k(\boldsymbol{r}'_h) \tag{6.6}$$

$$|S\rangle = \phi_a(\boldsymbol{r}_e) \phi_i(\boldsymbol{r}_h)\,, \tag{6.7}$$

where $\phi(\boldsymbol{r}_e)$ and $\phi(\boldsymbol{r}_h)$ are single-particle electron and hole states, respectively, and $c_{a,i}$ are the coefficients obtained from solving the Bethe-Salpeter equation (BSE) (cf., Eq. (2.4)). The indices a, b, c refer to electron (unoccupied) states, and the indices i, j, k refer to hole (occupied) states with corresponding energies ε_a and ε_i. The initial biexcitonic states are formed using interacting electron-hole pair states while the final excitonic states are non-interacting electron-hole pair states, obtained using filter diagonalization calculations with target energies resonant with the initial biexcitonic state. The initial biexcitonic state includes correlations within electron-hole pairs but ignores them between the two excitons [81]. The correlations in the final electron-hole pair are also ignored.

Therefore, the AR lifetime was computed as

$$\begin{aligned}\tau^{-1}_{\text{AR},2} =& \frac{2\pi}{\hbar Z_B} \sum_B e^{-\beta E_B} \sum_{a,i} \Big| \sum_{b,c,k} c^B_{b,i} c^B_{c,k} V_{abck} \Big|^2 \delta(E_B - \varepsilon_a + \varepsilon_i) \\ &+ \frac{2\pi}{\hbar Z_B} \sum_B e^{-\beta E_B} \sum_{a,i} \Big| \sum_{j,c,k} c^B_{a,j} c^B_{c,k} V_{ijck} \Big|^2 \delta(E_B - \varepsilon_a + \varepsilon_i)\,. \end{aligned} \tag{6.8}$$

The first term represents the electron channel of recombination, in which the final electron-hole pair involves a hot electron, and the second term represents the hole channel of recombination, in which the final electron-hole pair involves a hot hole. The Coulomb coupling V_{rsut} is given by

$$V_{rsut} = \int\int d^3\boldsymbol{r} d^3\boldsymbol{r}' \frac{\phi_r(\boldsymbol{r}) \phi_s(\boldsymbol{r}) \phi_u(\boldsymbol{r}') \phi_t(\boldsymbol{r}')}{|\boldsymbol{r} - \boldsymbol{r}'|}\,. \tag{6.9}$$

The initial biexcitonic states including a trapped hole are composed of one exciton with a trap coefficient, c_{tr}, of approximately 1 and another exciton with a trap coefficient of approximately 0. Here, we have defined

$$c_{\text{tr}} \equiv \sum_a |c_{a,\text{tr}}|^2\,, \tag{6.10}$$

where $c_{a,\text{tr}}$ refers to the coefficient of a noninteracting electron-hole pair with the hole in the single-particle trap state. The calculated AR rates were Boltzmann-averaged over five different trap locations that were evenly distributed across the surface of the NC.

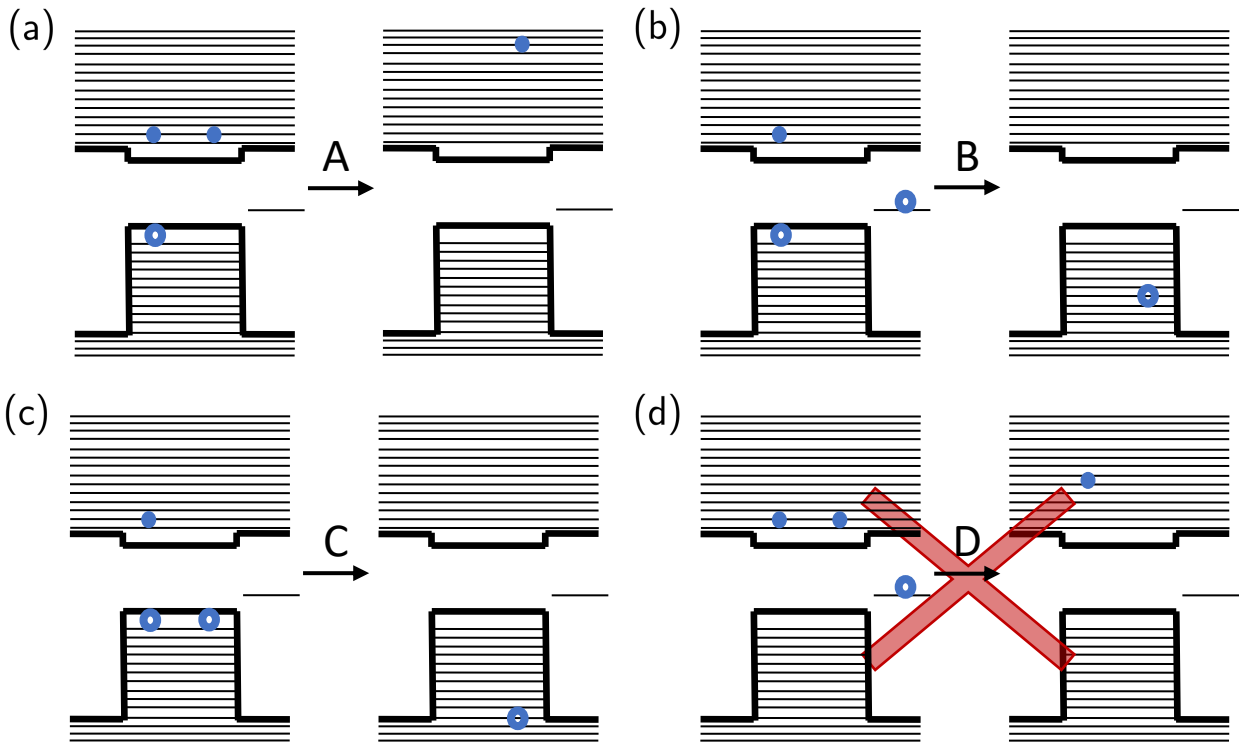

Figure 6.8: AR channels, identifiable by their initial and final states. Channels A and C pertain to an initial biexcitonic state with both holes in the VB while channel B pertains to an intial biexcitonic state with one hole in the VB and the other in a trap state. The fourth "spectator ion" of the initial state is not illustrated, as its energy is unaffected by AR. Channels A-C have comparable rates, while channel D has a rate greater than $10\,\mathrm{ns}^{-1}$.

6.5.2 Identification and characterization of Auger recombination channels

As discussed above and depicted in Fig. 6.8, AR can occur through different negative trion pathways (electron channels) and positive trion pathways (hole channels), leading to different final single electron-hole pair configurations. While Fig. 6.8 shows trion decay channels, the calculations performed here use biexcitonic initial states, so the initial and final state configurations also include a spectator ion that does not participate in AR and has thus been omitted in this illustration for clarity. For channels A and D, the final state is a hot electron and a spectator hole in a VB state or trap state. For channels B and C, the final state is a hot hole and a spectator electron. The rate of each of these channels was determined by examining the partial sum over final states corresponding to that channel. For example, the rate of channel A is given by the sum over final states that correspond to the configuration

shown in Fig. 6.8 (with the appropriate spectator ion):

$$(\tau_{\mathrm{AR},2}^{-1})_{\mathrm{A}} = \sum_{B} \frac{e^{-\beta E_B}}{Z_B} \left[\frac{2\pi}{\hbar} \sum_{S \in \mathrm{A}} \left| \langle B|V|S \rangle \right|^2 \delta(E_B - E_S) \right] . \tag{6.11}$$

The total rate for a given biexcitonic state is a sum of the rates of all the channels. For the biexcitonic state with two electrons in the CB and two holes in the VB, the channels only involve holes in the VB, and the summation for the overall rate is as follows:

$$\tau_{\mathrm{AR,VB}}^{-1} = (\tau_{\mathrm{AR},2}^{-1})_{\mathrm{A}} + (\tau_{\mathrm{AR},2}^{-1})_{\mathrm{C}} . \tag{6.12}$$

For the bi-excitonic state including a trapped hole (two electrons in the CB, one hole in the VB, and one hole in the trap), the channels involve both the VB hole and the trapped hole, and the summation for the overall rate is:

$$\tau_{\mathrm{AR,tr}}^{-1} = (\tau_{\mathrm{AR},2}^{-1})_{\mathrm{A}} + (\tau_{\mathrm{AR},2}^{-1})_{\mathrm{B}} + (\tau_{\mathrm{AR},2}^{-1})_{\mathrm{D}} . \tag{6.13}$$

We found that the rates for channels A, B, and C are comparable while the rate for channel D is 3-4 orders of magnitude smaller than the others. Therefore, we conclude that recombination of an electron and trapped hole is slow, and AR through channel D (or AR of a biexciton with two trapped holes) is negligible. The summed biexcitonic AR lifetimes with or without the trapped hole are very similar, as seen in Table 6.3 below, illustrating that the surface-trapped holes do participate in AR on similar timescales as VB holes so long as there are still holes present at the VB edge.

Table 6.3: Calculated AR lifetimes for an initial biexcitonic state with both holes at the VB edge, $\tau_{\mathrm{AR,VB}}$, compared to those for an initial biexcitonic state with one hole at the VB edge and one hole at a localized surface trap state, $\tau_{\mathrm{AR,tr}}$.

CdSe diameter (nm)	$\tau_{\mathrm{AR,VB}}$ (ps)	$\tau_{\mathrm{AR,tr}}$ (ps)
2.2	7.9	7.6
3.0	16.4	14.9
3.9	47.5	51.7
4.7	144.7	142.7

For channel B, the Coulomb coupling that drives AR requires some overlap between the two holes in the initial biexciton, overlap between one hole and the conduction band-edge electron in the initial biexciton, and overlap between the other hole and the hot hole in the final single exciton. Even though trapped holes are localized to the surface, there is still some wavefunction overlap with the holes at the VB edge, and there is favorable wavefunction overlap with hot hole states in the VB that have more oscillatory wavefunctions delocalized

throughout the NC. Therefore, the rate of channel B can be comparable to that of A and C. The trion with two holes trapped at different sites, however, will not undergo AR as there is little to no overlap between those states. These findings are consistent with the calculations presented at the beginning of this chapter for the photoinduced absorption signals of surface-trapped holes.

These calculations demonstrate that holes must be present near the VB edge for AR to occur. We expect these results to be consistent for both native trap states formed due to an unpassivated chalcogen atom and traps introduced by bulky NPTZ ligands. Kinetic modeling and experimental observation indicates that hole-trapping to native trap states is reversible while hole-trapping to kinetically-decoupled NPTZ-induced trap states is irreversible. This irreversible trapping prevents AR and allows for trap-mediated hole transfer at intermediate timescales beyond AR lifetimes.

6.6 Conclusions

In summary, we have applied ultrafast TA spectroscopy to examine the hole transfer dynamics from cadmium chalcogenide NCs to NPTZ hole-accepting ligands under multiexcitonic conditions. The analysis of TA data was enabled by atomistic electronic structure calculations of photoinduced absorption signals, which confirmed the assignment of broad, positive features to the sub-bandgap photoinduced absorption of trapped holes.

The experimental results indicate that the transfer of multiple holes from NCs to molecular acceptors at short times is possible when the hole transfer rate and AR rate are comparable. Furthermore, the trap-mediated hole transfer occurs on timescales of 10-100 ps, much longer than the AR lifetimes of the NCs studied here. Atomistic calculations of AR lifetimes and modeling of the kinetics data suggest a two-stage transfer mechanism. First, holes can directly transfer to NPTZ ligands under the short-lived multiexcitonic state. Next, multiple irreversibly-trapped holes in decoupled, NPTZ-induced trap states, which have very long AR lifetimes, can gradually transfer charge to acceptors. The results here suggest that careful engineering of hole trap states both in number and kind is required in order to achieve effective hole transfer over nonradiative recombination events when NCs are operating in the multiexcitonic regime.

Bibliography

(1) Alivisatos, A. P. Semiconductor clusters, nanocrystals, and quantum dots. *Science* **1996**, *271*, 933–937.

(2) Scholes, G. D.; Rumbles, G. Excitons in nanoscale systems. *Nat. Mater.* **2006**, *5*, 683–696.

(3) Klimov, V. I. Multicarrier interactions in semiconductor nanocrystals in relation to the phenomena of Auger recombination and carrier multiplication. *Annu. Rev. Condens. Matter Phys.* **2014**, *5*, 285–316.

(4) Efros, A. L.; Brus, L. E. Nanocrystal quantum dots: From discovery to modern development. *ACS Nano* **2021**, *15*, 6192–6210.

(5) Melnychuk, C.; Guyot-Sionnest, P. Multicarrier dynamics in quantum dots. *Chem. Rev.* **2021**, *121*, 2325–2372.

(6) Kagan, C. R.; Bassett, L. C.; Murray, C. B.; Thompson, S. M. Colloidal quantum dots as platforms for quantum information science. *Chem. Rev.* **2021**, *121*, 3186–3233.

(7) Jasrasaria, D.; Weinberg, D.; Philbin, J. P.; Rabani, E. Simulations of nonradiative processes in semiconductor nanocrystals. *J. Chem. Phys.* **2022**, *157*, 020901.

(8) Efros, A.; Efros, A. Interband light absorption in semiconductor spheres. *Sov. Phys. Semicond.* **1982**, *16*, 772–775.

(9) Murray, C. B.; Norris, D. J.; Bawendi, M. G. Synthesis and characterization of nearly monodisperse CdE (E = S, Se, Te) semiconductor nanocrystallites. *J. Am. Chem. Soc.* **1993**, *115*, 8706–8715.

(10) Wang, L. W.; Zunger, A. Electronic structure pseudopotential calculations of large (∼1000 atoms) Si quantum dots. *J. Phys. Chem.* **1994**, *98*, 2158–2165.

(11) Dabbousi, B. O.; Rodriguez-Viejo, J.; Mikulec, F. V.; Heine, J. R.; Mattoussi, H.; Ober, R.; Jensen, K. F.; Bawendi, M. G. (CdSe)ZnS core-shell quantum dots: Synthesis and characterization of a size series of highly luminescent nanocrystallites. *J. Phys. Chem. B* **1997**, *101*, 9463–9475.

(12) Efros, A. L.; Rosen, M. The electronic structure of semiconductor nanocrystals. *Annu. Rev. Mater. Sci.* **2000**, *30*, 475–521.

(13) Rabani, E.; Baer, R. Theory of multiexciton generation in semiconductor nanocrystals. *Chem. Phys. Lett.* **2010**, *496*, 227–235.

(14) Boles, M. A.; Engel, M.; Talapin, D. V. Self-assembly of colloidal nanocrystals: From intricate structures to functional materials. *Chem. Rev.* **2016**, *116*, 11220–11289.

(15) Weiss, E. A. Influence of shape anisotropy on the emission of low-dimensional semiconductors. *ACS Nano* **2021**, *15*, 3568–3577.

(16) Rossetti, R.; Nakahara, S.; Brus, L. E. Quantum size effects in the redox potentials, resonance Raman spectra, and electronic spectra of CdS crystallites in aqueous solution. *J. Chem. Phys.* **1983**, *79*, 1086–1088.

(17) Ekimov, A. I.; Hache, F.; Schanne-Klein, M. C.; Ricard, D.; Flytzanis, C.; Kudryavtsev, I. A.; Yazeva, T. V.; Rodina, A. V.; Efros, A. L. Absorption and intensity-independent photoluminescence measurements on CdSe quantum dots: Assignment of the first electronic transitions. *J. Opt. Soc. Am. B* **1993**, *10*, 100–107.

(18) Norris, D. J.; Sacra, A.; Murray, C. B.; Bawendi, M. G. Measurement of the size dependent hole spectrum in CdSe quantum dots. *Phys. Rev. Lett.* **1994**, *72*, 2612–2615.

(19) Norris, D. J.; Bawendi, M. G. Measurement and assignment of the size-dependent optical spectrum in CdSe quantum dots. *Phys. Rev. B* **1996**, *53*, 16338–16346.

(20) Nirmal, M.; Murray, C. B.; Bawendi, M. G. Fluorescence-line narrowing in CdSe quantum dots: Surface localization of the photogenerated exciton. *Phys. Rev. B* **1994**, *50*, 2293–2300.

(21) Nirmal, M.; Norris, D. J.; Kuno, M.; Bawendi, M. G.; Efros, A. L.; Rosen, M. Observation of the "dark exciton" in CdSe quantum dots. *Phys. Rev. Lett.* **1995**, *75*, 3728–3731.

(22) Norris, D. J.; Efros, A. L.; Rosen, M.; Bawendi, M. G. Size dependence of exciton fine structure in CdSe quantum dots. *Phys. Rev. B* **1996**, *53*, 16347–16354.

(23) Efros, A. L.; Rosen, M.; Kuno, M.; Nirmal, M.; Norris, D. J.; Bawendi, M. Band-edge exciton in quantum dots of semiconductors with a degenerate valence band: Dark and bright exciton states. *Phys. Rev. B* **1996**, *54*, 4843–4856.

(24) Cohen, M. L.; Bergstresser, T. K. Band structures and pseudopotential form factors for fourteen semiconductors of the diamond and zinc-blende structures. *Phys. Rev.* **1966**, *141*, 789–796.

(25) Rama Krishna, M. V.; Friesner, R. A. Exciton spectra of semiconductor clusters. *Phys. Rev. Lett.* **1991**, *67*, 629–632.

(26) Wang, L.-W.; Zunger, A. Pseudopotential calculations of nanoscale CdSe quantum dots. *Phys. Rev. B* **1996**, *53*, 9579–9582.

(27) Rabani, E.; Hetenyi, B.; Berne, B. J.; Brus, L. E. Electronic properties of CdSe nanocrystals in the absence and presence of a dielectric medium. *J. Chem. Phys.* **1999**, *110*, 5355–5369.

(28) Sewall, S. L.; Cooney, R. R.; Kambhampati, P. Experimental tests of effective mass and atomistic approaches to quantum dot electronic structure: Ordering of electronic states. *Appl. Phys. Lett.* **2009**, *94*, 243116.

(29) Califano, M.; Franceschetti, A.; Zunger, A. Temperature dependence of excitonic radiative decay in CdSe quantum dots: The role of surface hole traps. *Nano Lett.* **2005**, *5*, 2360–2364.

(30) Jasrasaria, D.; Philbin, J. P.; Yan, C.; Weinberg, D.; Alivisatos, A. P.; Rabani, E. Sub-bandgap photoinduced transient absorption features in CdSe nanostructures: The role of trapped holes. *J. Phys. Chem. C* **2020**, *124*, 17372–17378.

(31) Wang, L.-W.; Kim, J.; Zunger, A. Electronic structures of [110]-faceted self-assembled pyramidal InAs/GaAs quantum dots. *Phys. Rev. B* **1999**, *59*, 5678–5687.

(32) Mattila, T.; Wang, L.-W.; Zunger, A. Electronic consequences of lateral composition modulation in semiconductor alloys. *Phys. Rev. B* **1999**, *59*, 15270–15284.

(33) Guyot-Sionnest, P.; Shim, M.; Matranga, C.; Hines, M. Intraband relaxation in CdSe quantum dots. *Phys. Rev. B* **1999**, *60*, R2181–R2184.

(34) Klimov, V. I.; Mikhailovsky, A. A.; McBranch, D. W.; Leatherdale, C. A.; Bawendi, M. G. Quantization of multiparticle Auger rates in semiconductor quantum dots. *Science* **2000**, *287*, 1011–1013.

(35) Guyot-Sionnest, P.; Wehrenberg, B.; Yu, D. Intraband relaxation in CdSe nanocrystals and the strong influence of the surface ligands. *J. Chem. Phys.* **2005**, *123*, 074709.

(36) Oron, D.; Kazes, M.; Banin, U. Multiexcitons in type-II colloidal semiconductor quantum dots. *Phys. Rev. B* **2007**, *75*, 1–7.

(37) Pandey, A.; Guyot-Sionnest, P. Slow electron cooling in colloidal quantum dots. *Science* **2008**, *322*, 929–932.

(38) Jones, M.; Lo, S. S.; Scholes, G. D. Quantitative modeling of the role of surface traps in CdSe/CdS/ZnS nanocrystal photoluminescence decay dynamics. *Proc. Natl. Acad. Sci. U.S.A.* **2009**, *106*, 3011–3016.

(39) Sukhovatkin, V.; Hinds, S.; Brzozowski, L.; Sargent, E. H. Colloidal quantum-dot photodetectors exploiting multiexciton generation. *Science* **2009**, *324*, 1542–1544.

(40) McArthur, E. A.; Morris-Cohen, A. J.; Knowles, K. E.; Weiss, E. A. Charge carrier resolved relaxation of the first excitonic state in CdSe quantum dots probed with near-infrared transient absorption spectroscopy. *J. Phys. Chem. B* **2010**, *114*, 14514–14520.

(41) Ulbricht, R.; Hendry, E.; Shan, J.; Heinz, T. F.; Bonn, M. Carrier dynamics in semiconductors studied with time-resolved terahertz spectroscopy. *Rev. Mod. Phys.* **2011**, *83*, 543–586.

(42) Knowles, K. E.; McArthur, E. A.; Weiss, E. A. A multi-timescale map of radiative and nonradiative decay pathways for excitons in CdSe quantum dots. *ACS Nano* **2011**, *5*, 2026–2035.

(43) Bae, W. K.; Padilha, L. A.; Park, Y. S.; McDaniel, H.; Robel, I.; Pietryga, J. M.; Klimov, V. I. Controlled alloying of the core-shell interface in CdSe/CdS quantum dots for suppression of auger recombination. *ACS Nano* **2013**, *7*, 3411–3419.

(44) Qin, W.; Liu, H.; Guyot-Sionnest, P. Small bright charged colloidal quantum dots. *ACS Nano* **2014**, *8*, 283–291.

(45) Kambhampati, P. On the kinetics and thermodynamics of excitons at the surface of semiconductor nanocrystals: Are there surface excitons? *Chem. Phys.* **2015**, *446*, 92–107.

(46) Wu, M.; Congreve, D. N.; Wilson, M. W. B.; Jean, J.; Geva, N.; Welborn, M.; Van Voorhis, T.; Bulovic, V.; Bawendi, M. G.; Baldo, M. A. Solid-state infrared-to-visible upconversion sensitized by colloidal nanocrystals. *Nat. Photonics* **2016**, *10*, 31–34.

(47) Li, Q.; Zhou, B.; McBride, J. R.; Lian, T. Efficient diffusive transport of hot and cold excitons in colloidal type II CdSe/CdTe core/crown nanoplatelet heterostructures. *ACS Energy Lett.* **2017**, *2*, 174–181.

(48) Kaledin, A. L.; Kong, D.; Wu, K.; Lian, T.; Musaev, D. G. Quantum confinement theory of Auger-assisted biexciton recombination dynamics in type-I and quasi type-II quantum dots. *J. Phys. Chem. C* **2018**, *122*, 18742–18750.

(49) Li, Q.; Yang, Y.; Que, W.; Lian, T. Size and morphology dependent Auger recombination in CsPbBr3 perovskite two-dimensional nanoplatelets and one-dimensional nanorods. *Nano Lett.* **2019**, *19*, 5620–5627.

(50) Prezhdo, O. V. Photoinduced dynamics in semiconductor quantum dots: Insights from time-domain ab initio studies. *Acc. Chem. Res.* **2009**, *42*, 2005–2016.

(51) Gfroerer, T. H.; Sturge, M. D.; Kash, K.; Yater, J. A.; Plaut, A. S.; Lin, P. S. D.; Florez, L. T.; Harbison, J. P.; Das, S. R.; Lebrun, L. Slow relaxation of excited states in strain-induced quantum dots. *Phys. Rev. B* **1996**, *53*, 16474–16480.

(52) Yu, H.; Lycett, S.; Roberts, C.; Murray, R. Time resolved study of self-assembled InAs quantum dots. *Appl. Phys. Lett.* **1996**, *69*, 4087–4089.

(53) Heitz, R.; Veit, M.; Ledentsov, N. N.; Hoffmann, A.; Bimberg, D.; Ustinov, V. M.; Kop'ev, P. S.; Alferov, Z. I. Energy relaxation by multiphonon processes in InAs/GaAs quantum dots. *Phys. Rev. B* **1997**, *56*, 10435–10445.

(54) Sosnowski, T. S.; Norris, T. B.; Jiang, H.; Singh, J.; Kamath, K.; Bhattacharya, P. Rapid carrier relaxation in $In_{0.4}Ga_{0.6}As$/GaAs quantum dots characterized by differential transmission spectroscopy. *Phys. Rev. B* **1998**, *57*, R9423–R9426.

(55) Mukai, K.; Sugawara, M. Slow carrier relaxation among sublevels in annealed self-formed InGaAs/GaAs quantum dots. *Jpn J. Appl. Phys.* **1998**, *37*, 5451–5456.

(56) Klimov, V. I.; McBranch, D. W.; Leatherdale, C. A.; Bawendi, M. G. Electron and hole relaxation pathways in semiconductor quantum dots. *Phys. Rev. B* **1999**, *60*, 13740–13749.

(57) Klimov, V. I.; Mikhailovsky, A. A.; McBranch, D. W.; Leatherdale, C. A.; Bawendi, M. G. Mechanisms for intraband energy relaxation in semiconductor quantum dots: The role of electron-hole interactions. *Phys. Rev. B* **2000**, *61*, R13349–R13352.

(58) Harbold, J. M.; Du, H.; Krauss, T. D.; Cho, K.-S.; Murray, C. B.; Wise, F. W. Time-resolved intraband relaxation of strongly confined electrons and holes in colloidal PbSe nanocrystals. *Phys. Rev. B* **2005**, *72*, 195312.

(59) Nozik, A. J. Spectroscopy and hot electron relaxation dynamics in semiconductor quantum wells and quantum dots. *Annu. Rev. Phys. Chem.* **2001**, 193–231.

(60) Efros, A. In *Semiconductor Nanocrystals: From Basic Principles to Applications*, Efros, A. L., Lockwood, D. J., Tsybeskov, L., Eds.; Springer US: Boston, MA, 2003, pp 52–72.

(61) Wang, L.-W.; Califano, M.; Zunger, A.; Franceschetti, A. Pseudopotential theory of Auger processes in CdSe quantum dots. *Phys. Rev. Lett.* **2003**, *91*, 056404.

(62) Hendry, E.; Koeberg, M.; Wang, F.; Zhang, H.; de Mello Donegá, C.; Vanmaekelbergh, D.; Bonn, M. Direct observation of electron-to-hole energy transfer in CdSe quantum dots. *Phys. Rev. Lett.* **2006**, *96*, 057408.

(63) Cooney, R. R.; Sewall, S. L.; Anderson, K. E. H.; Dias, E. A.; Kambhampati, P. Breaking the phonon bottleneck for holes in semiconductor quantum dots. *Phys. Rev. Lett.* **2007**, *98*, 177403.

(64) Cooney, R. R.; Sewall, S. L.; Dias, E. A.; Sagar, D. M.; Anderson, K. E. H.; Kambhampati, P. Unified picture of electron and hole relaxation pathways in semiconductor quantum dots. *Phys. Rev. B* **2007**, *75*, 245311.

(65) Kilina, S. V.; Kilin, D. S.; Prezhdo, O. V. Breaking the phonon bottleneck in PbSe and CdSe quantum dots: Time-domain density functional theory of charge carrier relaxation. *ACS Nano* **2009**, *3*, 93–99.

(66) Robel, I.; Gresback, R.; Kortshagen, U.; Schaller, R. D.; Klimov, V. I. Universal size-dependent trend in Auger recombination in direct-gap and indirect-gap semiconductor nanocrystals. *Phys. Rev. Lett.* **2009**, *102*, 177404.

(67) Hill, N. A.; Whaley, K. B. A theoretical study of the influence of the surface on the electronic structure of CdSe nanoclusters. *J. Chem. Phys.* **1994**, *100*, 2831.

(68) Hanifi, D. A.; Bronstein, N. D.; Koscher, B. A.; Nett, Z.; Swabeck, J. K.; Takano, K.; Schwartzberg, A. M.; Maserati, L.; Vandewal, K.; van de Burgt, Y.; Salleo, A.; Alivisatos, A. P. Redefining near-unity luminescence in quantum dots with photothermal threshold quantum yield. *Science* **2019**, *363*, 1199–1202.

(69) Enright, M. J.; Jasrasaria, D.; Hanchard, M. M.; Needell, D. R.; Phelan, M. E.; Weinberg, D.; McDowell, B. E.; Hsiao, H.-W.; Akbari, H.; Kottwitz, M.; Potter, M. M.; Wong, J.; Zuo, J.-M.; Atwater, H. A.; Rabani, E.; Nuzzo, R. G. Role of the atomic structure on exciton dynamics and photoluminescence in NIR emissive InAs/InP/ZnSe quantum dots. *J. Phys. Chem. C* **2022**, *126*, 7576–7587.

(70) Guzelturk, B.; Cotts, B. L.; Jasrasaria, D.; Philbin, J. P.; Hanifi, D. A.; Koscher, B. A.; Balan, A. D.; Curling, E.; Zajac, M.; Park, S.; Yazdani, N.; Nyby, C.; Kamysbayev, V.; Fischer, S.; Nett, Z.; Shen, X.; Kozina, M. E.; Lin, M. F.; Reid, A. H.; Weathersby, S. P.; Schaller, R. D.; Wood, V.; Wang, X.; Dionne, J. A.; Talapin, D. V.; Alivisatos, A. P.; Salleo, A.; Rabani, E.; Lindenberg, A. M. Dynamic lattice distortions driven by surface trapping in semiconductor nanocrystals. *Nat. Commun.* **2021**, *12*, 1–9.

(71) Chelikowsky, J. R.; Kronik, L.; Vasiliev, I. Time-dependent density-functional calculations for the optical spectra of molecules, clusters, and nanocrystals. *J. Phys. Condens. Matter* **2003**, *15*, R1517–R1547.

(72) Shulenberger, K. E.; Coppieters 't Wallant, S. C.; Klein, M. D.; McIsaac, A. R.; Goldzak, T.; Berkinsky, D. B.; Utzat, H.; Barotov, U.; Van Voorhis, T.; Bawendi, M. G. Resolving the triexciton recombination pathway in CdSe/CdS nanocrystals through state-specific correlation measurements. *Nano Lett.* **2021**, *21*, 7457–7464.

(73) Song, Y.; Liu, R.; Wang, Z.; Xu, H.; Ma, Y.; Fan, F.; Voznyy, O.; Du, J. Enhanced emission directivity from asymmetrically strained colloidal quantum dots. *Sci. Adv.* **2022**, *8*, eabl8219.

(74) Degoli, E.; Guerra, R.; Iori, F.; Magri, R.; Marri, I.; Pulci, O.; Bisi, O.; Ossicini, S. Ab initio calculations of luminescence and optical gain properties in silicon nanostructures. *C. R. Phys.* **2009**, *10*, 575–586.

(75) Friesner, R. A. Ab initio quantum chemistry: Methodology and applications. *Proc. Natl. Acad. Sci. U.S.A.* **2005**, *102*, 6648–6653.

(76) Voznyy, O.; Mokkath, J. H.; Jain, A.; Sargent, E. H.; Schwingenschlögl, U. Computational study of magic-size CdSe clusters with complementary passivation by carboxylic and amine ligands. *J. Phys. Chem. C* **2016**, *120*, 10015–10019.

(77) Williamson, A.; Zunger, A. Pseudopotential study of electron-hole excitations in colloidal free-standing InAs quantum dots. *Phys. Rev. B* **2000**, *61*, 1978–1991.

(78) Wall, M. R.; Neuhauser, D. Extraction, through filter-diagonalization, of general quantum eigenvalues or classical normal mode frequencies from a small number of residues or a short-time segment of a signal. I. Theory and application to a quantum-dynamics model. *J. Chem. Phys.* **1995**, *102*, 8011–8022.

(79) Toledo, S.; Rabani, E. Verly large electronic structure calculations using an out-of-core filter-diagonalization method. *J. Comput. Phys.* **2002**, *180*, 256–269.

(80) Rohlfing, M.; Louie, S. G. Electron-hole excitations and optical spectra from first principles. *Phys. Rev. B* **2000**, *62*, 4927–4944.

(81) Philbin, J. P.; Rabani, E. Electron-hole correlations govern Auger recombination in nanostructures. *Nano Lett.* **2018**, *18*, 7889–7895.

(82) Jasrasaria, D.; Rabani, E. Interplay of surface and interior modes in exciton-phonon coupling at the nanoscale. *Nano Lett.* **2021**, *21*, 8741–8748.

(83) Xu, D.; Cao, J. Non-canonical distribution and non-equilibrium transport beyond weak system-bath coupling regime: A polaron transformation approach. *Front. Phys.* **2016**, *11*, 110308.

(84) Franchini, C.; Reticcioli, M.; Setvin, M.; Diebold, U. Polarons in materials. *Nat. Rev. Mater.* **2021**, *6*, 560–586.

(85) Griffin, G. B.; Ithurria, S.; Dolzhnikov, D. S.; Linkin, A.; Talapin, D. V.; Engel, G. S. Two-dimensional electronic spectroscopy of CdSe nanoparticles at very low pulse power. *J. Chem. Phys.* **2013**, *138*, 014705.

(86) Yan, C.; Weinberg, D.; Jasrasaria, D.; Kolaczkowski, M. A.; Liu, Z.-j.; Philbin, J. P.; Balan, A. D.; Liu, Y.; Schwartzberg, A. M.; Rabani, E.; Alivisatos, A. P. Uncovering the role of hole traps in promoting hole transfer from multiexcitonic quantum dots to molecular acceptors. *ACS Nano* **2021**, *15*, 2281–2291.

(87) Giustino, F. Electron-phonon interactions from first principles. *Rev. Mod. Phys.* **2017**, *89*, 1–63.

(88) Chen, H.-Y.; Sangalli, D.; Bernardi, M. Exciton-phonon interaction and relaxation times from first principles. *Phys. Rev. Lett.* **2020**, *125*, 107401.

(89) Cao, Y. W.; Banin, U. Growth and properties of semiconductor core/shell nanocrystals with InAs cores. *J. Am. Chem. Sci.* **2000**, *122*, 9692–9702.

(90) Reiss, P.; Protière, M.; Li, L. Core/shell semiconductor nanocrystals. *Small* **2009**, *5*, 154–168.

(91) Wuister, S. F.; de Mello Donegá, C.; Meijerink, A. Influence of thiol capping on the exciton luminescence and decay kinetics of CdTe and CdSe quantum dots. *J. Phys. Chem. B* **2004**, *108*, 17393–17397.

(92) Ekimov, A. I.; Efros, A. L.; Onushchenko, A. A. Quantum size effect in semiconductor microcrystals. *Solid State Commun.* **1985**, *56*, 921–924.

(93) Philbin, J. P.; Rabani, E. Auger recombination lifetime scaling for type-I and quasi-type-II core/shell quantum dots. *J. Phys. Chem. Lett.* **2020**, *11*, 5132–5138.

(94) Ondry, J. C.; Philbin, J. P.; Lostica, M.; Rabani, E.; Alivisatos, A. P. Resilient pathways to atomic attachment of quantum dot dimers and artificial solids from faceted CdSe quantum dot building blocks. *ACS Nano* **2019**, *13*, 12322–12344.

(95) Cui, J.; Panfil, Y. E.; Koley, S.; Shamalia, D.; Waiskopf, N.; Remennik, S.; Popov, I.; Oded, M.; Banin, U. Colloidal quantum dot molecules manifesting quantum coupling at room temperature. *Nat. Commun.* **2019**, *10*, 5401.

(96) Zunger, A. Nonlocal pseudopotential calculations of the electronic properties of relaxed GaAs(110) surface. *Phys. Rev. B* **1980**, *22*, 959–969.

(97) Hybertsen, M. S.; Louie, S. G. Spin-orbit splitting in semiconductors and insulators from the ab initio pseudopotential. *Phys. Rev. B* **1986**, *34*, 2920–2922.

(98) Li, Y.-H.; Gong, X. G.; Wei, S.-H. Ab initio all-electron calculation of absolute volume deformation potentials of IV-IV, III-V, and II-VI semiconductors: The chemical trends. *Phys. Rev. B* **2006**, *73*, 245206.

(99) Grünwald, M.; Lutker, K.; Alivisatos, A. P.; Rabani, E.; Geissler, P. L. Metastability in pressure-induced structural transformations of CdSe/ZnS core/shell nanocrystals. *Nano Lett.* **2013**, *13*, 1367–1372.

(100) Hazarika, A.; Fedin, I.; Hong, L.; Guo, J.; Srivastava, V.; Cho, W.; Coropceanu, I.; Portner, J.; Diroll, B. T.; Philbin, J. P.; Rabani, E.; Klie, R.; Talapin, D. V. Colloidal atomic layer deposition with stationary reactant phases enables precise synthesis of "digital" II-VI nano-heterostructures with exquisite control of confinement and strain. *J. Am. Chem. Soc.* **2019**, *141*, 13487–13496.

(101) Bergstresser, T. K.; Cohen, M. L. Electronic structure and optical properties of hexagonal CdSe, CdS, and ZnS. *Phys. Rev.* **1967**, *164*, 1069–1080.

(102) Öğüt, S.; Chelikowsky, J. R.; Louie, S. G. Quantum confinement and optical gaps in Si nanocrystals. *Phys. Rev. Lett.* **1997**, *79*, 1770–1773.

(103) Zhou, X. W.; Ward, D. K.; Martin, J. E.; Van Swol, F. B.; Cruz-Campa, J. L.; Zubia, D. Stillinger-Weber potential for the II-VI elements Zn-Cd-Hg-S-Se-Te. *Phys. Rev. B* **2013**, *88*, 085309.

(104) Han, P.; Bester, G. Interatomic potentials for the vibrational properties of III-V semiconductor nanostructures. *Phys. Rev. B* **2011**, *83*, 174304.

(105) Kelley, A. M. Comparison of three empirical force fields for phonon calculations in CdSe quantum dots. *J. Chem. Phys.* **2016**, *144*, 214702.

(106) Wang, L.-W.; Zunger, A. High-energy excitonic transitions in CdSe quantum dots. *J. Phys. Chem. B* **1998**, *102*, 6449–6454.

(107) Fan, K.; Liao, C.; Xu, R.; Zhang, H.; Cui, Y.; Zhang, J. Effect of shell thickness on electrochemical property of wurtzite CdSe/CdS core/shell nanocrystals. *Chem. Phys. Lett.* **2015**, *633*, 1–5.

(108) Yu, W. W.; Qu, L.; Guo, W.; Peng, X. Experimental determination of the extinction coefficient of CdTe, CdSe, and CdS nanocrystals. *Chem. Mater.* **2003**, *15*, 2854–2860.

(109) Franceschetti, A.; Zunger, A. Direct pseudopotential calculation of exciton Coulomb and exchange energies in semiconductor quantum dots. *Phys. Rev. Lett.* **1997**, *78*, 915–918.

(110) Banin, U.; Cao, Y.; Katz, D.; Millo, O. Identification of atomic-like electronic states in indium arsenide nanocrystal quantum dots. *Nature* **1999**, *400*, 542–544.

(111) Guzelian, A. A.; Banin, U.; Kadavanich, A. V.; Peng, X.; Alivisatos, A. P. Colloidal chemical synthesis and characterization of InAs nanocrystal quantum dots. *Appl. Phys. Lett.* **1996**, *69*, 1432–1434.

(112) Franceschetti, A.; Zunger, A. Pseudopotential calculations of electron and hole addition spectra of InAs, InP, and Si quantum dots. *Phys. Rev. B* **2000**, *62*, 2614–2623.

(113) Eshet, H.; Grünwald, M.; Rabani, E. The electronic structure of CdSe/CdS Core/shell seeded nanorods: Type-I or quasi-type-II? *Nano Lett.* **2013**, *13*, 5880–5885.

(114) Brumberg, A.; Harvey, S. M.; Philbin, J. P.; Diroll, B. T.; Crooker, S. A.; Wasielewski, M. R.; Rabani, E.; Schaller, R. D. Determination of the in-plane exciton radius in 2D CdSe nanoplatelets via magneto-optical spectroscopy. *ACS Nano* **2019**, *13*, 8589–8596.

(115) Hadar, I.; Philbin, J. P.; Panfil, Y. E.; Neyshtadt, S.; Lieberman, I.; Eshet, H.; Lazar, S.; Rabani, E.; Banin, U. Semiconductor seeded nanorods with graded composition exhibiting high quantum-yield, high polarization, and minimal blinking. *Nano Lett.* **2017**, *17*, 2524–2531.

(116) Philbin, J. P.; Brumberg, A.; Diroll, B. T.; Cho, W.; Talapin, D. V.; Schaller, R. D.; Rabani, E. Area and thickness dependence of Auger recombination in nanoplatelets. *J. Chem. Phys.* **2020**, *153*, 054104.

(117) Bozyigit, D.; Yazdani, N.; Yarema, M.; Yarema, O.; Lin, W. M. M.; Volk, S.; Vuttivorakulchai, K.; Luisier, M.; Juranyi, F.; Wood, V. Soft surfaces of nanomaterials enable strong phonon interactions. *Nature* **2016**, *531*, 618–622.

(118) Mack, T. G.; Jethi, L.; Andrews, M.; Kambhampati, P. Direct observation of vibronic coupling between excitonic states of CdSe nanocrystals and their passivating ligands. *J. Phys. Chem. C* **2019**, *123*, 5084–5091.

(119) Wei, S.; Chou, M. Y. Ab initio calculation of force constants and full phonon dispersions. *Phys. Rev. Lett.* **1992**, *69*, 2799–2802.

(120) Han, P.; Bester, G. First-principles calculation of the electron-phonon interaction in semiconductor nanoclusters. *Phys. Rev. B* **2012**, *85*, 1–7.

(121) Han, P.; Bester, G. Fundamental difference between measured and calculated exciton-phonon coupling in nanostructures. *Phys. Rev. B* **2019**, *99*, 1–6.

(122) Kong, L. T. Phonon dispersion measured directly from molecular dynamics simulations. *Comput. Phys. Commun.* **2011**, *182*, 2201–2207.

(123) Grünwald, M.; Zayak, A.; Neaton, J. B.; Geissler, P. L.; Rabani, E. Transferable pair potentials for CdS and ZnS crystals. *J. Chem. Phys.* **2012**, *136*, 234111.

(124) Chilla, G.; Kipp, T.; Menke, T.; Heitmann, D.; Nikolic, M.; Frömsdorf, A.; Kornowski, A.; Förster, S.; Weller, H. Direct observation of confined acoustic phonons in the photoluminescence spectra of a single CdSe-CdS-ZnS core-shell-shell nanocrystal. *Phys. Rev. Lett.* **2008**, *100*, 057403.

(125) Mork, A. J.; Lee, E. M. Y.; Tisdale, W. A. Temperature dependence of acoustic vibrations of CdSe and CdSe–CdS core–shell nanocrystals measured by low-frequency Raman spectroscopy. *Phys. Chem. Chem. Phys.* **2016**, *18*, 28797–28801.

(126) Yang, J.; Wen, X.; Xia, H.; Sheng, R.; Ma, Q.; Kim, J.; Tapping, P.; Harada, T.; Kee, T. W.; Huang, F.; Cheng, Y.-B.; Green, M.; Ho-Baillie, A.; Huang, S.; Shrestha, S.; Patterson, R.; Conibeer, G. Acoustic-optical phonon up-conversion and hot-phonon bottleneck in lead-halide perovskites. *Nat. Commun.* **2017**, *8*, 14120.

(127) Jia, X.; Jiang, J.; Zhang, Y.; Qiu, J.; Wang, S.; Chen, Z.; Yuan, N.; Ding, J. Observation of enhanced hot phonon bottleneck effect in 2D perovskites. *Appl. Phys. Lett.* **2018**, *112*, 143903.

(128) Leo, K.; Rühle, W. W.; Ploog, K. Hot-carrier energy-loss rates in $GaAs/Al_xGa_{1-x}As$ quantum wells. *Phys. Rev. B* **1988**, *38*, 1947–1957.

(129) Klimov, V.; Haring Bolivar, P.; Kurz, H. Hot-phonon effects in femtosecond luminescence spectra of electron-hole plasmas in CdS. *Phys. Rev. B* **1995**, *52*, 4728–4731.

(130) Yang, Y.; Ostrowski, D. P.; France, R. M.; Zhu, K.; van de Lagemaat, J.; Luther, J. M.; Beard, M. C. Observation of a hot-phonon bottleneck in lead-iodide perovskites. *Nat. Photonics* **2016**, *10*, 53–59.

(131) Li, Q.; Lian, T. Area- and thickness-dependent biexciton Auger recombination in colloidal CdSe nanoplatelets: Breaking the "universal volume scaling law". *Nano Lett.* **2017**, *17*, 3152–3158.

(132) Rabani, E. An interatomic pair potential for cadmium selenide. *J. Chem. Phys.* **2002**, *116*, 258–262.

(133) Han, P.; Bester, G. Force field potentials for the vibrational properties of II-VI semiconductor nanostructures. *Phys. Rev. B* **2017**, *96*, 195436.

(134) Fernée, M. J.; Sinito, C.; Mulvaney, P.; Tamarat, P.; Lounis, B. The optical phonon spectrum of CdSe colloidal quantum dots. *Phys. Chem. Chem. Phys.* **2014**, *16*, 16957–16961.

(135) Szilagyi, E.; Wittenberg, J. S.; Miller, T. A.; Lutker, K.; Quirin, F.; Lemke, H.; Zhu, D.; Chollet, M.; Robinson, J.; Wen, H.; Sokolowski-Tinten, K.; Lindenberg, A. M. Visualization of nanocrystal breathing modes at extreme strains. *Nat. Commun.* **2015**, *6*, 6577.

(136) Sagar, D. M.; Cooney, R. R.; Sewall, S. L.; Dias, E. A.; Barsan, M. M.; Butler, I. S.; Kambhampati, P. Size dependent, state-resolved studies of exciton-phonon couplings in strongly confined semiconductor quantum dots. *Phys. Rev. B* **2008**, *77*, 1–14.

(137) Mahan, G. D., *Many-Particle Physics*; Springer: Boston, MA, 2000.

(138) Takagahara, T. Electron-phonon interactions in semiconductor nanocrystals. *J. Lumin.* **1996**, *70*, 129–143.

(139) Salvador, M. R.; Graham, M. W.; Scholes, G. D. Exciton-phonon coupling and disorder in the excited states of CdSe colloidal quantum dots. *J. Chem. Phys.* **2006**, *125*, 184709.

(140) Morello, G.; De Giorgi, M.; Kudera, S.; Manna, L.; Cingolani, R.; Anni, M. Temperature and size dependence of nonradiative relaxation and exciton-phonon coupling in colloidal CdTe quantum dots. *J. Phys. Chem. C* **2007**, *111*, 5846–5849.

(141) Sagar, D. M.; Cooney, R. R.; Sewall, S. L.; Kambhampati, P. State-resolved exciton-phonon couplings in CdSe semiconductor quantum dots. *J. Phys. Chem. C* **2008**, *112*, 9124–9127.

(142) Nomura, S.; Kobayashi, T. Exciton–LO-phonon couplings in spherical semiconductor microcrystallites. *Phys. Rev. B* **1992**, *45*, 1305.

(143) Scamarcio, G.; Spagnolo, V.; Ventruti, G.; Lugará, M.; Righini, G. Size dependence of electron–LO-phonon coupling in semiconductor nanocrystals. *Phys. Rev. B* **1996**, *53*, R10489–R10492.

(144) Heitz, R.; Mukhametzhanov, I.; Stier, O.; Madhukar, A.; Bimberg, D. Enhanced polar exciton-LO-phonon interaction in quantum dots. *Phys. Rev. Lett.* **1999**, *83*, 4654–4657.

(145) Lin, C.; Gong, K.; Kelley, D. F.; Kelley, A. M. Electron-phonon coupling in CdSe/CdS core/shell quantum dots. *ACS Nano* **2015**, *9*, 8131–8141.

(146) Lin, C.; Gong, K.; Kelley, D. F.; Kelley, A. M. Size-dependent exciton-phonon coupling in CdSe nanocrystals through resonance Raman excitation profile analysis. *J. Phys. Chem. C* **2015**.

(147) Klein, M. C.; Hache, F.; Ricard, D.; Flytzanis, C. Size dependence of electron-phonon coupling in semiconductor nanospheres: The case of CdSe. *Phys. Rev. B* **1990**, *42*, 11123–11132.

(148) Marini, J. C.; Stebe, B.; Kartheuser, E. Exciton-phonon interaction in CdSe and CuCl polar semiconductor nanospheres. *Phys. Rev. B* **1994**, *50*, 14302–14308.

(149) Hamma, M.; Miranda, R. P.; Vasilevskiy, M. I.; Zorkani, I. Calculation of the Huang-Rhys parameter in spherical quantum dots: The optical deformation potential effect. *J. Phys. Condens. Matter* **2007**, *19*.

(150) Chu, I. H.; Radulaski, M.; Vukmirovic, N.; Cheng, H. P.; Wang, L. W. Charge transport in a quantum dot supercrystal. *J. Phys. Chem. C* **2011**, *115*, 21409–21415.

(151) Kelley, A. M. Electron-phonon coupling in CdSe nanocrystals from an atomistic phonon model. *ACS Nano* **2011**, *5*, 5254–5262.

(152) Yazdani, N.; Bozyigit, D.; Vuttivorakulchai, K.; Luisier, M.; Infante, I.; Wood, V. Tuning electron-phonon interactions in nanocrystals through surface termination. *Nano Lett.* **2018**, *18*, 2233–2242.

(153) Yazdani, N.; Andermatt, S.; Yarema, M.; Farto, V.; Bani-Hashemian, M. H.; Volk, S.; Lin, W. M.; Yarema, O.; Luisier, M.; Wood, V. Charge transport in semiconductors assembled from nanocrystal quantum dots. *Nat. Commun.* **2020**, *11*, 1–9.

(154) Zeng, T.; He, Y. Ab initio modeling of phonon-assisted relaxation of electrons and excitons in semiconductor nanocrystals for multiexciton generation. *Phys. Rev. B* **2021**, *103*, 1–15.

(155) Balan, A. D.; Eshet, H.; Olshansky, J. H.; Lee, Y. V.; Rabani, E.; Alivisatos, A. P. Effect of thermal fluctuations on the radiative rate in core/shell quantum dots. *Nano Lett.* **2017**, *17*, 1629–1636.

(156) Cui, J.; Beyler, A. P.; Coropceanu, I.; Cleary, L.; Avila, T. R.; Chen, Y.; Cordero, J. M.; Heathcote, S. L.; Harris, D. K.; Chen, O.; Cao, J.; Bawendi, M. G. Evolution of the single-nanocrystal photoluminescence linewidth with size and shell: Implications for exciton-phonon coupling and the optimization of spectral linewidths. *Nano Lett.* **2016**, *16*, 289–296.

(157) Mack, T. G.; Jethi, L.; Kambhampati, P. Temperature dependence of emission line widths from semiconductor nanocrystals reveals vibronic contributions to line broadening processes. *J. Phys. Chem. C* **2017**, *121*, 28537–28545.

(158) Peterson, M. D.; Cass, L. C.; Harris, R. D.; Edme, K.; Sung, K.; Weiss, E. A. The role of ligands in determining the exciton relaxation dynamics in semiconductor quantum dots. *Annu. Rev. Phys. Chem.* **2014**, *65*, 317–339.

(159) Tvrdy, K.; Frantsuzov, P. A.; Kamat, P. V. Photoinduced electron transfer from semiconductor quantum dots to metal oxide nanoparticles. *Proc. Natl. Acad. Sci. U. S. A.* **2011**, *108*, 29–34.

(160) Harris, R. D.; Bettis Homan, S.; Kodaimati, M.; He, C.; Nepomnyashchii, A. B.; Swenson, N. K.; Lian, S.; Calzada, R.; Weiss, E. A. Electronic processes within quantum dot-molecule complexes. *Chem. Rev.* **2016**, *116*, 12865–12919.

(161) Craig, C. F.; Duncan, W. R.; Prezhdo, O. V. Trajectory surface hopping in the time-dependent Kohn-Sham approach for electron-nuclear dynamics. *Phys. Rev. Lett.* **2005**, *95*, 163001.

(162) Akimov, A. V.; Prezhdo, O. V. The PYXAID program for non-adiabatic molecular dynamics in condensed matter systems. *J. Chem. Theory Comput.* **2013**, *9*, 4959–4972.

(163) Yazdani, N.; Volk, S.; Yarema, O.; Yarema, M.; Wood, V. Size, ligand, and defect-dependent electron-phonon coupling in chalcogenide and perovskite nanocrystals and its impact on luminescence line widths. *ACS Photonics* **2020**, *7*, 1088–1095.

(164) Liptay, T. J.; Marshall, L. F.; Rao, P. S.; Ram, R. J.; Bawendi, M. G. Anomalous stokes shift in CdSe nanocrystals. *Phys. Rev. B* **2007**, *76*, 1–7.

(165) Palato, S.; Seiler, H.; Nijjar, P.; Prezhdo, O.; Kambhampati, P. Atomic fluctuations in electronic materials revealed by dephasing. *Proc. Natl. Acad. Sci. U. S. A.* **2020**, *117*, 11940–11946.

(166) Mooney, J.; Krause, M. M.; Saari, J. I.; Kambhampati, P. A microscopic picture of surface charge trapping in semiconductor nanocrystals. *J. Chem. Phys.* **2013**, *138*, 204705.

(167) Jethi, L.; Mack, T. G.; Kambhampati, P. Extending semiconductor nanocrystals from the quantum dot regime to the molecular cluster regime. *J. Phys. Chem. C* **2017**, *121*, 26102–26107.

(168) Fischer, G., *Vibronic Coupling: The Interaction Between the Electronic and Nuclear Motions*; Theoretical chemistry; Academic Press: 1984.

(169) Peterson, M. D.; Cass, L. C.; Harris, R. D.; Edme, K.; Sung, K.; Weiss, E. A. The role of ligands in determining the exciton relaxation dynamics in semiconductor quantum dots. *Annu. Rev. Phys. Chem.* **2014**, *65*, 317–339.

(170) Von der Linde, D.; Lambrich, R. Direct measurement of hot-electron relaxation by picosecond spectroscopy. *Phys. Rev. Lett.* **1979**, *42*, 1090–1093.

(171) Pugnet, M.; Collet, J.; Cornet, A. Cooling of hot electron-hole plasmas in the presence of screened electron-phonon interactions. *Solid State Commun.* **1981**, *38*, 531–536.

(172) Prabhu, S. S.; Vengurlekar, A. S.; Roy, S. K.; Shah, J. Nonequilibrium dynamics of hot carriers and hot phonons in CdSe and GaAs. *Phys. Rev. B* **1995**, *51*, 14233–14246.

(173) Inoshita, T.; Sakaki, H. Electron relaxation in a quantum dot: Significance of multiphonon processes. *Phys. Rev. B* **1992**, *46*, 7260–7263.

(174) Asahi, H. Self-organized quantum wires and dots in III–V semiconductors. *Adv. Mater.* **1997**, *9*, 1019–1026.

(175) Klimov, V. I.; McBranch, D. W. Femtosecond 1P-to-1S electron relaxation in strongly confined semiconductor nanocrystals. *Phys. Rev. Lett.* **1998**, *80*, 4028.

(176) Schaller, R. D.; Pietryga, J. M.; Goupalov, S. V.; Petruska, M. A.; Ivanov, S. A.; Klimov, V. I. Breaking the phonon bottleneck in semiconductor nanocrystals via multiphonon emission induced by intrinsic nonadiabatic interactions. *Phys. Rev. Lett.* **2005**, *95*, 196401.

(177) Kharchenko, V.; Rosen, M. Auger relaxation processes in semiconductor nanocrystals and quantum wells. *J. Lumin.* **1996**, *70*, 158–169.

(178) Efros, A. L.; Kharchenko, V.; Rosen, M. Breaking the phonon bottleneck in nanometer quantum dots: Role of Auger-like processes. *Solid State Commun.* **1995**, *93*, 281–284.

(179) Nitzan, A.; Press, O. U., *Chemical Dynamics in Condensed Phases: Relaxation, Transfer and Reactions in Condensed Molecular Systems*; Oxford Graduate Texts; OUP Oxford: 2006.

(180) Zimanyi, E. N.; Silbey, R. J. Theoretical description of quantum effects in multichromophoric aggregates. *Philos. Trans. R. Soc. A* **2012**, *370*, 3620–3637.

(181) Egorov, S.; Skinner, J. Semiclassical approximations to quantum time correlation functions. *Chem. Phys. Lett.* **1998**, *293*, 469–476.

(182) Englman, R.; Jortner, J. The energy gap law for radiationless transitions in large molecules. *Mol. Phys.* **1970**, *18*, 145–164.

(183) Hilborn, R. C. Einstein coefficients, cross sections, f values, dipole moments, and all that. *Am. J. Phys.* **1982**, *50*, 982.

(184) Dasgupta, N. P.; Sun, J.; Liu, C.; Brittman, S.; Andrews, S. C.; Lim, J.; Gao, H.; Yan, R.; Yang, P. 25th anniversary article: Semiconductor nanowires—Synthesis, characterization, and applications. *Adv. Mater.* **2014**, *26*, 2137–2184.

(185) Kovalenko, M. V.; Manna, L.; Cabot, A.; Hens, Z.; Talapin, D. V.; Kagan, C. R.; Klimov, V. I.; Rogach, A. L.; Reiss, P.; Milliron, D. J.; Guyot-Sionnnest, P.; Konstantatos, G.; Parak, W. J.; Hyeon, T.; Korgel, B. A.; Murray, C. B.; Heiss, W. Prospects of nanoscience with nanocrystals. *ACS Nano* **2015**, *9*, 1012–1057.

(186) Kim, J. Y.; Voznyy, O.; Zhitomirsky, D.; Sargent, E. H. 25th anniversary article: Colloidal quantum dot materials and devices— A quarter-century of advances. *Adv. Mater.* **2013**, *25*, 4986–5010.

(187) Kagan, C. R.; Lifshitz, E.; Sargent, E. H.; Talapin, D. V. Building devices from colloidal quantum dots. *Science* **2016**, *353*, aac5523.

(188) Talapin, D. V.; Lee, J. S.; Kovalenko, M. V.; Shevchenko, E. V. Prospects of colloidal nanocrystals for electronic and optoelectronic applications. *Chem. Rev.* **2010**, *110*, 389–458.

(189) Klimov, V. I.; Mikhailovsky, A. A.; Xu, S.; Malko, A.; Hollingsworth, J. A.; Leatherdale, C. A.; Eisler, H.-J.; Bawendi, M. G. Optical gain and stimulated emission in nanocrystal quantum dots. *Science* **2000**, *290*, 314–317.

(190) Livache, C.; Martinez, B.; Goubet, N.; Ramade, J.; Lhuillier, E. Road map for nanocrystal based infrared photodetectors. *Front. Chem* **2018**, *6*, 1–11.

(191) Semonin, O. E.; Luther, J. M.; Choi, S.; Chen, H.-Y.; Gao, J.; Nozik, A. J.; Beard, M. C. Peak external photocurrent quantum efficiency exceeding 100% via MEG in a quantum dot solar cell. *Science* **2011**, *334*, 1530–1533.

(192) Shirasaki, Y.; Supran, G. J.; Bawendi, M. G.; Bulović, V. Emergence of colloidal quantum-dot light-emitting technologies. *Nat. Photon.* **2013**, *7*, 13–23.

(193) Knappenberger, K. L.; Wong, D. B.; Romanyuk, Y. E.; Leone, S. R. Excitation wavelength dependence of fluorescence intermittency in CdSe/ZnS core/shell quantum dots. *Nano Lett.* **2007**, *7*, 3869–3874.

(194) Geißler, D.; Würth, C.; Wolter, C.; Weller, H.; Resch-Genger, U. Excitation wavelength dependence of the photoluminescence quantum yield and decay behavior of CdSe/CdS quantum dot/quantum rods with different aspect ratios. *Phys. Chem. Chem. Phys.* **2017**, *19*, 12509–12516.

(195) Hoy, J.; Morrison, P. J.; Steinberg, L. K.; Buhro, W. E.; Loomis, R. A. Excitation energy dependence of the photoluminescence quantum yields of core and core/shell quantum dots. *J. Phys. Chem. Lett.* **2013**, *4*, 2053–2060.

(196) Li, S.; Steigerwald, M. L.; Brus, L. E. Surface states in the photoionization of high-quality CdSe core/shell nanocrystals. *ACS Nano* **2009**, *3*, 1267–1273.

(197) Klimov, V. I.; Ivanov, S. S. a.; Nanda, J.; Achermann, M.; Bezel, I.; McGuire, J. a. J.; Piryatinski, A. Single-exciton optical gain in semiconductor nanocrystals. *Nature* **2007**, *447*, 441–446.

(198) Bae, W. K.; Park, Y.-S.; Lim, J.; Lee, D.; Padilha, L. a.; McDaniel, H.; Robel, I.; Lee, C.; Pietryga, J. M.; Klimov, V. I. Controlling the influence of Auger recombination on the performance of quantum-dot light-emitting diodes. *Nat. Commun.* **2013**, *4*, 2661.

(199) Kambhampati, P. Hot exciton relaxation dynamics in semiconductor quantum dots: radiationless transitions on the nanoscale. *J. Phys. Chem. C* **2011**, *115*, 22089–22109.

(200) Pietryga, J. M.; Park, Y. S.; Lim, J.; Fidler, A. F.; Bae, W. K.; Brovelli, S.; Klimov, V. I. Spectroscopic and device aspects of nanocrystal quantum dots. *Chem. Rev.* **2016**, *116*, 10513–10622.

(201) Javaux, C.; Mahler, B.; Dubertret, B.; Shabaev, A.; Rodina, A. V.; Efros, A. L.; Yakovlev, D. R.; Liu, F.; Bayer, M.; Camps, G.; Biadala, L.; Buil, S.; Quelin, X.; Hermier, J.-P. Thermal activation of non-radiative Auger recombination in charged colloidal nanocrystals. *Nat. Nanotechnol.* **2013**, *8*, 206–12.

(202) McBride, J. R.; Pennycook, T. J.; Pennycook, S. J.; Rosenthal, S. J. The possibility and implications of dynamic nanoparticle surfaces. *ACS Nano* **2013**, *7*, 8358–8365.

(203) Utterback, J. K.; Grennell, A. N.; Wilker, M. B.; Pearce, O. M.; Eaves, J. D.; Dukovic, G. Observation of trapped-hole diffusion on the surfaces of CdS nanorods. *Nat. Chem.* **2016**, *8*, 1061–1066.

(204) Kirschner, M. S.; Hannah, D. C.; Diroll, B. T.; Zhang, X.; Wagner, M. J.; Hayes, D.; Chang, A. Y.; Rowland, C. E.; Lethiec, C. M.; Schatz, G. C.; Chen, L. X.; Schaller, R. D. Transient melting and recrystallization of semiconductor nanocrystals under multiple electron-hole pair excitation. *Nano Lett.* **2017**, *17*, 5315–5320.

(205) Cline, R. P.; Utterback, J. K.; Strong, S. E.; Dukovic, G.; Eaves, J. D. On the nature of trapped-hole states in CdS nanocrystals and the mechanism of their diffusion. *J. Phys. Chem. Lett.* **2018**, *9*, 3532–3537.

(206) Weathersby, S. P. Mega-electron-volt ultrafast electron diffraction at SLAC National Accelerator Laboratory. *Rev. Sci. Instrum.* **2015**, *86*, 073702.

(207) Gao, H. X.; Peng, L.-. M. Parameterization of the temperature dependence of the Debye–Waller factors. *Acta Crystallogr. A* **1999**, *55*, 926–932.

(208) Plimpton, S. Fast parallel algorithms for short-range molecular dynamics. *J. Comput. Phys.* **1995**, *117*, 1–19.

(209) Wu, X.; Tan, L. Z.; Shen, X.; Hu, T.; Miyata, K.; Trinh, M. T.; Li, R.; Coffee, R.; Liu, S.; Egger, D. A.; Makasyuk, I.; Zheng, Q.; Fry, A.; Robinson, J. S.; Smith, M. D.; Guzelturk, B.; Karunadasa, H. I.; Wang, X.; Zhu, X.; Kronik, L.; Rappe, A. M.; Lindenberg, A. M. Light-induced picosecond rotational disordering of the inorganic sublattice in hybrid perovskites. *Sci. Adv.* **2017**, *3*, e1602388.

(210) Guzelturk, B.; Utterback, J. K.; Coropceanu, I.; Kamysbayev, V.; Janke, E. M.; Zajac, M.; Yazdani, N.; Cotts, B. L.; Park, S.; Sood, A.; Lin, M.-F.; Reid, A. H.; Kozina, M. E.; Shen, X.; Weathersby, S. P.; Wood, V.; Salleo, A.; Wang, X.; Talapin, D. V.; Ginsberg, N. S.; Lindenberg, A. M. Nonequilibrium thermodynamics of colloidal gold nanocrystals monitored by ultrafast electron diffraction and optical scattering microscopy. *ACS Nano* **2020**, *14*, 4792–4804.

(211) Yang, X.; Masadeh, A. S.; McBride, J. R.; Božin, E. S.; Rosenthal, S. J.; Billinge, S. J. L. Confirmation of disordered structure of ultrasmall CdSe nanoparticles from X-ray atomic pair distribution function analysis. *Phys. Chem. Chem. Phys.* **2013**, *15*, 8480–8486.

(212) Achermann, M.; Bartko, A. P.; Hollingsworth, J. A.; Klimov, V. I. The effect of Auger heating on intraband carrier relaxation in semiconductor quantum rods. *Nat. Phys.* **2006**, *2*, 557–561.

(213) Hannah, D. C.; Brown, K. E.; Young, R. M.; Wasielewski, M. R.; Schatz, G. C.; Co, D. T.; Schaller, R. D. Direct measurement of lattice dynamics and optical phonon excitation in semiconductor nanocrystals using femtosecond stimulated raman spectroscopy. *Phys. Rev. Lett.* **2013**, *111*, 107401.

(214) Tewary, V. K.; Yang, B. Singular behavior of the Debye-Waller factor of graphene. *Phys. Rev. B* **2009**, *79*, 125416.

(215) Straub, J. E.; Borkovec, M.; Berne, B. J. Calculation of dynamic friction on intramolecular degrees of freedom. *J. Phys. Chem.* **1987**, *91*, 4995–4998.

(216) Egorov, S. A.; Rabani, E.; Berne, B. J. Nonradiative relaxation processes in condensed phases: Quantum versus classical baths. *J. Chem. Phys.* **1999**, *110*, 5238–5248.

(217) Bader, J. S.; Berne, B. J. Quantum and classical relaxation rates from classical simulations. *J. Chem. Phys.* **1994**, *100*, 8359–8366.

(218) Gillespie, D. T. Exact stochastic simulation of coupled chemical reactions. *J. Phys. Chem.* **1977**, *81*, 2340–2361.

(219) Wu, K.; Lim, J.; Klimov, V. I. Superposition principle in Auger recombination of charged and neutral multicarrier states in semiconductor quantum dots. *ACS Nano* **2017**, *11*, 8437–8447.

(220) Wei, H. H.-Y.; Evans, C. M.; Swartz, B. D.; Neukirch, A. J.; Young, J.; Prezhdo, O. V.; Krauss, T. D. Colloidal semiconductor quantum dots with tunable surface composition. *Nano Lett.* **2012**, *12*, 4465–4471.

(221) Chen, J.-. S.; Zang, H.; Li, M.; Cotlet, M. Hot excitons are responsible for increasing photoluminescence blinking activity in single lead sulfide/cadmium sulfide nanocrystals. *Chem. Commun.* **2018**, *54*, 495–498.

(222) Houtepen, A. J.; Hens, Z.; Owen, J. S.; Infante, I. On the origin of surface traps in colloidal II–VI semiconductor nanocrystals. *Chem. Mater.* **2017**, *29*, 752–761.

(223) Galland, C.; Ghosh, Y.; Steinbrück, A.; Sykora, M.; Hollingsworth, J. A.; Klimov, V. I.; Htoon, H. Two types of luminescence blinking revealed by spectroelectrochemistry of single quantum dots. *Nature* **2011**, *479*, 203–207.

(224) Puzder, A.; Williamson, A. J.; Gygi, F.; Galli, G. Self-healing of CdSe nanocrystals: First-principles calculations. *Phys. Rev. Lett.* **2004**, *92*, 217401.

(225) Kilina, S.; Velizhanin, K. A.; Ivanov, S.; Prezhdo, O. V.; Tretiak, S. Surface ligands increase photoexcitation relaxation rates in CdSe quantum dots. *ACS Nano* **2012**, *6*, 6515–6524.

(226) Voznyy, O.; Thon, S. M.; Ip, A. H.; Sargent, E. H. Dynamic trap formation and elimination in colloidal quantum dots. *J. Phys. Chem. Lett.* **2013**, *4*, 987–992.

(227) Sippel, P.; Albrecht, W.; Mitoraj, D.; Eichberger, R.; Hannappel, T.; Vanmaekelbergh, D. Two-photon photoemission study of competing auger and surface-mediated relaxation of hot electrons in CdSe quantum dot solids. *Nano Lett.* **2013**, *13*, 1655–1661.

(228) Sargent, E. H. Solution-processed infrared optoelectronics: Photovoltaics, sensors, and sources. *IEEE J. Sel. Top. Quantum Electron.* **2008**, *14*, 1223.

(229) Fu, H.; Zunger, A. InP quantum dots: Electronic structure, surface effects, and the redshifted emission. *Phys. Rev. B* **1997**, *56*, 1496.

(230) Steckel, J. S.; Coe-Sullivan, S.; Bulović, V.; Bawendi, M. G. 1.3μm to 1.55μm tunable electroluminescence from PbSe quantum dots embedded within an organic device. *Adv. Mater.* **2003**, *15*, 1862.

(231) Konstantatos, G.; Howard, I.; Fischer, A.; Hoogland, S.; Clifford, J.; Klem, E.; Levina, L.; Sargent, E. H. Ultrasensitive solution-cast quantum dot photodetectors. *Nature* **2006**, *442*, 180.

(232) Sun, Q.; Wang, Y. A.; Li, L. S.; Wang, D.; Zhu, T.; Xu, J.; Yang, C.; Li, Y. Bright, multicoloured light-emitting diodes based on quantum dots. *Nat. Photonics* **2007**, *1*, 717.

(233) Nozik, A. J.; Beard, M. C.; Luther, J. M.; Law, M.; Ellingson, R. J.; Johnson, J. C. Semiconductor quantum dots and quantum dot arrays and applications of multiple exciton generation to third-generation photovoltaic solar cells. *Chem. Rev.* **2010**, *110*, 6873.

(234) Keuleyan, S.; Lhuillier, E.; Brajuskovic, V.; Guyot-Sionnest, P. Mid-infrared HgTe colloidal quantum dot photodetectors. *Nat. Photonics* **2011**, *5*, 489.

(235) Dai, X.; Zhang, Z.; Jin, Y.; Niu, Y.; Cao, H.; Liang, X.; Chen, L.; Wang, J.; Peng, X. Solution-processed, high-performance light-emitting diodes based on quantum dots. *Nature* **2014**, *515*, 96.

(236) Carey, G. H.; Abdelhady, A. L.; Ning, Z.; Thon, S. M.; Bakr, O. M.; Sargent, E. H. Colloidal quantum dot solar cells. *Chem. Rev.* **2015**, *115*, 12732.

(237) Lu, H.; Carroll, G. M.; Neale, N. R.; Beard, M. C. Infrared quantum dots: Progress, challenges, and opportunities. *ACS Nano* **2019**, *13*, 939.

(238) Klem, E. J. D.; Levina, L.; Sargent, E. H. PbS quantum dot electroabsorption modulation across the extended communications band 1200–1700 nm. *Appl. Phys. Lett.* **2005**, *87*, 053101.

(239) Bruns, O. T.; Bischof, T. S.; Harris, D. K.; Franke, D.; Shi, Y.; Riedemann, L.; Bartelt, A.; Jaworski, F. B.; Carr, J. A.; Rowlands, C. J. Next-generation in vivo optical imaging with short-wave infrared quantum dots. *Nat. Biomed. Eng.* **2017**, *1*, 0056.

(240) Meinardi, F.; McDaniel, H.; Carulli, F.; Colombo, A.; Velizhanin, K. A.; Makarov, N. S.; Simonutti, R.; Klimov, V. I.; Brovelli, S. Highly efficient large-area colourless luminescent solar concentrators using heavy-metal-free colloidal quantum dots. *Nat. Nanotechnol.* **2015**, *10*, 878.

(241) Sargent, E. H. Infrared quantum dots. *Adv. Mater.* **2005**, *17*, 515.

(242) Ma, Q.; Su, X. Near-infrared quantum dots: Synthesis, functionalization and analytical applications. *Analyst* **2010**, *135*, 1867.

(243) Kershaw, S. V.; Susha, A. S.; Rogach, A. L. Narrow bandgap colloidal metal chalcogenide quantum dots: Synthetic methods, heterostructures, assemblies, electronic and infrared optical properties. *Chem. Soc. Rev.* **2013**, *42*, 3033.

(244) Colvin, V. L.; Schlamp, M. C.; Alivisatos, A. P. Light-emitting diodes made from cadmium selenide nanocrystals and a semiconducting polymer. *Nature* **1994**, *370*, 354–357.

(245) Dabbousi, B. O.; Bawendi, M. G.; Onitsuka, O.; Rubner, M. F. Electroluminescence from CdSe quantum-dot/polymer composites. *Appl. Phys. Lett.* **1995**, *66*, 1316.

(246) Mattoussi, H.; Radzilowski, L. H.; Dabbousi, B. O.; Thomas, E. L.; Bawendi, M. G.; Rubner, M. F. Electroluminescence from heterostructures of poly(phenylene vinylene) and inorganic CdSe nanocrystals. *J. Appl. Phys.* **1998**, *83*, 7965.

(247) Schlamp, M. C.; Peng, X.; Alivisatos, A. P. Improved efficiencies in light emitting diodes made with CdSe(CdS) core/shell type nanocrystals and a semiconducting polymer. *J. Appl. Phys.* **1997**, *82*, 5837.

(248) Bruchez, M.; Moronne, M.; Gin, P.; Weiss, S.; Alivisatos, A. P. Semiconductor nanocrystals as fluorescent biological labels. *Science* **1998**, *281*, 2013.

(249) Mitchell, G. P.; Mirkin, C. A.; Letsinger, R. L. Programmed assembly of DNA functionalized quantum dots. *J. Am. Chem. Soc.* **1999**, *121*, 8122.

(250) Chan, W. C. W.; Nie, S. Quantum dot bioconjugates for ultrasensitive nonisotopic detection. *Science* **1998**, *281*, 2016.

(251) Naczynski, D. J.; Tan, M. C.; Zevon, M.; Wall, B.; Kohl, J.; Kulesa, A.; Chen, S.; Roth, C. M.; Riman, R. E.; Moghe, P. V. Rare-earth-doped biological composites as in vivo shortwave infrared reporters. *Nat. Commun.* **2013**, *4*, 2199.

(252) Wang, R.; Li, X.; Zhou, L.; Zhang, F. Epitaxial seeded growth of rare-earth nanocrystals with efficient 800 nm near-infrared to 1525 nm short-wavelength infrared downconversion photoluminescence for in vivo bioimaging. *Angew. Chem., Int. Ed.* **2014**, *53*, 12086.

(253) Zhang, Y.; Hong, G.; Zhang, Y.; Chen, G.; Li, F.; Dai, H.; Wang, Q. Ag 2S quantum dot: A bright and biocompatible fluorescent nanoprobe in the second near-infrared window. *ACS Nano* **2012**, *6*, 3695.

(254) Hatami, S.; Würth, C.; Kaiser, M.; Leubner, S.; Gabriel, S.; Bahrig, L.; Lesnyak, V.; Pauli, J.; Gaponik, N.; Eychmüller, A. Absolute photoluminescence quantum yields of IR26 and IR-emissive $Cd_{1-x}Hg_xTe$ and PbS quantum dots-method- and material-inherent challenges. *Nanoscale* **2015**, *7*, 133.

(255) Semonin, O. E.; Johnson, J. C.; Luther, J. M.; Midgett, A. G.; Nozik, A. J.; Beard, M. C. Absolute photoluminescence quantum yields of IR-26 dye, PbS, and PbSe quantum dots. *J. Phys. Chem. Lett.* **2010**, *1*, 2445.

(256) Rurack, K.; Spieles, M. Fluorescence quantum yields of a series of red and near-infrared dyes emitting at 600-1000 nm. *Anal. Chem.* **2011**, *83*, 1232.

(257) Srivastava, V.; Kamysbayev, V.; Hong, L.; Dunietz, E.; Klie, R. F.; Talapin, D. V. Colloidal chemistry in molten salts: Synthesis of luminescent $In_{1-x}Ga_xP$ and $In_{1-x}Ga_xAs$ quantum dots. *J. Am. Chem. Soc.* **2018**, *140*, 12144.

(258) Sagar, L. K.; Bappi, G.; Johnston, A.; Chen, B.; Todorović, P.; Levina, L.; Saidaminov, M. I.; García de Arquer, F. P.; Hoogland, S.; Sargent, E. H. Single-precursor intermediate shelling enables bright, narrow line width InAs/InZnP-based QD emitters. *Chem. Mater.* **2020**, *32*, 2919.

(259) Franke, D.; Harris, D. K.; Chen, O.; Bruns, O. T.; Carr, J. A.; Wilson, M. W. B.; Bawendi, M. G. Continuous injection synthesis of indium arsenide quantum dots emissive in the short-wavelength infrared. *Nat. Commun.* **2016**, *7*, 12749.

(260) Aharoni, A.; Mokari, T.; Popov, I.; Banin, U. Synthesis of InAs/ CdSe/ ZnSe core/ shell/ shell structures with bright and stable near-infrared fluorescence. *J. Am. Chem. Soc.* **2006**, *128*, 257.

(261) Li, Y.; Hou, X.; Dai, X.; Yao, Z.; Lv, L.; Jin, Y.; Peng, X. Stoichiometry-controlled InP-based quantum dots: Synthesis, photoluminescence, and electroluminescence. *J. Am. Chem. Soc.* **2019**, *141*, 6448.

(262) Pietra, F.; Kirkwood, N.; De Trizio, L.; Hoekstra, A. W.; Kleibergen, L.; Renaud, N.; Koole, R.; Baesjou, P.; Manna, L.; Houtepen, A. J. Ga for Zn cation exchange allows for highly luminescent and photostable InZnP-based quantum dots. *Chem. Mater.* **2017**, *29*, 5192.

(263) Kim, S.; Kim, T.; Kang, M.; Kwak, S. K.; Yoo, T. W.; Park, L. S.; Yang, I.; Hwang, S.; Lee, J. E.; Kim, S. K. Highly luminescent InP/GaP/ZnS nanocrystals and their application to white light-emitting diodes. *J. Am. Chem. Soc.* **2012**, *134*, 3804.

(264) Sagar, L. K.; Bappi, G.; Johnston, A.; Chen, B.; Todorović, P.; Levina, L.; Saidaminov, M. I.; García de Arquer, F. P.; Nam, D.-H.; Choi, M.-J.; Hoogland, S.; Voznyy, O.; Sargent, E. H. Suppression of Auger recombination by gradient alloying in InAs/CdSe/CdS QDs. *Chem. Mater.* **2020**, *32*, 7703–7709.

(265) Wijaya, H.; Darwan, D.; Zhao, X.; Woan Yuann Ong, E.; Rui Garrick Lim, K.; Wang, T.; Jun Lim, L.; Hong Khoo, K.; Tan, Z.-K.; Wijaya, H. Efficient near-infrared light-emitting diodes based on In(Zn)As–In(Zn)P–GaP–ZnS quantum dots. *Adv. Funct. Mater.* **2020**, *30*, 1906483.

(266) Xie, R.; Chen, K.; Chen, X.; Peng, X. InAs/InP/ZnSe core/shell/shell quantum dots as near-infrared emitters: Bright, narrow-band, non-cadmium containing, and biocompatible. *Nano Res.* **2008**, *1*, 457.

(267) Enright, M. J.; Dou, F. Y.; Wu, S.; Rabe, E. J.; Monahan, M.; Friedfeld, M. R.; Schlenker, C. W.; Cossairt, B. M. Seeded growth of nanoscale semiconductor tetrapods: Generality and the role of cation exchange. *Chem. Mater.* **2020**, *32*, 4774–4784.

(268) Mundy, M. E.; Eagle, F. W.; Hughes, K. E.; Gamelin, D. R.; Cossairt, B. M. Synthesis and spectroscopy of emissive, surface-modified, copper-doped indium phosphide nanocrystals. *ACS Mater. Lett.* **2020**, *2*, 576.

(269) Wei, S. H.; Zunger, A. Calculated natural band offsets of all II-VI and III-V semiconductors: Chemical trends and the role of cation *d* orbitals. *Appl. Phys. Lett.* **1998**, *72*, 2011.

(270) Gong, M.; Duan, K.; Li, C. F.; Magri, R.; Narvaez, G. A.; He, L. Electronic structure of self-assembled InAs InP quantum dots: Comparison with self-assembled InAs GaAs quantum dots. *Phys. Rev. B* **2008**, *77*, 045326.

(271) Micic, O. I.; Curtis, C. J.; Jones, K. M.; Sprague, J. R.; Nozik, A. J. Synthesis and characterization of InP quantum dots. *J. Phys. Chem.* **1994**, *98*, 4966–4969.

(272) Giessen, H.; Fluegel, B.; Mohs, G.; Peyghambarian, N.; Sprague, J. R.; Micic, O. I.; Nozik, A. J. Observation of the quantum confined ground state in InP quantum dots at 300 K. *Appl. Phys. Lett.* **1996**, *68*, 304–306.

(273) Mushonga, P.; Onani, M. O.; Madiehe, A. M.; Meyer, M. Indium phosphide-based semiconductor nanocrystals and their applications. *J. Nanomater.* **2012**, *2012*, 12.

(274) Won, Y. H.; Cho, O.; Kim, T.; Chung, D. Y.; Kim, T.; Chung, H.; Jang, H.; Lee, J.; Kim, D.; Jang, E. Highly efficient and stable InP/ZnSe/ZnS quantum dot light-emitting diodes. *Nature* **2019**, *575*, 634.

(275) Stein, J. L.; Holden, W. M.; Venkatesh, A.; Mundy, M. E.; Rossini, A. J.; Seidler, G. T.; Cossairt, B. M. Probing surface defects of InP quantum dots using phosphorus Kα and Kβ x-ray emission spectroscopy. *Chem. Mater.* **2018**, *30*, 6377.

(276) Kim, Y.; Chang, J. H.; Choi, H.; Kim, Y. H.; Bae, W. K.; Jeong, S. III-V colloidal nanocrystals: Control of covalent surfaces. *Chem. Sci.* **2020**, *11*, 913.

(277) Leatherdale, C. A.; Woo, W. K.; Mikulec, F. V.; Bawendi, M. G. On the absorption cross section of CdSe nanocrystal quantum dots. *J. Phys. Chem. B* **2002**, *106*, 7619.

(278) Jasieniak, J.; Smith, L.; Van Embden, J.; Mulvaney, P.; Califano, M. Re-examination of the size-dependent absorption properties of CdSe quantum dots. *J. Phys. Chem. C* **2009**, *113*, 19468.

(279) Yu, P.; Beard, M. C.; Ellingson, R. J.; Fernere, S.; Curtis, C.; Drexler, J.; Luiszer, F.; Nozik, A. J. Absorption cross-section and related optical properties of colloidal InAs quantum dots. *J. Phys. Chem. B* **2005**, *109*, 7084.

(280) Klimov, V. I. Spectral and dynamical properties of multiexcitons in semiconductor nanocrystals. *Annu. Rev. Phys. Chem.* **2007**, *58*, 635.

(281) Bronstein, N. D.; Yao, Y.; Xu, L.; O'Brien, E.; Powers, A. S.; Ferry, V. E.; Alivisatos, A. P.; Nuzzo, R. G. Quantum dot luminescent concentrator cavity exhibiting 30-fold concentration. *ACS Photonics* **2015**, *2*, 1576.

(282) Xu, J.; Voznyy, O.; Liu, M.; Kirmani, A. R.; Walters, G.; Munir, R.; Abdelsamie, M.; Proppe, A. H.; Sarkar, A.; García De Arquer, F. P. 2D matrix engineering for homogeneous quantum dot coupling in photovoltaic solids. *Nat. Nanotechnol.* **2018**, *13*, 456.

(283) Waiskopf, N.; Ben-Shahar, Y.; Banin, U. Photocatalytic hybrid semiconductor-metal nanoparticles; From synergistic properties to emerging applications. *Adv. Mater.* **2018**, *30*, 1.

(284) Wolff, C. M.; Frischmann, P. D.; Schulze, M.; Bohn, B. J.; Wein, R.; Livadas, P.; Carlson, M. T.; Jäckel, F.; Feldmann, J.; Würthner, F. All-in-one visible-light-driven water splitting by combining nanoparticulate and molecular co-catalysts on CdS nanorods. *Nat. Energy* **2018**, *3*, 862.

(285) Chen, O.; Zhao, J.; Chauhan, V. P.; Cui, J.; Wong, C.; Harris, D. K.; Wei, H.; Han, H. S.; Fukumura, D.; Jain, R. K.; Bawendi, M. G. Compact high-quality CdSe-CdS core-shell nanocrystals with narrow emission linewidths and suppressed blinking. *Nat. Mater.* **2013**, *12*, 445–451.

(286) Kozlov, O. V.; Park, Y.-S.; Roh, J.; Fedin, I.; Nakotte, T.; Klimov, V. I. Sub-single-exciton lasing using charged quantum dots coupled to a distributed feedback cavity. *Science* **2019**, *675*, 672.

(287) Lannoo, M.; Delerue, C.; Allan, G. Theory of radiative and nonradiative transitions for semiconductor nanocrystals. *J. Lumin.* **1996**, *70*, 170.

(288) Ghosh, T.; Dehnel, J.; Fabian, M.; Lifshitz, E.; Baer, R.; Ruhman, S. Spin Blockades to Relaxation of Hot Multiexcitons in Nanocrystals. *J. Phys. Chem. Lett.* **2019**, *10*, 2341.

(289) Sewall, S. L.; Cooney, R. R.; Anderson, K. E.; Dias, E. A.; Kambhampati, P. State-to-state exciton dynamics in semiconductor quantum dots. *Phys. Rev. B* **2006**, *74*, 235328.

(290) Tyagi, P.; Kambhampati, P. False multiple exciton recombination and multiple exciton generation signals in semiconductor quantum dots arise from surface charge trapping. *J. Chem. Phys.* **2011**, *134*, 094706.

(291) Malko, A. V.; Mikhailovsky, A. A.; Petruska, M. A.; Hollingsworth, J. A.; Klimov, V. I. Interplay between optical gain and photoinduced absorption in CdSe nanocrystals. *J. Phys. Chem. B* **2004**, *108*, 5250.

(292) Burda, C.; Link, S.; Mohamed, M.; El-Sayed, M. The relaxation pathways of CdSe nanoparticles monitored with femtosecond time-resolution from the visible to the IR: Assignment of the transient features by carrier quenching. *J. Phys. Chem. B* **2001**, *105*, 12286.

(293) Burda, C.; Link, S.; Mohamed, M. B.; El-Sayed, M. The pump power dependence of the femtosecond relaxation of CdSe nanoparticles observed in the spectral range from visible to infrared. *J. Chem. Phys.* **2002**, *116*, 3828.

(294) Lian, S.; Weinberg, D. J.; Harris, R. D.; Kodaimati, M. S.; Weiss, E. A. Subpicosecond photoinduced hole transfer from a CdS quantum dot to a molecular acceptor bound through an exciton-delocalizing ligand. *ACS Nano* **2016**, *10*, 6372.

(295) Schnitzenbaumer, K. J.; Labrador, T.; Dukovic, G. Impact of chalcogenide ligands on excited state dynamics in CdSe quantum dots. *J. Phys. Chem. C* **2015**, *119*, 13314.

(296) Morris-Cohen, A. J.; Frederick, M. T.; Cass, L. C.; Weiss, E. A. Simultaneous determination of the adsorption constant and the photoinduced electron transfer rate for a Cds quantum dot-viologen complex. *J. Am. Chem. Soc.* **2011**, *133*, 10146.

(297) Lian, S.; Christensen, J. A.; Kodaimati, M. S.; Rogers, C. R.; Wasielewski, M. R.; Weiss, E. A. Oxidation of a molecule by the biexcitonic state of a CdS quantum dot. *J. Phys. Chem. C* **2019**, *123*, 5923.

(298) Zhu, H.; Song, N.; Rodríguez-Córdoba, W.; Lian, T. Wave function engineering for efficient extraction of up to nineteen electrons from one CdSe/CdS quasi-type II quantum dot. *J. Am. Chem. Soc.* **2012**, *134*, 4250.

(299) Wu, K.; Du, Y.; Tang, H.; Chen, Z.; Lian, T. Efficient extraction of trapped holes from colloidal CdS nanorods. *J. Am. Chem. Soc.* **2015**, *137*, 10224.

(300) Wu, K.; Zhu, H.; Liu, Z.; Rodríguez-Córdoba, W.; Lian, T. Ultrafast charge separation and long-lived charge separated state in photocatalytic CdS-Pt nanorod heterostructures. *J. Am. Chem. Soc.* **2012**, *134*, 10337.

(301) Fischer, S. A.; Isborn, C. M.; Prezhdo, O. V. Excited states and optical absorption of small semiconducting clusters: Dopants, defects and charging. *Chem. Sci.* **2011**, *2*, 400.

(302) Lifshitz, E.; Glozman, A.; Litvin, I. D.; Porteanu, H. Optically detected magnetic resonance studies of the surface/interface properties of II-VI semiconductor quantum dots. *J. Phys. Chem. B* **2000**, *104*, 10449.

(303) Veamatahau, A.; Jiang, B.; Seifert, T.; Makuta, S.; Latham, K.; Kanehara, M.; Teranishi, T.; Tachibana, Y. Origin of surface trap states in CdS quantum dots: Relationship between size dependent photoluminescence and sulfur vacancy trap states. *Phys. Chem. Chem. Phys.* **2015**, *17*, 2850.

(304) Giansante, C.; Infante, I. Surface traps in colloidal quantum dots: A combined experimental and theoretical perspective. *J. Phys. Chem. Lett.* **2017**, *8*, 5209–5215.

(305) Olshansky, J. H.; Balan, A. D.; Ding, T. X.; Fu, X.; Lee, Y. V.; Alivisatos, A. P. Temperature-dependent hole transfer from photoexcited quantum dots to molecular species: Evidence for trap-mediated transfer. *ACS Nano* **2017**, *11*, 8346.

(306) Hens, Z. Can the oscillator strength of the quantum dot bandgap transition exceed unity? *Chem. Phys. Lett.* **2008**, *463*, 391.

(307) Zhu, H.; Yang, Y.; Lian, T. Multiexciton annihilation and dissociation in quantum confined semiconductor nanocrystals. *Acc. Chem. Res.* **2013**, *46*, 1270.

(308) Ben-Shahar, Y.; Philbin, J. P.; Scotognella, F.; Ganzar, L.; Cerullo, G.; Rabani, E.; Banin, U. Charge carrier dynamics in photocatalytic hybrid semiconductor-metal nanorods: crossover from Auger recombination to charge transfer. *Nano Lett.* **2018**, *18*, 5211–5216.

(309) Gao, J.; Kidon, L.; Rabani, E.; Alivisatos, A. P. Ultrahigh hot carrier transient photocurrent in nanocrystal arrays by Auger recombination. *Nano Lett.* **2019**, *19*, 4804.

(310) Tarafder, K.; Surendranath, Y.; Olshansky, J. H.; Alivisatos, A. P.; Wang, L.-W. Hole transfer dynamics from a CdSe/CdS quantum rod to a tethered ferrocene derivative. *J. Am. Chem. Soc.* **2014**, *136*, 5121.

(311) Walsh, B. R.; Saari, J. I.; Krause, M. M.; Nick, R.; Coe-Sullivan, S.; Kambhampati, P. Surface and interface effects on non-radiative exciton recombination and relaxation dynamics in CdSe/Cd,Zn, S nanocrystals. *Chem. Phys.* **2016**, *471*, 11.

(312) He, Y.; Hu, S.; Han, T.; Chen, X.; Yu, Y.; Li, T.; Zhu, W.; Ouyang, G. Suppression of the Auger recombination process in CdSe/CdS core/shell nanocrystals. *ACS Omega* **2019**, *4*, 9198.

(313) Frantsuzov, P.; Kuno, M.; Jankó, B.; Marcus, R. A. Universal emission intermittency in quantum dots, nanorods and nanowires. *Nat. Phys.* **2008**, *4*, 519.

(314) Efros, A. L.; Rosen, M. Random telegraph signal in the photoluminescence intensity of a single quantum dot. *Phys. Rev. Lett.* **1997**, *78*, 1110.